ESPOO 2007 VTT PUBLICATIONS 664

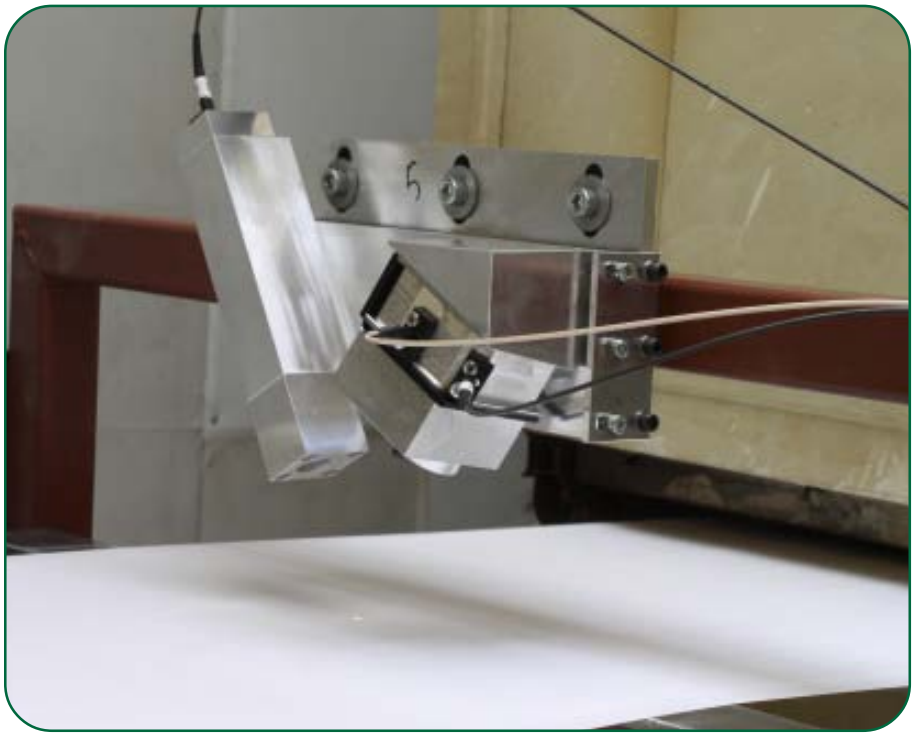

Janne Paaso

Moisture depth profiling in paper using near-infrared spectroscopy

VTT PUBLICATIONS 664

Moisture depth profiling in paper using near-infrared spectroscopy

Janne Paaso

Academic Dissertation to be presented
with the assent of the Faculty of Technology, University of Oulu,
for public discussion in the Auditorium TA105, Linnanmaa,
on December 14th, 2007, at 12 o'clock noon.

ISBN 978-951-38-7063-8 (soft back ed.)
ISSN 1235-0621 (soft back ed.)

ISBN 978-951-38-7064-5 (URL: http://www.vtt.fi/publications/index.jsp)
ISSN 1455-0849 (URL: http://www.vtt.fi/publications/index.jsp)

JULKAISIJA – UTGIVARE – PUBLISHER

VTT, Vuorimiehentie 3, PL 1000, 02044 VTT
puh. vaihde 020 722 111, faksi 020 722 4374

VTT, Bergsmansvägen 3, PB 1000, 02044 VTT
tel. växel 020 722 111, fax 020 722 4374

VTT Technical Research Centre of Finland, Vuorimiehentie 3, P.O.Box 1000, FI-02044 VTT, Finland
phone internat. +358 20 722 111, fax +358 20 722 4374

VTT, Kaitoväylä 1, PL 1100, 90571 OULU
puh. vaihde 020 722 111, faksi 020 722 2320

VTT, Kaitoväylä 1, PB 1100, 90571 ULEÅBORG
tel. växel 020 722 111, fax 020 722 2320

VTT Technical Research Centre of Finland, Kaitoväylä 1, P.O. Box 1100, FI-90571 OULU, Finland
phone internat. +358 20 722 111, fax +358 20 722 2320

Technical editing Anni Kääriäinen

Edita Prima Oy, Helsinki 2007

Paaso, Janne. Moisture depth profiling in paper using near-infrared spectroscopy. Espoo 2007. VTT Publications 664. 193 p. + app. 6 p.

Keywords moisture content, depth profiling, paper coating, optical properties, near-infrared spectroscopy, NIR, fibre-optic light sources, fibre-optic probes, multichannel spectroscopy, water transport characteristics, on-line measurement, Monte Carlo modelling

Abstract

A near-infrared spectroscopic method and measurement system for moisture depth profiling is presented in this thesis. The measurement system is based on a fibre-optic light source and probes, and a hyperspectral imaging spectrograph. The probes feature six different measurement geometries, including a specular reflection measurement, and diffuse reflection and transmission measurements, all of which are measured in seven positions simultaneously. A theoretical analysis of the depth profiling capabilities of the system is presented, as well as laboratory tests of the system performance. Based on these, the analysis depth of the reflection moisture measurement in a 75 μm thick uncoated paper is estimated to be about 40 μm. It is also shown that the depth profiling properties depend on the average moisture content of the paper, and that the inclusion of a coating layer complicates the depth profiling. The use of the theoretical analysis results in the interpretation of the measurement results is also discussed.

As the main application, the measurement system was installed on a pilot-scale paper coating machine. The feasibility of semi-quantitative moisture depth profiling during the coating process is shown. The determination of the first and second critical concentrations of the coating colour consolidation process is also discussed. Detailed results from the extensive programme of trial runs are presented, along with discussion of the physics behind the measurements. It is found that the water transport characteristics measured during the coating process are not in accordance with mass and heat transfer theories in some respects. Also, the specular reflection measurement results do not behave as expected, making the determination of the first critical concentration impossible in some cases. Instead, the second critical concentration is easily detected, but does not always behave as expected. Reasons for the unexpected behaviour of the measurements are discussed, and conclusions drawn about the water transport during the coating process.

Preface

This thesis is a result of research work carried out in VTT Technical Research Centre of Finland (VTT) during the years 2004–2007. The major part of the results has been achieved in the COATME and COATME2 projects. These projects were part of a larger research consortium coordinated by Oy Keskuslaboratorio – Centrallaboratorium Ab (KCL). The projects were funded by KCL and VTT, and by Tekes – the Finnish Funding Agency for Technology and Innovation. I would also like to acknowledge the financial support from the Infotech Oulu Graduate School.

My sincerest thanks go to my supervisors, Professors Risto Myllylä (University of Oulu) and Harri Kopola (VTT), for their advice, guidance and continuing support, especially in the painful phase of finalizing the thesis.

This thesis would not have come into being without the excellent cooperation with KCL. Especially I would like to thank Mrs. Hanna Koskela, Mr. Heikki Pajari and Dr Ulla Forsström for three years full of trial runs, fruitful discussions and work towards understanding the paper coating immobilization process. I also express my gratitude to the other people at KCL who participated in the COATME and COATME2 projects. In addition, my thanks go to Metso Automation Oy, especially to Markku Mäntylä, for lending the spectral camera, and for helpful hints and suggestions.

I am also very grateful to my colleagues at VTT. Mr. Janne Suhonen and Mrs. Mari Tenhunen did great work in starting the two projects, and guiding during the projects. Mr. Jussi Tenhunen, Mr. Pekka Suopajärvi and Mr. Hannu Vasama were the main optical and mechanical designers of the measurement system. In addition, I am grateful to Jussi for introducing me to the principles of real scientific thinking. Mr. Petri Lehtonen did very valuable work in the testing of the measurement system, and in the trial runs at KCL. In addition, my thanks go to my co-researchers at VTT, who have helped me in many ways during this work and during my entire career at VTT.

And last but not least, my greatest thanks to my wife for her encouragement, support and patience during the years of work and writing of this thesis.

Oulu, November 2007

Janne Paaso

Contents

Abstract 3

Preface 4

List of abbreviations and symbols 8

1. Introduction 17
   - 1.1 Objectives of the thesis 21
   - 1.2 Contribution of the thesis 21

2. Near-infrared spectroscopy 24
   - 2.1 Fundamentals 24
   - 2.2 Near-infrared spectroscopic measurements 25
   - 2.3 Theories of near-infrared measurements 29
     - 2.3.1 Analytical models 30
     - 2.3.2 Monte Carlo models 35
     - 2.3.3 Modelling of paper samples 37

3. Paper coating consolidation 39
   - 3.1 The paper coating process 39
   - 3.2 Consolidation and critical points 41
   - 3.3 Mass and heat transfer models 45

4. The depth-profiling system and method 48
   - 4.1 Measuring equipment 48
     - 4.1.1 Configuration 48
     - 4.1.2 Probes 49
     - 4.1.3 Measurement principle 54
     - 4.1.4 Light source 56
     - 4.1.5 Fibres 58
     - 4.1.6 Spectral camera 58
   - 4.2 On-line measurements 59
     - 4.2.1 Trial runs 59
     - 4.2.2 Measurement procedure 62
     - 4.2.3 Data processing 64
   - 4.3 Measurements on laboratory coater 76

4.3.1 Configuration at laboratory coater 76
4.3.2 Coating and water spraying experiments 77

5. Determination of the optical properties 79
5.1 The inverse Monte Carlo model 79
5.2 Measurements 80
5.2.1 Instrumentation 81
5.2.2 Measurement procedure for the base paper 83
5.2.3 Measurement procedure for the coating colour 85
5.3 Optical properties of the base paper 89
5.3.1 Measurement results 89
5.3.2 Assumptions used in the calculations 90
5.3.3 The anisotropy factor 92
5.3.4 Absorption and scattering coefficients 93
5.4 Optical properties of the coating colour 95
5.4.1 Assumptions used in the calculations 95
5.4.2 The anisotropy factor 99
5.4.3 The absorption and scattering coefficients 101

6. Theoretical analysis of the measurement method 105
6.1 Monte Carlo model 105
6.2 Theoretical model for the measurement method 108
6.2.1 Approximations used in the model 108
6.2.2 Comparing simulations to measurements 109
6.3 Simulation of on-line measurements 111
6.4 Depth profiling properties of the measurement method 116
6.4.1 Definition of depth sensitivity 116
6.4.2 Depth sensitivity in base paper 120
6.4.3 Depth sensitivity in coated paper 127
6.4.4 Conclusions 132

7. Experimental results 135
7.1 Laboratory coater measurements 135
7.2 Interpretation of the on-line measurement results 139
7.3 Performance of the measurement system on-line 142
7.3.1 Signal-to-noise ratios 142
7.3.2 Comparability of measurement positions 146
7.4 On-line measurement results 148

7.4.1 Comparison between drying strategies 149
7.4.2 Effect of coat weight 151
7.4.3 Different coating colours 154
7.4.4 Different base papers 155
7.4.5 First and second critical concentrations 159
7.5 Other quantities of interest 162
7.5.1 Collimated transmission moisture 163
7.5.2 Moisture and other water bands 163
7.5.3 Scattering in all geometries 164
7.5.4 Temperature measurement by the infrared method 166
7.5.5 Water vapour 169
7.5.6 Wavelength dependence of specular reflection and scattering 171
7.6 Comparison of simulation and measurement results 172

8. Discussion and conclusions 175

9. Summary 180

References 182

Appendices
Appendix A: Mathematics of the inverse Monte Carlo model

List of abbreviations and symbols

Abbreviations

ANSI-C	standard for the C programming language
a.u.	absorbance unit(s)
BRMR	bottom reflection moisture rise
Capim SP	type of kaolin pigment
CMC	carboxymethylcellulose
CNC	computerised numerical control
DL 966	type of latex binder
DRA-2500	integrating sphere accessory of the Varian Cary 5000 spectrometer
FCC	first critical concentration
FT-NIR	Fourier transform near-infrared
HC-90	type of calcium carbonate pigment
HLL	high-low-low drying strategy
H–O–H	hydrogen–oxygen–hydrogen bond
InGaAs	indium-gallium-arsenide

KM	Kubelka–Munk
LED	light-emitting diode
LLH	low-low-high drying strategy
M1, M2	mirrors in the Varian Cary spectrometer
MCML	Monte Carlo model of light transport in multi-layer tissues
MCT	mercury-cadmium-telluride
MSSM	measurement system simulation model
NIR	near-infrared
NIRS	near-infrared spectroscopy
O–H	oxygen–hydrogen bond
Op.DI.MA	trade name for optical teflon
PbS	lead sulphide
PMT	photomultiplier tube
pph	parts per hundred
PVA	polyvinylacetate
RTE	radiative transfer equation
SCC	second critical concentration
SNR	signal-to-noise ratio

Tekes	the Finnish Funding Agency for Technology and Innovation

Symbols

A	absorbance
a , b	coefficients in the Kubelka–Munk theory
a_k , b_k	Mie coefficients
$B_{dm}^{dz}(z)$	boxcar-type test function
C	collimated transmittance
C_m	calibration function
$\tilde{C}_m$	calibration function with moisture depth profile as argument
c_n	specular reflection correction coefficient for measurement position *n*
d	thickness of sample
dm	height of the perturbation
dz	width of the perturbation
D_λ	diffuse reflectance at a certain wavelength
D_{λ_k}	diffuse reflectance at a certain wavelength
$D_{\lambda_1}, D_{\lambda_2}, \ldots, D_{\lambda_j}$	diffuse reflectances at different wavelengths

e	Napier's constant
f	test function
g	anisotropy factor
$g^{base}(m,\lambda)$	anisotropy factor function for the base paper
$g^{coating}(m,\lambda)$	anisotropy factor function for the coating colour
G_n	measured specular reflection signal at measurement position *n*
G'_n	difference quotient of specular reflection signal at measurement position *n*
G_n^{corr}	corrected specular reflection signal at measurement position *n*
$\overline{G}^{glossy}$	mean of specular reflection signals from glossy paper
G_n^{glossy}	specular reflection signal from glossy paper at measurement position *n*
I	measured intensity
I_0	intensity of the incident radiation in the Mie theory
I_R	measured intensity of the reference sample
i_1, i_2	variables in the Mie theory
$I(\tau,\mu)$	intensity of diffuse radiation in the radiative transfer equation

$I_{\theta s}$	scattered intensity in the Mie theory
K	Kubelka–Munk absorption coefficient
k	index
l	layer index
m	moisture content
$\dot{m}$	water evaporation rate
m_l	moisture content of layer l
m_{pred}	predicted moisture content
$m(z)$	moisture depth profile function
n	measurement position number
n_c	refractive index of solid particles
n_{eff}	effective refractive index
n_l	refractive index of layer l
n_{rel}	relative refractive index
n_w	refractive index of water
P_a	partial vapour pressure of surrounding air
P_{p0}	partial vapour pressure on the paper surface
P'_{sca}	refraction efficiency

$p(\mu, \mu')$	scattering phase function in the radiative transfer equation
q	heat flux in heat transfer equations
r	radius of solid particles
R , R_0	diffuse reflectance
R_d	distance from the centre of the sphere in the Mie theory
S	Kubelka–Munk scattering coefficient
s_b	solids content of base paper
s_c	solids content of coating colour
S_n	scattering signal at measurement position *n*
$S(0)$	complex forward scattering amplitude
t	time
T	diffuse transmittance
T_a	air temperature
t_c	thickness of the coating layer
T_c	temperature of hot cylinder surface
t_l	thickness of layer *l*
t_n	time at measurement position *n*

T_{p0}	temperature of the paper web
V_c	total volume of the coating colour
V_s	volume of solids
V_w	volume of water
w_c^s	grammage of solid materials in the coating layer
w_l^s	grammage of solid materials in layer l
w_l^w	grammage of water in layer l
x	the x-coordinate in the plane of a sample
x_r	size parameter
y	the y-coordinate in the plane of a sample
z	coordinate in the thickness direction of a sample
z_0	position of the perturbation
z'	depth coordinate of the spectral depth sensitivity function
α	angle between paper surface normal and the optical axes of the probes
α_{a-p}	convective heat transfer coefficient
α_{c-p}	contact heat transfer coefficient
β_{a-p}	mass transfer coefficient

δD_λ	functional derivative of diffuse reflectance
Δm	finite height of the perturbation function
Δz	finite width of the perturbation function
$\Delta_m^C(z')$	application-specific depth sensitivity
$\Delta_\lambda(z')$	spectral depth sensitivity function
ε	parameter used in evaluating the functional derivative
θ	angle of ray in the radiative transfer equation
θ_s	scattering angle in the Mie theory
θ'	angle of scattered ray in the radiative transfer equation
λ	wavelength of light
μ	cosine of angle of ray in the radiative transfer equation
μ_a	absorption coefficient
μ_s	scattering coefficient
$\mu_a^{base}(m,\lambda)$	absorption coefficient function for the base paper
$\mu_s^{base}(m,\lambda)$	scattering coefficient function for the base paper
$\mu_a^{coating}(m,\lambda)$	absorption coefficient function for the coating colour

$\mu_s^{coating}(m,\lambda)$	scattering coefficient function for the coating colour
μ'	cosine of angle of scattered ray in the radiative transfer equation
ν_s	volume fraction of solids
ρ_b	density of base paper
ρ_c	density of coating colour
ρ_w	density of water
τ	optical depth
ω_0	albedo

1. Introduction

Near-infrared (NIR) spectroscopy is one of the well-established branches of spectroscopy. In addition to purely academic interest, it also has a wide variety of practical applications. They range from moisture, protein, fat and carbohydrate content measurement in the food industry [1] to on-line quality control gauges in the paper industry [2–4]. Due to the relatively strong absorption bands of water in the near-infrared spectral region [5], the moisture content measurement of different samples is the most popular application of NIR spectroscopy. Another reason for this is the importance of knowledge of the moisture content in many industrial processes.

In the pulp and paper industry there are two substances present in every phase of paper-related production: the wood or cellulose fibres, and water. The fibres are the main raw material, but many process properties are controlled or dictated by water: removal of water in the wet end [6], in the drying sections [7] and absorption of water into the base paper in the coating process [8], to mention only a few. The importance of moisture content from the point of view of process control is also high: it affects the runnability and quality of the end product in paper machines [9]. In addition, the main reason for the high energy consumption of paper mills is the removal of water from the paper [10]. Thus optimal control of the drying processes is a key issue in every paper mill.

Due to the importance of water in the paper processes, the measurement of moisture, or water, has attained great interest during the decades of modern paper manufacturing. The gravimetric method [11] has the longest history, but it is not suitable for on-line measurements. The most important on-line measurement methods include microwave-based techniques [11, 12], methods based on impedance [13, 14] and techniques based on near-infrared spectroscopy [11, 15]. Of these, the near-infrared technique is nowadays the most popular; it offers a fast and reliable non-contact measurement, which is suitable for a wide variety of basis weights from very low-grammage printing papers to board grades of relatively high basis weight [15]. Furthermore, the technique can be used to measure low-grammage papers, tissue and board in the wet end [16, 17] and dry end in the paper machine, as well as in the coating machine [3, 18].

One of the most important techniques used to tailor the properties of the end product is applying one or more coating layers onto the paper. The main purpose is to make the printing properties and appearance of the paper better. In the paper coating process, wet coating colour is first applied onto the base paper, and then the paper is dried using infrared, air flow or cylinder driers [19]. During the drying, the coating colour undergoes a transition from a wet suspension to a rigid solid structure. This is called the paper coating consolidation or immobilisation process [20].

Conventionally, the immobilisation process of paper coating has been mainly described by the so-called first and second critical concentrations, or critical points [20]. Specular reflection and diffuse reflection intensity measurements, among others, have been used to determine these points. The measurements related to the immobilisation process have mainly been conducted on the laboratory scale [20–24], but on-line measurements have also gained attention [25]. Honeywell Inc. has introduced a product called the GelView system to measure and control the critical points [2, 26–28]. In these papers, the behaviour of specular and diffuse reflection in the paper coating process has been thoroughly studied.

With specular and diffuse reflection measurements the state of the coating immobilisation can be determined, i.e. the first and second critical points. However, very crucial to the understanding of the coating process is to know the behaviour of water. Water moves off the coating layer in two ways: through surface evaporation and through penetration into the base paper. These processes depend on the drying conditions, but also on the physical and chemical properties of the coating colour and the base paper. These issues have received a lot of interest in paper coating research [29–32] since it has been shown that they have an effect on the end product quality, especially on mottling and printability [33–35]. In these papers, the effect of drying conditions and drying optimisation on end-product quality were studied, and simulations and laboratory experiments were performed to gain understanding of the evaporation and absorption of water into the base paper. However, direct on-line measurements of the water transport during the coating process have been lacking.

It is obvious that extensive measurements both in the laboratory and on-line are needed to gain more understanding of the coating process. Measurement of the

depth profile of water during the coating process would give new insight into the process. Supplied with suitable data processing and theoretical analysis of the properties of the measurement, such measurements would also allow the development of more realistic theories on the physical and chemical changes taking place during the coating process.

Despite its importance in the paper coating process, and in many other industrial processes, the depth profiling of moisture has attained surprisingly little interest in the literature. Batchelor et al. proposed a method based on impedance between copper sheets placed in a stack of papers [13]. A somewhat similar approach was used by Gupta et al. [36]. As these techniques need a paper stack as a sample, they are not suitable for on-line use. Leisen et al. [37] used magnetic resonance imaging to monitor the diffusion of water in paper samples. Very recently, Fabritius et al. used optical coherence tomography to follow liquid penetration into paper samples [38, 39]. While this technique gives superior depth-profiling resolution, it is too slow for on-line use.

Because of the limited penetration depth of near-infrared radiation, the NIR diffuse reflection measurement is inherently sensitive to the surface layers of the sample [40, 41]. Despite this property, there are very few articles on moisture depth profiling based on NIR spectroscopy. Boström used diffuse reflectance measurements from both sides of paper samples to deduce qualitative moisture depth profiles in laboratory and process conditions [42]. A natural third measurement to add is the NIR transmission measurement through the paper. The combination of diffuse reflection from both sides of the paper and the transmission measurement gives more information for depth profiling. However, such approaches have not previously been presented in the literature until this work.

Near-infrared measurements are sensitive to scattering changes in the sample [43]. The coating paste and the base paper have different scattering properties, and the scattering properties also depend on the moisture content. Spectral preprocessing methods to deal with scattering variations exist [43]. However, these methods are mostly suited to situations where NIR spectroscopy is used as a secondary measurement method, requiring a concentration reference method. When used in moisture depth profiling, NIR spectroscopy is usually a primary measurement method, since typically there are no reference methods available.

Hence the spectral preprocessing methods can only be used with care. This complicates analysis of the moisture depth profiles obtained since the response of the NIR measurement can change when the scattering properties of the sample change.

To overcome the problems associated with scattering changes, theoretical analysis of NIR spectroscopy used as a depth-profiling tool would be needed. Fortunately, the behaviour of near-infrared radiation in scattering samples has been studied extensively from the theoretical point of view. The theories can be roughly divided into analytical models [44–47] and Monte Carlo methods [48–50]. Some of the models are specifically intended to model the behaviour of light in paper [45, 50]. However, the depth profiling properties of NIR measurements have not been extensively studied theoretically; mainly, the penetration depth of infrared radiation in the sample has attained interest [40, 41]. On the other hand, the radiation transfer models and Monte Carlo methods mentioned above would offer rather straightforward ways to investigate the depth profiling properties.

There are a number of NIR measurement technologies capable of on-line operation. Filter wheel-based devices [51] and array spectrometers [52, 53] are the most common, although Fourier transform spectrometers have also been used on-line recently [54]. The paper coating process is a rather harsh environment; humidity and temperature are high, and contamination from the paper and coating colour can also occur. Fibre-optic probes are a good choice for such environments. Usually, they are used with array spectrometers with suitable fibre-optic light sources, but fibre-optic probes can be used with virtually any near-infrared spectroscopic device or spectrometer.

Depth profiling of moisture during the coating process actually means a multipoint measurement to really follow the process. Moreover, as discussed earlier, NIR moisture depth profiling is a multiple-geometry measurement. Thus a combination of multipoint and multiple-geometry measurement leads to a large number of measurement channels. In principle, this can be achieved either by using several measurement instruments or by using a single measurement instrument and a fibre-optic multiplexer. However, the hyperspectral imaging spectrographs [55] with fibre inputs offer a very powerful alternative. They feature simultaneous full spectrum measurement from tens or even hundreds of

input fibre channels in the visible and near-infrared spectral ranges. Thus, for example, the combination of three measurement geometries at seven measurement positions is easily possible. The continuous spectral measurement offers also an advantage in researching the depth-profiling possibilities since the spectral information can be fully exploited.

1.1 Objectives of the thesis

The main goal of this thesis is to develop an on-line-capable measurement system and method for moisture depth profiling in paper samples. The main application is the paper coating process. From the application point of view, the more specific goals of the thesis are:

1. Measuring the moisture depth profiles along the coating process.
2. Finding the first and second critical points of the coating colour immobilisation.
3. Based on 1 and 2, development of an in-depth understanding of the water transport mechanisms and coating immobilisation characteristics along the coating process.

From the measurement technology point of view, the more specific goals of the thesis are design, fabrication, installation and testing of the on-line moisture depth profiling system, and theoretical analysis of the moisture depth profiling performance of the system.

1.2 Contribution of the thesis

The scientific work in the thesis can be roughly divided into technical, theoretical and application-related parts. Chapters 1, 2 and 3 are introductory. The technical part, Chapter 4, includes the design and fabrication of the measurement instruments, and development of the measurement method and measurement data processing. The theoretical part, Chapters 5 and 6, involves the development of a theoretical model of the measurement method, and using

the model to analyse the depth-profiling properties of the measurement. The experimental and application part, Chapter 7, concerns the tests of the measurement system in laboratory, using it in a pilot paper coating machine, and analysing the measurement results in detail.

The results of this thesis have been achieved in close collaboration between VTT and Oy Keskuslaboratorio Ab (KCL). KCL set the main objectives for the measurement system, and took part in the general design of the measurement system. The cooperation extended to the testing and use of the measurement system in laboratory and on-line conditions. The arrangements for the on-line coating trials were KCL's responsibility, as well as the use of the measurement results in understanding the coating process. In the remainder of this section, the contributions of the author are briefly summarised.

The detailed design of the measurement system was done by the author and Mr. Pekka Suopajärvi and Mr. Jussi Tenhunen at VTT. The author also took part in the specification and design phase of the measurement instruments, although the actual optical and mechanical design was carried out by design engineers at VTT. The fabrication and assembling of the instruments was also done at VTT.

The author developed the measurement method used in the laboratory and on-line, as well as the data processing methods and tools. The measurement and data processing methods are partly based on conventional spectroscopic practices, but some new methods specifically suited to this particular measurement system were developed. The laboratory measurements were carried out, or supervised by, the author. In the on-line measurements, the author was the person responsible for the working of the whole measurement system.

In the theoretical modelling part, the author developed the models for the coated paper samples, as well as the inverse models for the determination of the optical properties of the samples. These models are mostly based on techniques well described in the literature, but, especially in the modelling of the coated paper samples, new techniques to simulate the expected signals from near-infrared measurements were developed. The theoretical analysis methods of the moisture depth profiling performance of the measurement are a novelty, and were developed by the author.

To the author's knowledge, multipoint moisture depth profiling based on NIR spectroscopy has not been presented earlier in the literature, except for the author's own recent publications. And the theoretical analysis of the NIR moisture depth profiling method is scientifically a new result. Moreover, extensive optical measurements in the paper coating process with a thorough analysis of the water transport characteristics have not been published earlier. Some of the results of this thesis have been published in [56] and [57], and the author has also contributed and supervised the NIR measurement simulation results of Kurki et al. [58].

2. Near-infrared spectroscopy

The fundamentals, techniques and theories related to near-infrared spectroscopy (NIRS) are briefly reviewed in this chapter. Different near-infrared measurement instruments are described, along with a summary of typical measurement geometries. Finally, the theories used to model near-infrared measurements in scattering samples are introduced.

2.1 Fundamentals

According to [59], near-infrared spectroscopy can be briefly defined as follows:

Near-infrared spectroscopy is the measurement of the wavelength and intensity of absorption of near-infrared light by a sample.

The NIR spectral region spans from 700 to 2500 nm. The lower wavelength limit is the limit between visible and infrared light, whereas wavelengths greater than 2500 nm belong to the mid-infrared spectral region. The fundamental difference between the mid-infrared and near-infrared spectral regions is that, with most samples, the spectral features in the mid-infrared region originate from the fundamental vibrations of the molecules, whereas in the near-infrared region the absorption bands are related to the combination and overtone modes of the fundamental vibrations.

The measurement of moisture depth profiles is the main goal of this thesis. The measurement of moisture with near-infrared spectroscopy is based on the vibrations of the water molecule and the absorption features they cause in the NIR spectral region. In the liquid phase, the water molecule has three vibrations [60]:

- Symmetric O–H stretching vibration (ν_1)
- H–O–H bending vibration (ν_2)
- Asymmetric O–H stretching vibration (ν_3).

The spectral bands of water observed in the NIR spectral range are 970 nm, 1200 nm, 1440 nm and 1940 nm [5]. All these are combinations and overtones of the primary vibrations shown above. Thus the NIR water bands are relatively weak. However, the 1440 nm and 1940 nm bands are strong enough to be suitable for paper moisture content measurement. Kuusela has presented a thorough study on the NIR moisture measurement of paper, board and pulp [15].

2.2 Near-infrared spectroscopic measurements

The applications of near-infrared measurements are numerous. In this section, fundamentals of near-infrared spectroscopic measurements are briefly reviewed from the instrumental point of view. The word "spectroscopic" is used in this thesis to refer to measurements involving at least two wavelengths, i.e. measurements that exploit the information in the spectral dimension in some way. This is to make a contrast to NIR imaging systems, where the spectral information is not usually used in any way.

In a typical NIRS measurement application there are four basic parts to the measurement system:

1. the illumination unit
2. the sample or process interface
3. the dispersive component
4. the detection unit.

The illumination unit provides the light, which is then led to the sample interface in some way, for example by the use of mirrors or by using fibre-optics. The illumination optics of the sample interface focuses the light on the sample, and the transmitted or scattered light is then collected with the collection optics of the sample interface. The detection unit converts the collected radiation into an electrical signal. In a spectroscopic measurement, the dispersive component has to be included in some point of the illumination – sample interface – detection chain.

There are numerous alternatives for each of the basic parts of an NIRS measurement system. The most common choice for illumination unit is a halogen lamp with suitable collection optics. LEDs are an emerging alternative [61]. The sample or process interface can be a fibre-optic probe, a diffuse or specular reflection accessory, an integrating sphere, or a normal transmission cuvette, to mention only a few. The detection unit can incorporate one detector, a multichannel detector, a row detector, or a matrix detector. There are also several choices for the detector material – silicon, indium-gallium-arsenide (InGaAs), lead sulphide (PbS) and mercury-cadmium-telluride (MCT) being the most common in the NIR spectral range. The detection unit also includes the electronics to collect the photoelectrons or to measure the current caused by the collected photons. The dispersive unit can be based on a static or an oscillating grating, on optical filters, or on interferometric techniques. Moreover, the light source can also provide some wavelength discrimination capability. For example, LEDs have a relatively narrow emission band and their emission wavelength can be tailored [61].

Different NIRS measurement techniques are obtained through combination of different alternatives of the four basic parts mentioned above. During the past decades the number of different measurement techniques has increased rapidly. According to [62], the devices can be categorised into monochromator-based devices, array spectrometers, miniature spectrometers, tuneable filter and discrete filter devices, Hadamard transform spectrometers, and spectrometers based on infrared-emitting diodes. A natural supplement to this list are the Fourier transform near-infrared (FT-NIR) spectrometers, which are not, however, usually restricted to the NIR spectral range alone. Spectrometers based on a NIR matrix array can also be regarded as a separate category of NIR spectrometers [55]. The fixed-wavelength instruments include, among others, filter wheel devices [3, 51], linear variable filter devices [51] and instruments based on multi-channel detectors [63].

Of these, the discrete filter devices are best suited to on-line use, but rugged array spectrometers and FT-NIRs are becoming more and more popular in process analyser use. The benefits of discrete filter devices are relatively low cost, ruggedness, fast operation, simplicity and small size. The major drawbacks are the loss of information due to the limited number of wavelength channels, and the inflexibility in changing these channels. For the array spectrometers and

FT-NIRS, the benefits and drawbacks are almost the opposite to discrete filter devices. The array spectrometers offer a fast full-spectrum measurement with a relatively good signal-to-noise ratio. As drawbacks, the wavelength range in a single instrument is limited, the wavelength stability and accuracy can be a problem, and there can also be problems with the temperature stability. The FT-NIRs offer a powerful alternative in terms of wavelength accuracy, resolution and spectral range, but their cost, size and sensitivity to vibrations are the main challenges in on-line applications.

When considering a need for multipoint measurements, the alternatives become more restricted. Of course, multiple instruments can always be used, but in addition to the cost issue, the data acquisition, instrument-to-instrument variations and maintenance rapidly become challenging when the number of measurement positions is increased. This is especially true when performing NIRS multipoint measurements in on-line conditions. For such applications, fibre-optic probes offer the best approach in many cases. However, almost all NIRS fibre optic measurement systems employ array spectrometers with only one fibre input. If multipoint measurements are needed, one must resort to some kind of multiplexing techniques, or use many instruments simultaneously.

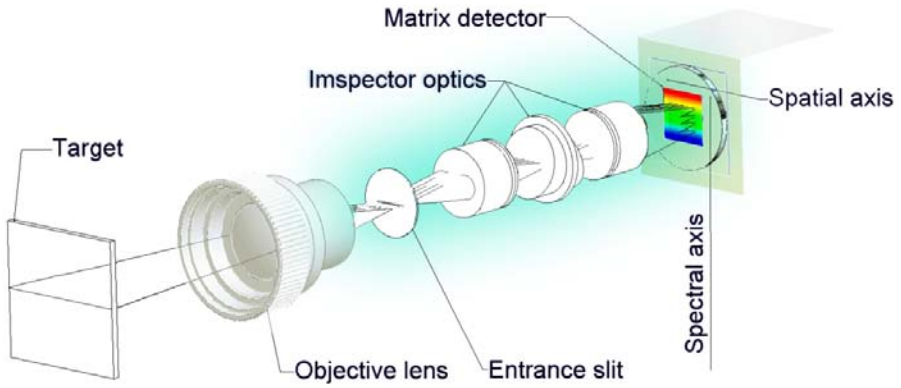

Figure 1. The operation principle of a spectral camera. Picture courtesy of Specim Ltd, Oulu, Finland.

The so-called spectral cameras offer a powerful alternative for spectral imaging and multipoint measurements [55]. The spectral cameras are based on a hyperspectral imaging spectrograph, and a matrix detector. Similar to the conventional array spectrometers, there is an entrance slit, collimating and focusing optics and a grating to disperse the light coming into the entrance slit into a spectrum (see Figure 1). The dispersed light is detected with a matrix detector. In contrast to conventional array spectrometers, the matrix detector resolves the incoming light both spatially and spectrally. Thus the spectral camera yields a line image of the target with a continuous spectrum.

The spectral cameras can be equipped with a fibre bundle that has tens or even hundreds of separate fibres in one end and a bundle of fibres in the other end. The fibres in the bundle are arranged in a row, which is suited to the input slit. Spectral cameras having a fibre-optic bundle can measure a continuous spectrum from even hundreds of fibre input channels simultaneously. All this can be done in a fraction of a second, resulting in tens or hundreds of measurements per second. These features are unique in the field of NIRS measurements.

The massive-parallel measurement capability of fibre-optic spectral cameras opens up new possibilities in multipoint measurements. In process industry applications, the process can be followed in many positions simultaneously, for example in machine direction, cross direction, or both, in a paper mill. Another new possibility is to add multiple geometries in one measurement position. These geometries could include, for example, collimated transmission, angle-resolved diffuse reflection and transmission, specular reflection, spatially resolved diffuse reflection and so on. The use of polarisation of light is also possible in conjunction with the aforementioned geometries. When one adds the possible combinations of the above, the number of different multiple-geometry measurement possibilities approaches infinity.

One of the objectives in this work is to develop instrumentation to measure the depth profile of water in multiple positions along the drying section of a paper coating machine. The depth profiling needs a multiple-geometry measurement, in which at least two different geometries are used. This leads to a combination of multipoint and multiple-geometry measurement, which will be referred to as *multimeasurement* hereafter. A more detailed description of the multimeasurement system developed is presented in Chapter 4.1.

In the laboratory, the combination of measurement results in different geometries has been used for decades, if not centuries. In contrast, on-line NIR spectroscopic multimeasurements have not been reported earlier in the literature. Multipoint single-geometry NIRS measurements have been used in commercial products [16, 17]. On the other hand, multipoint multiple-geometry measurements are used in the Honeywell GelView system [2, 26–28], but it does not work in the NIR spectral range and it is not a spectroscopic measurement. A kind of single-point multiple-geometry NIRS measurement was introduced by Boström [42]. The lack of articles on multipoint multiple-geometry measurement systems is probably related to the novelty of the fibre-optic spectral cameras.

2.3 Theories of near-infrared measurements

Near-infrared spectroscopic measurements usually deal with inhomogeneous, scattering and absorbing samples. Such samples are often referred to as *turbid samples*. This is in contrast to homogeneous liquid or solid samples, where light scattering does not occur. Nevertheless, the spectroscopic practices originally developed for non-turbid samples are often employed with turbid samples. Specifically, the measured reflectance or transmittance signals are converted into absorbance,

$$A = -\log_{10}\left(I / I_R\right), \tag{1}$$

where I is the measured intensity and I_R is the intensity of the reference sample. The resulting quantity, A, is said to be in absorbance units, although, strictly speaking, absorbance "units" do not exist. For convenience, signals converted into absorbance will be referred to as being in the absorbance units in this thesis, and denoted briefly by a.u. In absorbance units, the relation between the absorption band height and concentration of certain substances is often linear, despite the fact that the absorbance contains information on both the absorption and scattering properties of the sample. This is often sufficient, and any further analysis of the generation of the NIR signal in the sample is not needed. Also, one can qualitatively follow the changes in the scattering properties of the sample by monitoring the diffuse reflection or transmission intensities.

In many cases, however, the simple calculation of absorbance spectra is not sufficient. One may be interested in the origin of the scattering and its relationship to the structural properties of the sample, or in the penetration depth of the NIR radiation. Of course, there is also the purely academic interest to be able to explain the generation of diffuse reflection and transmission signals. These desires have resulted in the development of a wealth of theories for behaviour of radiation in turbid samples.

The models can be roughly divided into two categories: analytical models and Monte Carlo models. The analytical models describe the reflected or transmitted signals in the form of an analytical expression. The Monte Carlo models, on the other hand, describe the propagation of photons or light rays in the sample as a stochastic process. They require always a computer simulation to get any results. There are also semi-analytical models, which require a numerical solution to the expressions of scattered radiation. The main benefits of analytical models are the calculation speed and that they increase the understanding of the underlying physical mechanisms. The drawback is that they are only valid in the framework of their assumptions, which restricts their use to simple measurement configurations. The Monte Carlo models, on the other hand, offer a flexible and exact solution to most problems, but only at the expense of calculation time and numerical accuracy. The analytical and Monte Carlo models are briefly reviewed in the following sections.

2.3.1 Analytical models

One of the most well known light scattering theories is the one developed by Mie in 1908 [64]. It describes the scattering of a plane wave from an isolated sphere, and is derived from Maxwell's equations by the use of spherical harmonic expansions [65]. The Mie theory relates the scattered intensity to the properties of the sphere in the following fashion:

$$\frac{I_{\theta s}}{I_0} = \frac{\lambda^2}{8\pi^2 {R_d}^2}(i_1 + i_2) \qquad (2)$$

where $I_{\theta s}$ is the scattered intensity at a distance R_d from the centre of the sphere, and I_0 and λ are the intensity and wavelength of the incident radiation. The variables i_1 and i_2 are functions of the scattering angle θ_s, the complex refractive indices of the sphere and the surrounding medium, and the size of the sphere divided by the wavelength of the incident radiation.

The Mie theory describes the scattering of light by only one particle, and should therefore only be applied to samples where the particles are well separated. One can still deduce some important properties of scattering samples from Equation (2). The most important result of the Mie theory is that the angular distribution of the scattered radiation is not, in general, isotropic. In particular, when the particle size is greater than the wavelength, pronounced forward scattering occurs. However, the Mie theory does not take multiple scattering into account, or the interference effects caused by the densely packed particles in a typical inhomogeneous solid sample.

Perhaps the most popular approach to deal with multiple scattering phenomena is provided by the so-called *radiative transfer equation* (RTE). It has been extensively studied by Chandrasekhar [66]. The RTE assumes that the light propagates through a homogeneous sample, where the optical properties are described by the following parameters:

- μ_a: the absorption coefficient. Describes the decay of the intensity of a light ray due to absorption by the medium.

- μ_s: the scattering coefficient. Describes the decay of the intensity of a light ray due to scattering in any direction.

- $p(\mu, \mu')$: the scattering phase function, describing the probability of a photon being scattered from direction θ to θ', with $\mu = \cos\theta$ and $\mu' = \cos\theta'$. The polar angles θ and θ' are measured relative to the incident direction of the radiation.

- $\tau = (\mu_a + \mu_s)z$: the optical depth, where z is the coordinate in the thickness direction of the sample.

- $\omega_0 = \mu_s / (\mu_s + \mu_a)$: the albedo.

In the special case of a sample consisting of plane parallel layers, i.e. a one-dimensional model, the RTE can be written as follows [66, 67]:

$$\mu \frac{\partial I(\tau,\mu)}{\partial \tau} = -(\mu_a + \mu_s) I(\tau,\mu) + \frac{\mu_s}{2} \int_{-1}^{1} p(\mu,\mu') I(\tau,\mu') d\mu' \qquad (3)$$

where $I(\tau,\mu)$ is the intensity of the diffuse radiation emerging from multiple scattering events. The scattering phase function $p(\mu,\mu')$ is normalised to 2 when it is integrated over all directions.

The scattering phase function is usually described by some parameters. The most important of these is the so-called anisotropy factor *g*. It is the first moment of the scattering phase function:

$$g = \frac{1}{2} \int_{-1}^{1} p(\mu,\mu') \mu' \, d\mu' \qquad (4)$$

Often, the scattering phase function is written as a function of the angle θ_r between the incident and scattered rays, $p(\mu,\mu') = p(\theta_r)$. A parametric expression for the scattering phase function was proposed by Henyey and Greenstein in 1941 [68], originally for galactic scattering. The Henyey–Greenstein function expresses the scattering phase function with *g* as the parameter:

$$p(\theta_r) = \frac{1 - g^2}{\left(1 + g^2 - 2g\cos\theta_r\right)^{3/2}} . \qquad (5)$$

This approximation is widely used to describe anisotropic scattering.

A large number of different approximations have been proposed to solve the RTE, Equation (3). Even exact solutions have been presented by Chandrasekhar [66]. In the following, emphasis is put on relatively simple approximations, which can be readily applied in the analysis of NIR spectra. Most of the approximations are based on discretising the intensity $I(\tau,\mu)$ to several directed radiation fluxes, which leads to a system of differential equations. Upon

solving the system of equations, one can compute the diffuse reflection and transmission intensities.

Probably the most well known approximate solution to the RTE is the Kubelka–Munk (KM) theory [44]. The most important approximations introduced by it are the following:

- The sample is treated as a homogeneous slab of material.
- The sample surface is parallel to the *xy* plane, and the sample has infinite dimensions in the *xy* plane. The *z* axis is perpendicular to the sample surface.
- The radiation fluxes travel in two opposite directions, namely, +*z* and -*z*.
- The sample scatters isotropically, and specular reflections are ignored.
- The incident radiation is diffuse.

These approximations lead to a set of two coupled differential equations, which can be solved to yield the radiation fluxes at the sample surfaces. From these, the formula for diffuse reflectance can be computed [69]:

$$R = \frac{1}{a + b\coth(bSz)} \tag{6}$$

where

$$\begin{aligned} a &= 1 + \frac{K}{S} \\ b &= \sqrt{\left(\frac{K}{S}\right)^2 + 2\frac{K}{S}} \end{aligned} \tag{7}$$

For the diffuse transmittance, one gets [69]

$$T = \frac{b}{a\sinh(bSz) + b\cosh(bSz)} \tag{8}$$

In these equations, the K and S are the absorption and scattering coefficients, respectively, defined in the framework of Kubelka–Munk theory. They differ from the μ_a and μ_s that are incorporated in the RTE (Equation (3)). In KM theory, only scattering to the forward direction (i.e. to the forward hemisphere) contributes to the scattering coefficient, whereas the RTE scattering coefficient describes scattering into *any* direction. Correspondingly, the KM absorption coefficient is related to the absorption of diffuse radiation in a layer, whereas the RTE absorption coefficient describes the decay of a collimated light beam. In comparing the results from models based on the RTE coefficients with the KM theory results, these differences have to be taken into account.

The Kubelka–Munk theory is widely used in predicting the reflectivity or transmissivity of different kinds of samples, and is especially popular in the paper industry. However, it is a relatively simple approximation, mostly because of the two-flux approach. It cannot account for the propagation of radiation in the x or y directions, for example. To overcome these kinds of restrictions, solutions incorporating more fluxes have been proposed [70–72]. A somewhat different approach is the so-called discrete ordinates approximation, which discretises the integral in Equation (3) using several directions with the quadrature approximation using Jacobi polynomials [66].

In a typical measurement configuration, the illumination is collimated. The discrete ordinates approximation has been adapted to account for this situation as well. A three-flux model with an additional directional impinging flux has been developed by Kuhn et al. [73]. They give analytical formulas for the diffuse reflectance and transmittance as a function of optical thickness and albedo. This model is in excellent agreement with the exact solution to the radiation transfer equation [46].

A completely different approach to the solution of the radiation transfer equation is provided by the diffusion approximation, where the flow of photons in a sample is described as a diffusion process [74, 75]. The diffusion approximation is often used in biomedical optics, where the scattering coefficient is usually much larger than the absorption coefficient. In such situations, the diffusion

approximation works well. Increasing deviations from the exact solution to the RTE are encountered with lower albedos [46].

All the models discussed above fall into the category of *continuum theories*, which deal with the sample as a continuous medium, with the continuous absorption and scattering coefficients. The fact that the sample consists of particles is neglected completely. The continuum theories are good at describing samples with small particles, but when the particle size begins to be greater than the wavelength, the applicability of the continuum theories becomes more questionable. In such cases the *discontinuum theories* should have an advantage [47]. In them, the structure of the sample is taken into account. For example, the sample is thought of as being built from layers, whose absorption, reflection and transmission properties are derived from the properties of the particles the layers are comprised of.

Although the discontinuum theories offer a more rigorous treatment to the modelling of radiation behaviour in turbid samples than the continuum theories, they have not gained high popularity. One reason is that many of the inhomogeneous samples encountered in NIRS measurements are structurally very complex and thus difficult to treat with the discontinuum models. A very good example of this is coated paper.

2.3.2 Monte Carlo models

Analytical or semi-analytical models to solve the radiation transfer problem were discussed in the preceding section. As the speed of the computers has increased, so the applicability and popularity of Monte Carlo methods has grown. In this thesis, “Monte Carlo” means methods that use computer programs to simulate the behaviour of separate light rays or photons migrating in a turbid sample. This is in contrast with the analytical models, which try to describe the behaviour of light inside a sample in terms of radiation fluxes, i.e. as scalar or vector functions of the position.

There are two main advantages of the Monte Carlo methods. First, the radiation transfer problem can be described, at least in principle, as exactly as desired. Second, the solution provided by Monte Carlo is exact. The illumination and

collection of radiation can be easily modified to correspond to the experimental arrangement. The structure of the sample, and light behaviour inside it, can also be modelled accurately. The exactness of the solution is limited by the statistical nature of the Monte Carlo method, which means the accuracy of the results is highly dependent on the computation time. With modern computers, this is not normally a big issue however. In addition, it should be borne in mind that the Monte Carlo result is only exact within the framework of the assumptions used in the model; for example, if polarisation effects are not taken into account in the Monte Carlo code, the solution is only exact up to the point where polarisation effects have some importance.

A large number of different Monte Carlo models have been proposed [48, 50, 76]. They differ in the geometrical description of the sample, in the treatment of optical properties and their impact on the ray propagation, the implementation of the Monte Carlo algorithms, and in many other aspects. The rule of thumb is that the more complex the model, the more accurate it is in describing a particular modelling problem, but also the slower and more difficult to use.

In measurement applications the so-called plane-parallel layers approximation is often sufficient. It describes the sample as a collection of planar layers, which are infinite in the *xy*-direction but have finite thicknesses in the *z*-direction. An example of a Monte Carlo algorithm using the plane-parallel layers approximation is the so-called MCML Monte Carlo code by Wang et al. [48]. The parameters in the algorithm include the absorption and scattering coefficients, the anisotropy factor and the refractive index of the layers. The layers are treated as homogeneous and light polarisation is not taken into account. The ANSI-C code for this algorithm is available on the Internet. The algorithm has been well tested and is used throughout the world, especially in biomedical applications.

Monte Carlo algorithms for more complex geometries have also been developed by many authors. For example, Boas et al. developed a three-dimensional Monte Carlo code that is capable of handling spatially varying optical properties [76]. As an example, they calculated the time-resolved photon migration through a three-dimensional model of the human head. Green et al. developed a three-dimensional structural model of paper and used Monte Carlo techniques to

describe light propagation inside the model paper sample [50]. Polarisation effects can also be included in the Monte Carlo simulations [77].

It is expected that Monte Carlo techniques will become more and more popular in the future. The main driving force is the ever-increasing computation capability of computers. Although sophisticated three-dimensional Monte Carlo models are possible, and the calculation times of such models are becoming shorter and shorter, there is still room for simple models. For example, the simulation of an NIR diffuse reflection spectrum with 512 wavelengths and 0.01 per cent accuracy is time-consuming, even with the relatively simple plane-parallel Monte Carlo codes. Moreover, analytical models are superior to Monte Carlo models when their approximations correspond well to the characteristics of the measurement. A good example of this is the integrating sphere measurements, which can often be adequately described by the three-flux model [78–80]. On the other hand, hybrid analytical – Monte Carlo models have also been proposed [49].

2.3.3 Modelling of paper samples

The modelling of light propagation in paper samples has received quite a lot of interest in the literature [44, 45, 50, 81–84]. The main reason is that the light scattering and absorption properties of paper are closely related to its opacity and brightness, which belong to the most important properties of paper. On the other hand, modelling the drying effect of infrared dryers leads to modelling the propagation of infrared light in paper [85].

The problem with modelling the behaviour of radiation inside paper is that the structure of the paper is very complex. The base paper consists of fibres, fine particles and fillers [86, 87]. The coating layer contains at least pigments (kaolin and calcium carbonate are the two most common) and some binder (latexes, for example). Usually, different auxiliary substances, such as optical brighteners, are also used to tailor the properties of the paper or the coating layer. Many of the particles of these substances are far from being spherical. A good example of this is the processed wood fibre in paper, which is usually in the form of a misshapen hollow cylinder. The length of the fibre is in the millimetre range,

and the thickness in the micrometer range. The inner and outer surfaces of the fibre have also some structure on the sub-micrometer scale [88].

The complete geometrical and statistical description of the structure of a typical paper sample is a very demanding task. Modelling the behaviour of light in such a sample is even more difficult. Attempts in this direction have been made [50, 81, 82], but the models are too complicated to use in the analysis of spectroscopic data. Because of these difficulties, most models reported in the literature are phenomenological. The paper is either assumed to be homogeneous, or its structure is simplified drastically. The radiation field is described by several radiation fluxes, or statistically by Monte Carlo techniques. The physical and chemical properties of the paper are described by effective parameters, such as the scattering and absorption coefficients.

The widely used Kubelka–Munk model [44] was originally developed for predicting the coverage of inks, but over decades it has become one of the standard models used in the paper industry. Scallan and Borch [45] described the paper as a series of alternating cellulose–air layers, and derived an expression for the reflectance of the paper based upon considerations of light reflection and transmission in these layers. The predicted reflectance agrees quite well with the measured value. The main advantage of the Scallan–Borch model is that it relates the structural and optical properties of the fibres to the reflectance. The Scallan–Borch model has also been used in the modelling of infrared radiation in paper [85] in an attempt to model the effect of infrared dryers. A kind of Scallan–Borch model ideology was adopted by Carlsson et al. in their Monte Carlo calculations of time-resolved light propagation in paper [84].

In addition to modelling the behaviour of radiation inside paper samples, the specular reflection occurring on the surface of the paper has also received attention. For example, Lettieri et al. developed a model for the angularly resolved specular reflection, and obtained a good correspondence between the model and experiments [83].

3. Paper coating consolidation

This chapter introduces the consolidation process of paper coating colours. First, the fundamentals of the paper coating process are presented, then the consolidation process is described along with the concepts of the first and second critical concentrations. Finally, the theoretical models used in describing the mass and heat transfer processes during the paper coating process are very briefly reviewed.

3.1 The paper coating process

The papermaker can modify and tailor the properties of the final product by coating the paper. The most important reason for coating the paper is the improvement of the visual appearance and printing properties of the paper [19, 89]. The coating improves opacity, smoothness and gloss, and the ink absorption decreases. These are all desirable properties. On the other hand, the mechanical strength and stiffness decrease when compared to uncoated papers of the same basis weight, which is undesirable [19, 89]. In this thesis, coating refers to aqueous pigment coating of paper. Other coating types are covering the paper surface with plastic or wax, for example [19].

The coating colour recipe, coat weight, the type of base paper, and the running speed are the most common variables that can be changed in the coating process. By changing the ingredients of the coating colour, one can affect the properties of the end product, but also tailor the runnability properties, e.g. the water retention characteristics [19]. The coating colour consists of water, pigments and binders. Thickeners may be used to control the water retention and rheology of the coating colour. Often, different additives are used to get the desired runnability or end product properties. The purpose of pigments is to achieve the desired brightness, gloss, colour and opacity properties of the coated paper [19]. The most common pigments are calcium carbonate and kaolin, but there are a number of other alternatives; a combination of pigments is used in many cases. There are also special pigments used to fine-tune the properties of the coating colour.

The purpose of binders is to bind the pigment particles to each other, and to bind the coating colour into the base paper. Binders also have an effect on the

properties of the wet coating colour, for example the water retention characteristics. The most common binders are different latexes, which are non-soluble in water, and starch, proteins, derivatives of cellulose and different alcohols, which are soluble in water. Often, two or more binder substances are used together to get the desired runnability and end product properties. Some thickeners also have binding properties, as well as the binders having thickener properties.

Typically, the coat weight ranges from 5 to 20 g/m^2. Multiple coating layers may be applied to achieve coat weights that are not possible with one coating. This is very common in the coating of paperboard [90]. Only one side of the paper may be coated, or both, and the coating colours and coating process conditions can be different for the two sides.

The type of base paper affects the properties of the final coated paper. In addition to the normal paper properties (stiffness, tear resistance, etc.), the base paper has also a great effect on the water transport characteristics during the coating process. This affects the roughness, printability and other properties of the final product [19].

There are many types of paper coating methods. Blade coating with jet application was used in the on-line trials discussed in this thesis. Thus, the focus in the following description and discussion is on this specific coating method. The blade coating method used in this work takes place in three phases: first, the wet coating colour is applied to the paper using a jet. Second, the excess coating colour is scraped off with a blade. Third, the excess water is removed by drying the paper with infrared dryers, air flows and cylinder dryers [90]. A schematic picture of a pilot coating machine can be found in Section 4.2.1. There, the trial runs are briefly described and the two different drying strategies used in the trials are presented.

Sizing is a surface treatment technique related to coating. It increases the overall and surface strength of the paper, and is sometimes used to improve the coating characteristics of the paper. In sizing, polymer solutions are applied to the paper in the size press, typically located between two dryer sections of the paper machine [89]. In this work, sizing was used to modify the water absorption properties of the base paper prior to pigment coating.

3.2 Consolidation and critical points

During the drying phase of the paper coating process the coating colour undergoes a transition from a wet suspension to a rigid three-dimensional structure. This transition is referred to as coating colour *consolidation* or *immobilisation*. The chemical and physical changes occurring in the coating colour during consolidation depend on many things; in addition to the properties of the coating colour, the base paper and the drying strategy have an effect, among others [8]. Because the characteristics of the consolidation process have a great effect on the properties of the final product, and especially on the printability [33–35], the understanding of the coating colour consolidation has received quite a lot of interest in the literature. In the following, the most important results achieved in the research are summarised, concentrating especially on the movement of water during coating colour consolidation.

The first remarkable attempt to understand the physical and chemical processes occurring during consolidation of paper coatings was made in 1982 by Watanabe and Lepoutre [20]. They proposed the mechanisms behind the consolidation process and gave a thorough description of the concepts of first and second critical points. Since their milestone paper, the basic understanding of the consolidation process has not changed, but some new aspects have been studied by several authors [21–25].

Watanabe and Lepoutre studied the specular 75 degrees gloss and diffuse reflectance of coating colour layers applied on a glass or plastic film (see Figure 2). Their findings can be summarised as follows: in a typical experiment, after application of the coating, there is a wet coating film on the substrate and the gloss value is high. Water is removed from the coating layer through surface evaporation and absorption into the substrate. The coating reaches the first critical concentration or point (FCC), when menisci start to form on the surface. At this point there is an abrupt drop in the gloss value (see Figure 2) since the film-like surface of the wet coating changes into a rougher surface. The gloss continues to drop until it reaches the gloss level of a dry coating layer. The diffuse reflectance decreases slightly when the coating layer is wet, and continues to drop through the first critical concentration. At the so-called second critical concentration or point (SCC), the reflectance rises sharply (see Figure 2). This is related to air permeating the coating structure. Because air has a lower

refractive index than water (1.0 compared to 1.33), the scattering efficiency of the coating layer increases drastically, resulting in the rise of the diffuse reflectance. The reflectance rise continues until all water in the pores of the coating is replaced by air. Moreover, at the SCC, the gloss has nearly reached its final value, i.e. the second turning point of the gloss curve.

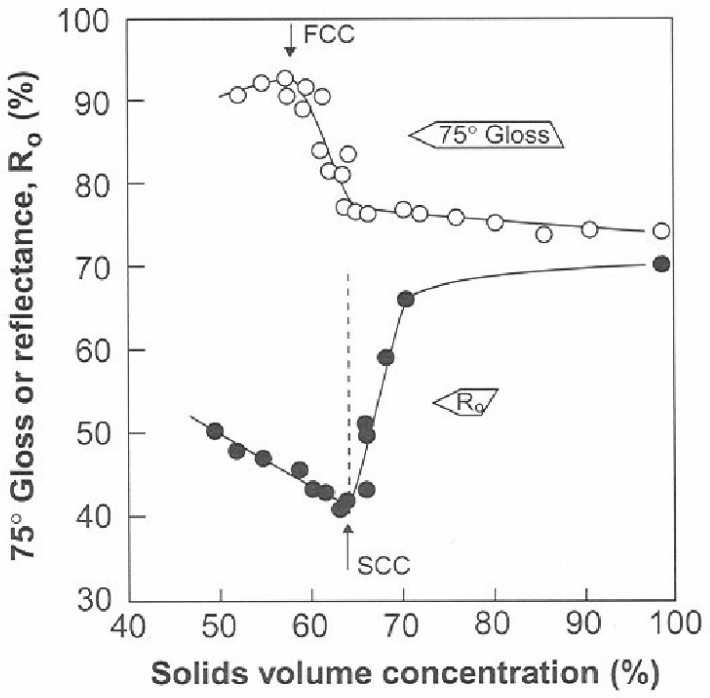

Figure 2. The gloss and diffuse reflectance as a function of the solids volume concentration in the wet coating according to Watanabe and Lepoutre. The positions of the first and second critical concentration are marked in the figure (FCC and SCC).

Watanabe and Lepoutre also showed that when the coating layer is wet and has not reached the FCC, particles (and also water) can move rather easily in the dispersion. This movement is greatly restricted when the coating colour reaches the FCC, at which point a three-dimensional network forms. From this point on, capillary forces cause shrinkage of the network until at the SCC the network is fixed and a rigid three-dimensional structure is left.

The laboratory consolidation studies of Watanabe and Lepoutre were continued in [21, 23] to examine the structural properties of the coating colour and their relationship to the consolidation process. The gloss signal and the light-scattering coefficient as calculated with the Kubelka–Munk theory were used in these studies, along with other analysis methods.

The coating consolidation process suggested by Watanabe and Lepoutre is quite simple from the point of view of measurements. However, Morin et al. [25] showed that the behaviour of specular gloss in the actual coating process of paper is more complex. The most important reasons for this are the deformation and other effects caused to the base paper and the coating layer by the coating blade.

The influence of the blade pressure on the smoothness of the surface of the coated paper is shown in Figure 3. According to Morin et al., the following effects take place in the coated paper at and after the blade:

- The base paper recovers from the pressure caused by the blade. This causes a redistribution of the coating colour on the paper surface.
- Water and some binders migrate into the base paper, thus forming a high-solids filter cake in the base paper – coating interface.
- The water penetrating the base paper causes fibre swelling.

The roughening of the paper surface after the blade makes the specular gloss drop right from the blade, since the rough surface makes the specular reflection spread angularly. Thus the simple picture of the sudden drop in the gloss related to the FCC as described above is not fully valid in on-line conditions. On the other hand, the FCC is not necessarily reached at the same time at different positions on the paper because of the non-uniform coat weight [25]. This also makes the sudden drop in gloss more like a gradual transition. The roughening effect together with the non-uniform coat weight complicates the interpretation of the gloss measurement results.

Theories exist on the formation of specular reflection or gloss from rough surfaces [91]. In addition, techniques to simulate the angular dependence of specular reflection based on surface roughness measurements of coated paper

samples have been proposed [83]. On the other hand, MacGregor et al. have proposed an instrument to measure the spatial gloss variation on paper samples [92]. However, the application of these theories and techniques in the paper coating process to the coating consolidation research has not been reported.

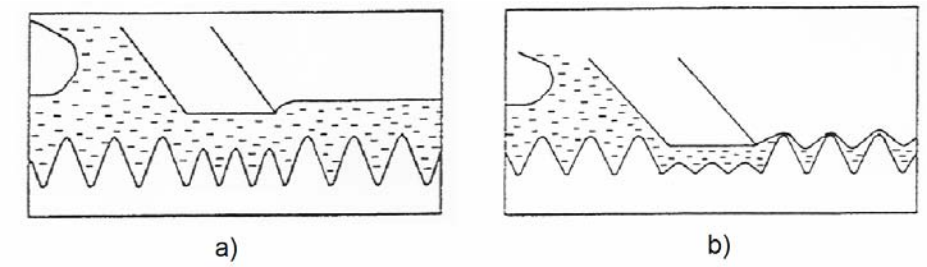

Figure 3. Low (a) versus high (b) blade pressure and their influence on the smoothness of the surface of the coated paper, after [25].

Honeywell International Ltd. has developed a product to control the drying section in a paper coating process based on the measurement of specular and diffuse reflection. The use of this so-called GelView system in coating trials and real process conditions has been reported by several authors [2, 26–28]. However, the measurement system proposed is not capable of measuring moisture depth profiles during the coating process, only the ratio of specular to diffuse reflection. This tells about the phase of the consolidation but not directly about the water transport.

Some papers have been published about the use of optical moisture measurements in coating consolidation research. For example, Huang et al. [22] used the response of a conventional near-infrared moisture sensor to find the critical points. However, they report that the calibration of the moisture sensor to predict the moisture of the coating colour during consolidation was not possible. Instead, they use the response of the sensor to find the critical points. Also, Willenbacher et al. [24] used near-infrared optical methods to study the dewatering of coating colours in the laboratory. However, they do not discuss the on-line applications of such measurements.

3.3 Mass and heat transfer models

One of the most important aspects of paper manufacturing is drying. It is the main source of energy consumption in paper mills and has thus been the subject of extensive research and optimisation efforts. The modelling of the drying process from the point of view of mass and heat transfer has gained quite a lot of attention in the literature [8, 30, 31, 93–99]. These models describe the heat and mass transfer processes occurring during drying of the paper. The most important parameter to estimate is the drying rate. The models employed to predict the drying rate vary from rather simple to very complicated. The basic principles of heat and mass transfer models are briefly reviewed in the following.

The heat transfer in the paper drying process mainly takes place in three forms: conduction, convection and radiative transfer [95]. Conduction is the predominant transfer mechanism in cylinder dryers, although convection also has an important role. On the other hand, convection has the major role in air impingement drying and radiative transfer is prevailing in the infrared drying.

The contact heat transfer between the paper web and a cylinder dryer is usually described by the heat transfer equation [95]

$$q = \alpha_{c-p}(T_c - T_{p0}) \tag{9}$$

where q is the heat flux, α_{c-p} is the contact heat transfer coefficient, T_c is the temperature of the hot cylinder surface, and T_{p0} is the temperature of the web surface. Convective heat transfer occurs in air impingement dryers and also in other drying methods in paper–air interfaces. The convective heat transfer is described by the equation [95]

$$q = \alpha_{a-p}(T_a - T_{p0}) \tag{10}$$

where α_{a-p} is the convective heat transfer coefficient and T_a is the air temperature. Determining the heat transfer coefficients is not an easy task. In most cases, one must resort to experimental correlations to get accurate estimates for α_{a-p} [96, 97].

The radiation heat transfer in impingement dryers may be described by the radiation heat transfer coefficient. It can be calculated from the temperatures and emissivities of paper and the drying equipment using Stefan–Boltzmann's law [95]. Modelling the radiation heat transfer in infrared dryers requires knowledge of the spectral properties of the web, spectral properties of different components in the radiator and geometric configuration factors [85, 95].

In addition to the heat transfer, mass transfer occurs in the drying process. The most important mass transfer process is that of water vapour escaping from the paper. This phenomenon is often described by the mass transfer equation [98]:

$$\dot{m} = \beta_{a-p}(P_{p0} - P_a) \tag{11}$$

where $\dot{m}$ is the water evaporation rate, β_{a-p} is the mass transfer coefficient, P_{p0} is the partial vapour pressure on the paper surface, and P_a is the partial vapour pressure of the surrounding air. The mass transfer coefficient has to be determined experimentally, or by experimental correlations.

By combining the heat and mass transfer equations stated above with the heat and mass balance in the drying process, one can create a mathematical model of the drying process [98]. The heat and mass balance equations typically relate the change in paper temperature to the heat and mass fluxes, and the change in moisture content of the paper to mass fluxes. In single layer models, the paper is treated as a single layer, and the mass and heat transfer inside the paper are neglected [98]. There are also more sophisticated models, which include the transfer processes inside the web [99].

The drying of coated paper can be treated with the models described above. However, modelling the coating application is needed to understand the coating process. The so-called KCL model [100] is able to describe the coating process before drying, i.e. the effect of the jet application and the blade. The model takes into account, among other things, the pressure against the paper web in the jet application and under the blade, the capillary water transport mechanisms and paper and roll compression. The model predicts the dewatering of the coating colour layer, and wetting of the base paper.

Rajala developed the so-called VTT model for paper drying simulation in 1995 [94], based on the model by Lampinen [99]. The VTT model was very recently modified to be able to predict the critical concentrations [8]. The modified model expresses the heat transfer to the coated web from the air foils and from the infrared dryers. The model also takes into account the evaporation of water from the surfaces of the paper and internal heat and mass transfer processes inside the coating layer and base paper and between them. These processes are described by partial differential equations. The boundary conditions express heat and mass transfer between the dryers, the surrounding atmosphere and the paper web. In addition to predicting the critical concentrations, the model gives the evaporation rates, and temperature and moisture gradients inside the paper.

In the work of Timofeev et al. [8] the KCL model was used to calculate the state of the coated paper before drying, and the VTT model to simulate the drying process. The results of the simulations were compared to the experimental results obtained with the moisture depth profiling system presented in this thesis. Specifically, comparisons were made between the simulated and measured locations of the critical points. In this thesis, measurement results obtained with the moisture depth profiling system are not directly compared to results from the mass and heat transfer models. However, these models offer a valuable guide in understanding the measurement results in this thesis. Whenever appropriate, comments about the correspondence of the measurement results and theoretical models will be made.

4. The depth-profiling system and method

One of the main goals of this thesis is the development of a fibre-optic measurement system that is capable of measuring moisture depth profiles in paper at multiple positions. This chapter describes the measurement system in detail, starting from the instruments used and ending with the measurement methods and data processing. The system was first tested in a laboratory coater, and then installed in a pilot-scale coating machine. The measurement methods used in both cases are presented, as well as the methods to calculate the specular reflection, diffuse reflection intensity and moisture results.

4.1 Measuring equipment

The multimeasurement system developed will be discussed in detail in the following sections. In addition to the system, the method for performing reliable measurements in an on-line application is also described. Although the system was developed with on-line multipoint measurements in mind, it can be used in laboratory single-point measurements as well. The description below concentrates on the on-line situation, but the main principles also apply to the use of the measurement system in the laboratory. The differences between the on-line and the laboratory use are discussed in Section 4.3.1. The testing of the measurement system and principle has been done in the laboratory, but there are a number of laboratory measurements that are scientifically interesting *per se*.

4.1.1 Configuration

To meet the need for multipoint and multigeometry measurement that could be installed onto a paper coating machine, a fibre-optic measurement system was designed, as shown schematically in Figure 4. It consists of a fibre-optic light source with a chopper and a controller, fibre-optic measurement probes, a spectral camera, and a computer for data acquisition and processing. The measurement positions are shown by the circles. Specular reflection, diffuse reflection from both sides of the paper, and different transmission signals are measured in measurement positions 1–7. The reference probe is used to track the phase of the signal from the other probes, and it can also be used to monitor the

stability of the light source. The light source provides the illumination to the measurement positions and to the reference probe. The spectral camera collects the light that has interacted with the paper.

The light source and the probes were designed and fabricated at VTT in Oulu, Finland, by the author and several optical and mechanical design engineers. The fibre-optic spectral camera was an Aisa Hawk produced by Spectral Imaging Ltd., Oulu, Finland.

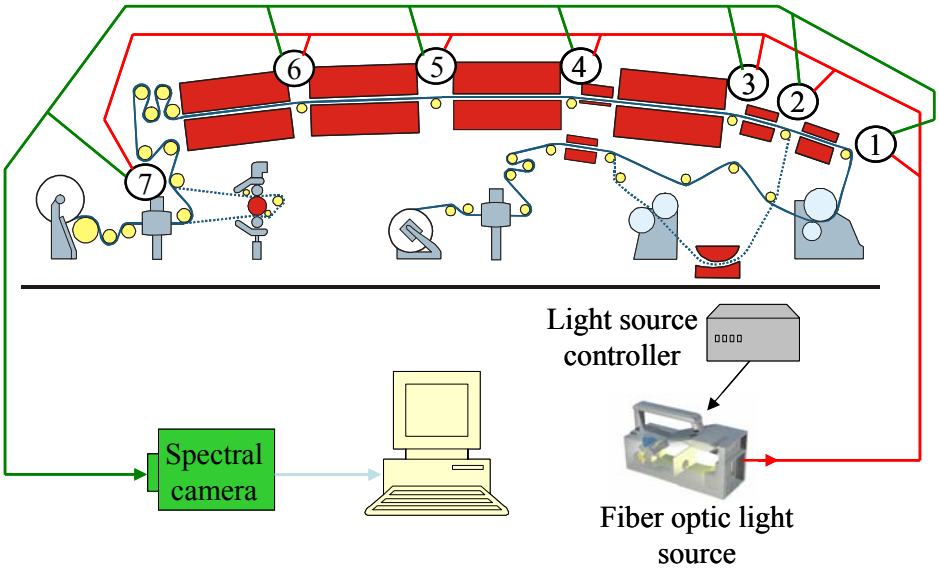

Figure 4. Block diagram of the measurement system. The measurement positions are shown by the circles. In measurement positions 1–7 specular reflection, diffuse reflection intensity and 5 different moisture values are measured. The reference probe is for tracking the phase of the signal and for monitoring the lamp.

4.1.2 Probes

The environmental conditions in a paper coating machine are rather harsh. The temperature can exceed 200 degrees Celsius in many places, and the humidity is also high. Moreover, during possible web breaks the paper and the wet coating can contaminate or even damage the measuring equipment. Metallic fibre-optic probes are a natural choice in such an environment.

The measuring equipment at each measurement position consists of a top unit and a bottom unit (see Figure 5 and Figure 6). The top unit has a top reflection probe and a specular reflection probe, whereas the bottom unit only has a bottom reflection probe. The top and bottom reflection probes are mechanically and optically similar. They include an illumination mirror, which images the end of the illumination fibre onto the surface of the paper, and a collection mirror, which images the paper surface to the end of the collection fibre. The specular reflection probe is a lens package that collects the light from the paper surface to the end of the collection fibre. The probes and the mirrors are fabricated using modern CNC milling machines and packaged carefully to form a robust probe. The mirrors look at the paper through a protective sealed window. The distance from the top (or bottom) reflection probe to the measurement spot is about 105 mm and the corresponding distance for the specular reflection probe is about 95 mm.

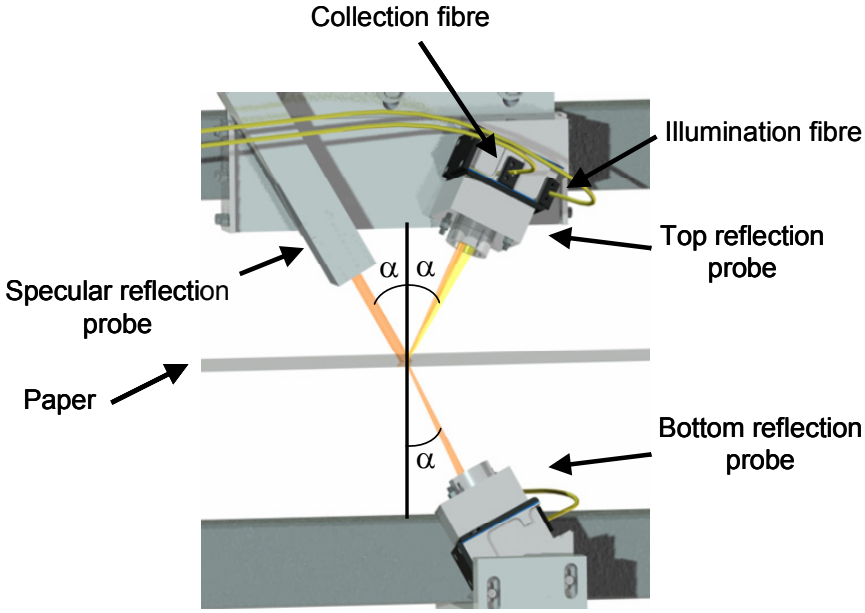

Figure 5. Drawing of the probes in a measurement position. The top reflection and specular reflection probes form the top unit, and the bottom reflection probe forms the bottom unit. The angle to paper surface normal $\alpha = 30°$ is also shown. The yellow colour indicates the illumination rays and the orange colour the collection rays in a particular phase of the illumination sequence.

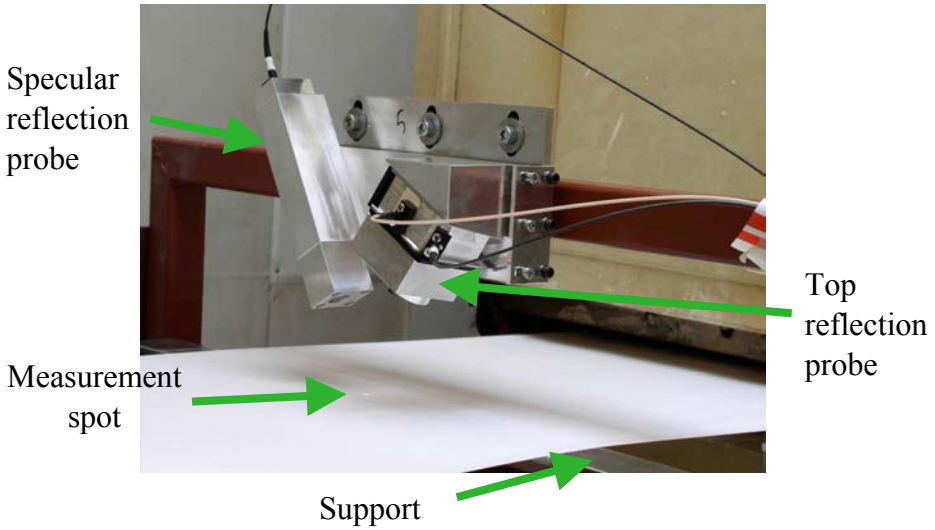

Figure 6. The top side fibre-optic probes. Distance from the top reflection probe to the measurement spot is about 105 mm and the corresponding distance for the specular reflection probe is about 95 mm. The 4 mm wide and 6 mm long measurement spot is faintly visible on the paper. There is a metallic support below the paper, as can be seen at the very bottom of the image.

The top reflection probe collects the diffusely reflected radiation from the paper and the specular reflection probe collects the specular reflection from the paper. The bottom reflection probe collects the diffusely reflected light from the bottom side of the paper. All probes are aligned so that they see the same spot on the paper and the specular reflection probe is in the line of sight of the bottom reflection probe. This particular geometrical arrangement allows the simultaneous measurement of reflection and transmission signals, which is crucial in moisture depth profiling.

The measurement positions were chosen carefully. There are more positions at the beginning of the drying section since most of the changes take place there. Almost all empty sections between the dryers are used as measurement positions. There are no measurement probes above the turning rolls, although they would provide a very stable web. There are two reasons for this: first, transmission measurements would be impossible, and second, the infrared radiation reflects from the roll, which would make the comparison to positions without a roll impossible.

There are two main features in the design of the reflection probe: first, it maximises the collected optical power from the measurement spot, and second, it minimises the distance dependence of the probe. The distance insensitivity is achieved by making the illumination spot larger than the collection spot and by optimising the shape of the spots. The optimisation is done by custom surface design in the mirrors, going beyond the conventional conic sections. As a result, ±5 mm distance insensitivity is obtained for the reflection probe.

The specular reflection probe has similar requirements to the reflection probe for the distance insensitivity. In addition, the specular reflection probe also has to be insensitive to angular variations since the specular reflection is very directional. Fluttering and creasing of the paper changes the direction of the specular reflection. Thus the specular reflection probe must tolerate slight changes in the direction of the specularly reflected light. This means that the probe's angular collection efficiency has to be uniform. These challenges have been addressed in the design of the specular reflection probe. The specular reflection probe is a lens package consisting of three lenses and an aperture. The lenses form a telecentric optic, which forms a nearly collimated collection beam, and simultaneously ensures that the acceptance angle is constant over the whole collection spot.

The optical design used to collect the specularly reflected light in the specular reflection probe is schematically shown in Figure 7. The combination of the first, second and third lens images the paper surface onto the end of the optical fibre. An aperture is placed at the focus of the first lens, which coincides with the focus of the second–third lens combination. The optical design is of the telecentric type. The advantages of this optic are that its magnification does not depend on the probe–paper distance, and the acceptance angle on the surface of the paper is constant over the whole collection spot. These properties are essential in achieving the distance insensitivity for two reasons: first, as the probe–paper distance changes, the position of the illumination spot inside the collection spot changes. Therefore, the acceptance angle of the specular reflection probe must not change. Second, the collection efficiency must not change with distance, which means the magnification of the specular reflection probe has to be distance insensitive.

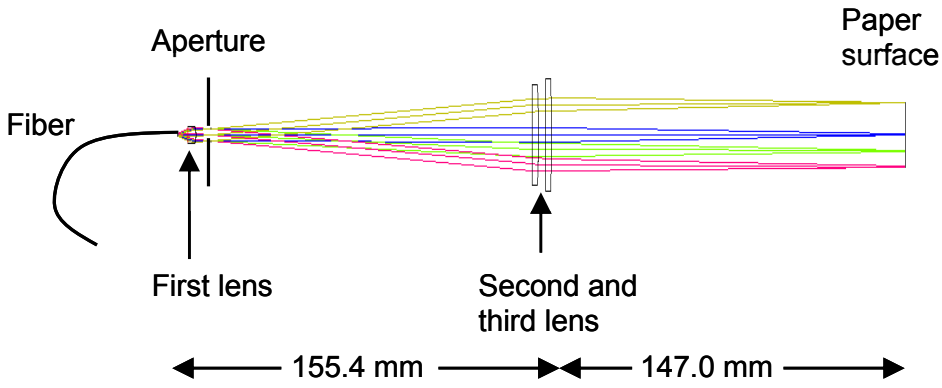

Figure 7. The optical design of the specular reflection probe.

The top reflection probe and the specular reflection probe subtend a 30-degree angle to the paper surface normal. This also defines the angle of the specular reflection measurement. The most widely used specular gloss measurement standard, the so-called Hunter gloss, uses a 75-degree angle to the surface normal of the paper and uses the visible spectral range [101]. However, this standard was developed to measure gloss mainly from the final product. In this work the purpose is to obtain information on the state of the wet coating. The main reason for selecting 30 degrees for the specular reflection angle is that larger angles would make the measurement unit larger and make it difficult to achieve the angular deviation and distance insensitivity. Selecting 30 degrees for the angle leads to a lower sensitivity to specular reflection than using 75 degrees. In fact, this is an advantage, since the 30 degrees specular reflection of a wet coated paper may be even 20 times higher than that of a dry coated paper. Thus, a 75 degrees specular reflection angle could have lead to difficulties in the dynamic range of the measurement.

In this thesis, the term "gloss" is used to refer to measurements made according to a certain gloss standard, for example [101]. Since the specular reflection measurement described above does not fulfil the requirements of any gloss standard, the measurement will be referred to as "specular reflection". In particular, this choice is made because the wavelength range of the spectral camera is in the NIR region, whereas the gloss standards use a visible wavelength. However, the behaviour of the specular reflection measurement of this thesis was tested to be proportional to the results obtained with a standard gloss meter.

The spot sizes of the probes are different. The illumination spot of the top and bottom reflection probes is 4 mm wide and 6 mm long. The top and bottom reflection collection spot is 1.5 mm wide and 3 mm long. The spot size difference is needed to obtain the ±5 mm distance insensitivity. The effective spot size of top and bottom reflection measurements is the smaller of the two mentioned above, namely 1.5 mm times 3 mm. The specular reflection collection spot is circular and measures 18 mm in diameter. Because the diffuse reflection probe also provides illumination for the gloss probe, the effective spot size for gloss measurement is 4 mm times 6 mm. The magnifications of the optical systems in the top and bottom reflection probes are about 7 times for the illumination and 14 times for the collection. The magnification in the gloss probe is about 30 times.

The moving paper web flutters remarkably at some positions. A metallic support is used below the paper to stabilise the web. It also makes the installation of the probes to the correct measurement distance easier. In the trial runs the supports were not observed to cause any problems. Another way to stabilise the web would be an air-clamp [2]. However, this would make the design of the measurement units far more complex since one of the primary targets is to measure from both sides of the paper and through the paper. With the metallic support, this was easily achieved by making a hole in the support.

4.1.3 Measurement principle

To take full advantage of the measurement geometry, the fibre-optic light source was designed to perform so-called double-chopping. The light source has 24 output fibres, which are chopped with a rotating chopper in the following fashion:

1. lights on in half of the fibres, lights off in the other fibres (top phase)
2. lights on in the other half of the fibres, off elsewhere (bottom phase)
3. lights off in all the fibres (dark phase).

This illumination sequence is illustrated in Figure 8. Note that in all phases, all the three probes are collecting; only the place of the illumination is changed. This “temporal multiplexing” is the only practical way of measuring the reflection from both sides and transmission through the same spot on a moving

paper simultaneously. Strictly speaking, the measurements are not exactly simultaneous. The chopping frequency determines how simultaneous they are; this frequency depends upon the speed of the chopper blade inside the light source and could be up to few thousand hertz. In the measurement system for this thesis, however, the spectral camera can take 100 frames per second. This limits the chopping frequency to 10–30 hertz, depending on the details of demodulation of the chopped signal. Fortunately, the paper coating process is very stationary; thus the average quantities are those of interest.

The inclusion of the dark phase is absolutely crucial. In principle, the dark signal could be measured separately by blocking the illumination for some time, but this does not work very well on the coating machine. The main reason is the interference from the infrared dryers, which are essentially incandescent lamps. Measurement position 2 in particular, which is located between two infrared dryers, suffers from very strong interference, even though the light from the dryers cannot reach the probes directly. The increase in the visible light level on the measurement spot when the infrared dryers were switched on could be easily seen with the naked eye. In the infrared spectral range, the interference effect should be even more pronounced. The inclusion of the dark phase in the chopping sequence rejects this interference very effectively.

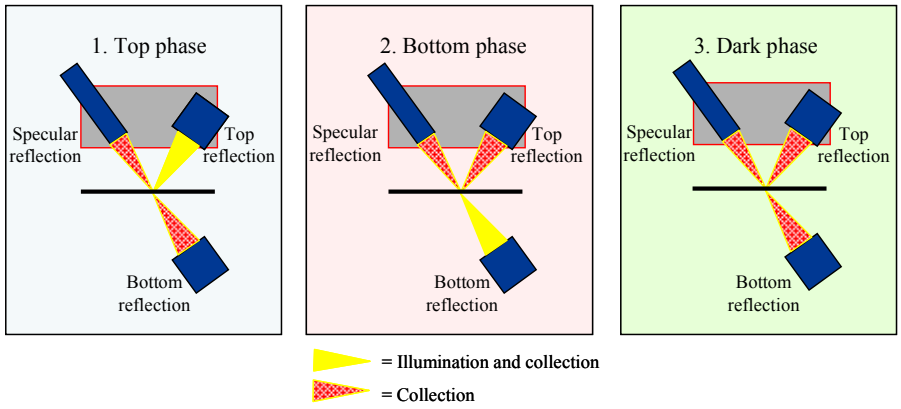

Figure 8. The illumination sequence. There are three phases: top, bottom and dark, as indicated in the figure. When a probe is illuminating, it is actually also collecting radiation, but when it is in the "collection" state, it only collects radiation.

Table 1. Types of measurement at different illumination phases. The phases and probes are depicted in Figure 8.

Probe	***Top phase***	***Bottom phase***	***Dark phase***
Top reflection probe	Top reflection signal	Bottom-to-top transmission signal	Dark current
Specular reflection probe	Specular reflection signal	Bottom-to-top transmission signal (collimated geometry)	Dark current
Bottom reflection probe	Top-to-bottom transmission signal	Bottom reflection signal	Dark current

The illumination sequence and the measurement geometry allow measuring with six different geometries almost simultaneously, as summarised in Figure 8 and Table 1. All of the seven measurement positions have these six geometries. The resulting 42 measurement signals are detected with the spectral camera, which disperses them spectrally, yielding near-infrared spectra in the wavelength region 968–2436 nm. Many properties of the sample can be calculated from the spectra, including moisture, specular reflection and diffuse reflection intensities.

The measurement system was first tested in the laboratory and then installed on a laboratory coater for laboratory-scale coating experiments. Only one full-equipped measurement position was installed and used in these experiments. After these tests the full measurement system was installed on the KCL pilot coating machine, and measurements were performed during trial runs.

4.1.4 Light source

The light source used is a double-chopping fibre-optic light source with 24 output fibres. Double-chopping means there are two light paths, which are chopped by the same chopper but in a different position. These two light paths are guided to two separate fibre bundles. This allows the following illumination schedule:

1. lights on in bundle 1, off in bundle 2
2. lights on in bundle 2, off in bundle 1
3. lights off in both bundles.

This makes it possible to measure reflection from both sides of the paper, but from the same spot. Strictly speaking, the measurements are from the same spot only if the paper is non-moving. A moving paper web results in top and bottom reflection measurements that are from different positions in the machine direction but from the same positions in the cross direction. Dark current is also collected in the chopping sequence, which rejects the interference from ambient light, especially from the infrared dryers. Reference measurements in the measurement positions are used to compensate for changes in the lamp intensity due to drifting and ageing.

In the light source the light from a halogen bulb is first collected by two collecting mirrors on both sides of the bulb (see Figure 9). These collecting mirrors form images of the lamp filament onto two imaging mirrors. The imaging mirrors image the collecting mirrors to the ends of two fibre-optic bundles. The geometry is of the Köhler illumination type [102]. The Köhler illumination is used in order to produce a uniform illumination power on the ends of the fibre-optic bundles. There is no sign of lamp filament image in the position of the bundle ends and the irradiance level in all 24 fibres is on the same level.

The chopper blade is located between the imaging mirror and the fibre-optic bundles. The blade only has one hole extending about one-third of the circumference (the blue disc in Figure 9). The geometry of the chopper blade and the fibre-optic bundles is arranged to produce the illumination sequence described above.

The controller box includes the current source, and some electronics to stabilise the lamp and control the chopper. The controller keeps the resistance of the lamp constant, which, in principle, also keeps the temperature of the filament constant. The chopper has a reading frame, whose signal is used by the controller to keep the chopping frequency at the desired value.

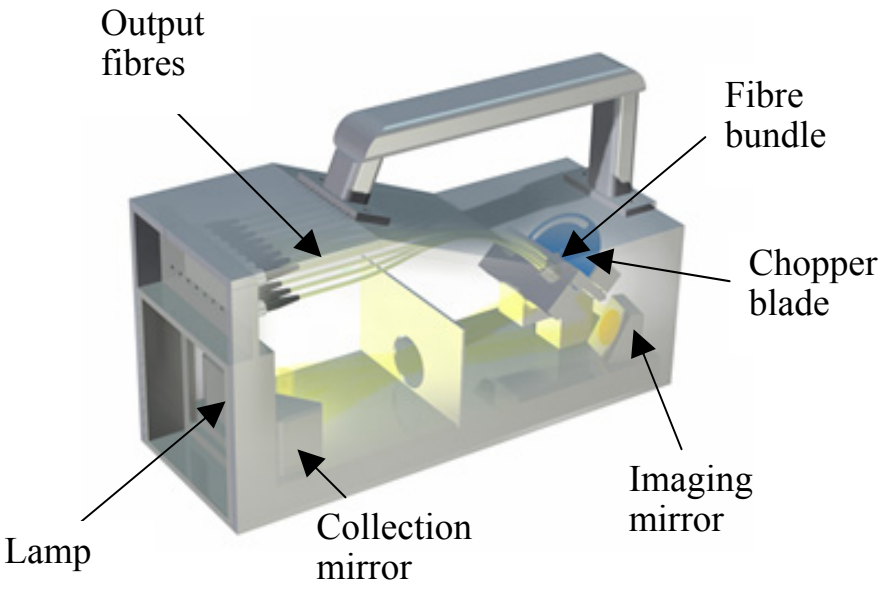

Figure 9. The fibre-optic light source.

4.1.5 Fibres

Normal infrared-grade silica-silica fibres are used for illumination and collection. The illumination fibres have a core diameter of 600 µm and the top and bottom reflection collecting fibres have a core diameter of 105 µm. Instead, the specular reflection collecting fibre has a core diameter of 600 µm. The fibres have a fibreglass jacket. The five fibres of each measurement position are bundled together in a plastic cable to make the handling easier.

4.1.6 Spectral camera

The particular type of spectral camera used in the measurement system is based on a mercury-cadmium-telluride infrared camera (hereafter called the MCT camera). The spectral camera has 253 rows and 320 columns and its spectral range is 968–2436 nm. It is capable of taking 100 frames per second and has a 14-bit analogue-to-digital converter. The camera is cooled with a 4-stage Peltier cooler, which keeps its temperature as low as −80 degrees Celsius.

The MCT array and matrix detectors have shown excellent performance in the near-infrared region as compared to the more conventional extended InGaAs detectors [53]. This fact along with the powerful 4-stage cooling makes the MCT camera a very sensitive instrument. The high sensitivity makes it possible to use fibre-optic illumination in the probes, which is hardly feasible when using extended InGaAs arrays as detectors. The spectral camera has 110 input fibres with a core diameter of 62.5 μm, which means it can measure 110 infrared spectra from different positions at the same time.

The spectral camera is operated by software delivered by the vendor, Specim Ltd. The software features grabbing of frames but not separation of the signals from the input fibres. All data processing further to frame grabbing is performed by custom-made Matlab programs.

4.2 On-line measurements

The main application of the developed measurement system is the paper coating process. Therefore, the majority of experimental results were obtained during trial runs at the KCL pilot plant. In this section the details of the trial runs are presented, followed by a description of the measurement procedure used in the trial runs and the data processing methods.

4.2.1 Trial runs

It is a common practice in the paper industry to test new coating formulations, different drying conditions and different base papers on pilot-scale machines. The main reason is the cost benefit: the pilot machines are often built with a similar construction as the production machines but the width of the web is very much smaller. This leads to savings in energy consumption, raw materials needed for the tests and machine maintenance costs. In addition, the purpose of production machines is to produce as much paper as possible, which means the time and possibilities for testing different scenarios are limited. On the contrary, the pilot machines can be built so as to maximise flexibility for different tests.

In this thesis the measuring equipment was installed on the pilot coating machine at KCL. An extensive program of trial runs was conducted to test different aspects of the coating process. Wood-containing base paper (51 g/m^2) was coated with a jet-applicator blade coating unit. Brazilian kaolin (Capim SP), 50 pph (parts per hundred), and ground calcium carbonate (HC-90), 50 pph, were used as pigments, and styrene-butadiene latex (DL 966), 10 pph, as a binder. There were four variables in the trial runs:

1. type of base paper (uncoated, sized, impermeable)
2. two drying strategies (high-low-low and low-low-high)
3. different coating colours (the thickener was varied)
4. different coat weights (7.0–13.0 g/m^2 target coat weights).

The running speed in the trials was 1500 m/min. The target final moisture level was 5%, which was measured with the permanently installed moisture gauge before the rewinder.

A particular combination of the variables listed above is called a *trial point*. Preparation for one trial point requires a lot of work, and is only briefly described. The coating colour for a particular trial point was made and the base paper was installed on the coating machine before starting the trial point. When the running of the base paper through the coating machine was started, the infrared dryers and air foils were preheated. The coating process was then started and the angle and pressure of the blade, the temperatures and air flows in the dryers, as well as other parameters, were set so that the conditions for a particular trial point were achieved. Then the actual trial point could be started. Typically, several tens of trial points could be run during one day.

Theoretically, the base paper type should affect the water transport from the coating layer to the base paper. Three base paper types were used in the coating trials. The “uncoated” base paper absorbed water rapidly. The “sized” base paper was surface sized with starch and hydrophobic agent, and was expected to absorb water more slowly. The “impermeable” base paper was coated with a high amount of latex, forming a non-porous surface, which should make water absorption very slow. The coating colours with different thickeners had different water retention characteristics. Different base papers, coating colours, coat

weights and drying strategies were expected to have a clear effect on the coating immobilisation during the coating process.

Figure 10 and Figure 11 show how the dryers of the coating machine were used in the two drying strategies. The strategies are almost reflections of each other: in the high-low-low strategy the infrared dryers and the first air foil were functioning, and the other air foils were cold, except the last one, which was used to adjust the final moisture level of the coated paper. In the low-low-high strategy the infrared dryers and the first air foil were cold, and the other air foils were functioning.

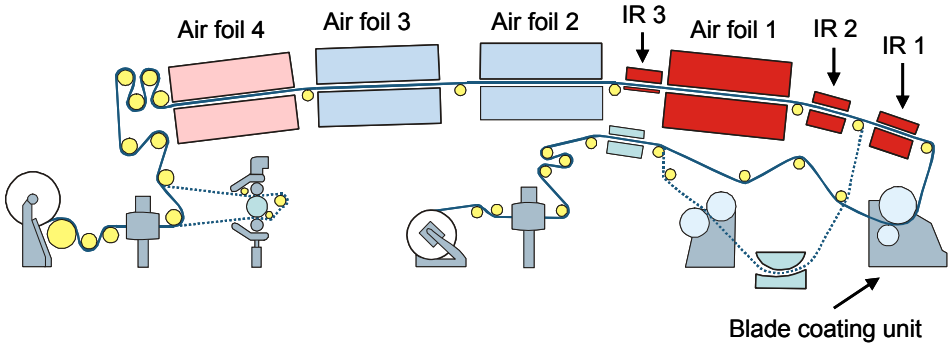

Figure 10. High-low-low (HLL) drying strategy. The infrared dryers and the first air foil are functioning, and the second and third air foils are cold. To adjust the final moisture level, the fourth air foil is run at relatively low power.

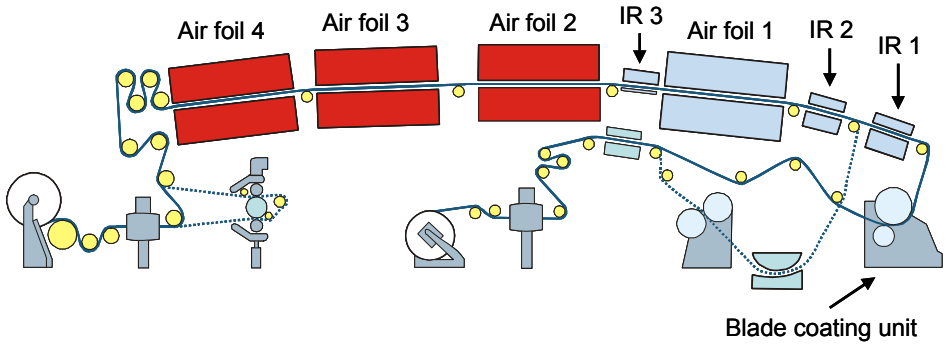

Figure 11. The low-low-high (LLH) drying strategy. The infrared dryers and the first air foil are cold, and the other air foils are functioning at high power.

4.2.2 Measurement procedure

The measurement procedures used for the actual measurements, reference measurements and standardisation between the probes are described in this section. The many measurement geometries and measurement positions posed some challenges, which had to be solved to get reliable measurement results.

Trial point measurements

The measurements at each trial point were very straightforward: before the start of the coating process, the plain, moving base paper was measured (1000 frames), and after the start of a trial point, 3000–5000 frames were collected. Care was taken to ensure the trial point measurement was not started before the trial point was started, and was finished before the end of the trial point. Only the measured frames were saved in this phase. Data processing was performed afterwards.

Reference measurements

Reference measurements have to be performed to calculate near-infrared absorption spectra from the measured intensity spectra. Optical teflon (Gigahertz-Optik GmbH, Op.DI.MA) was used for this purpose in this work. The material was machined so thinly that it allowed simultaneous measurement of diffuse reflection and transmission. The reference sheet was fixed to an aluminium plate. The procedure for reference measurements was the following:

1. The transmission channels were blocked to prevent the saturation of the specular reflection channels, which could leak to all channels.
2. The reference plate was placed on one of the measurement positions.
3. 1000 frames were taken three times, so that the reference plate was shifted a little bit between the measurements.
4. Steps 2 and 3 were repeated for all measurement positions.

After combining the spectra from the reference measurements, references for all reflection, transmission and specular reflection channels in all measurement

positions were obtained. The three spectra from every measurement position allowed cross-checking the signal to detect possible errors in the reference measurement.

Probe-to-probe standardization

In a normal optical measurement application there is only one probe, and the reference measurement standardises the probe completely, at least in principle. In this work there are seven similarly equipped measurement positions. Although the probes were machined with modern precision mechanical facilities, there was no guarantee that the probes would actually behave in exactly the same way in the measurements. Therefore, some methods for probe-to-probe standardisation were needed.

The reference signal measured with the reference plate as described in the preceding section served as a probe-to-probe standardisation method. This was sufficient for the calculation of the height of absorbance bands since intensity variations cancel out in the calculations.

However, a very good probe-to-probe standardization method was needed for the specular reflection and diffuse reflection measurements since these are absolute intensity measurements. The reference plate was not suitable because of the spatial inhomogeneity of the material. The signal from the reference plate varied a few per cent from point to point on the surface, and there was also a small angle dependence of the specular reflection signal. This was too much since the intensity levels of the diffuse reflection channels only changed a few per cent in some trial points.

Before starting a trial point the base paper was run at low velocity through the coating machine without applying any coating. Measurements were taken at this time and these measurements were used as a reference and standardisation method for specular reflection and diffuse reflection intensity. The only change that occurred in the base paper in this situation is that it dried since there was some heat remaining in the air foils, even though they were not functioning. Such drying only changed the specular reflection and scattering properties of the paper very slightly. This made the base paper a perfect reference. Unfortunately,

because of the drying, the base paper measurements could not be used as a reference for the moisture calculations.

As a further standardisation and test sample, a glossy paper was run through the coating machine several times during the pilot trials. The glossy paper better resembled the situation during trial points, where the coating layer was wet and glossy. See Section 4.2.3 for further details on how these measurements were used.

4.2.3 Data processing

The spectral camera measures 110 near-infrared spectra in the wavelength region 968–2436 nm; 23 of these channels were used in the pilot trials. This data had to be processed carefully in order to obtain interesting results describing the coating process. The processing was performed afterwards with Matlab programs specifically written for the purpose.

The processing can be divided into four parts:

1. Extraction of the 23 channels from the frames taken by the spectral camera.
2. Detection of the phase of the frames and calculation of the top-phase and bottom-phase spectra.
3. Calculation of the absorbance and corrected intensity spectra.
4. Calculation of final quantities of interest.

In this thesis the final quantities of interest include specular reflection, diffuse reflection intensity (called *scattering* for short) and moisture. Scattering and moisture values could be calculated from top and bottom diffuse reflection spectra, and from transmission spectra (see Figure 8 and Table 1 for a description of the geometries). Specular reflection could only be calculated from the signal of the specular reflection probe. Typically, specular reflection, top reflection intensity, top and bottom reflection moisture, and top-to-bottom transmission moisture were considered in the analysis of the measurement results. Other quantities can also be calculated from the spectra, such as water

vapour band height and the shift of water absorption band as a function of temperature (see Chapter 7). As an example of the other quantities, the calculation of water vapour band height, in addition to the specular reflection, scattering and moisture calculations, is presented in the following discussion.

Extraction of the channels

Extracting the channels from the images was straightforward since every channel occupies a single column in the image (see Figure 12). The program just read the sequence of images and mapped the appropriate columns to a matrix, which was then saved.

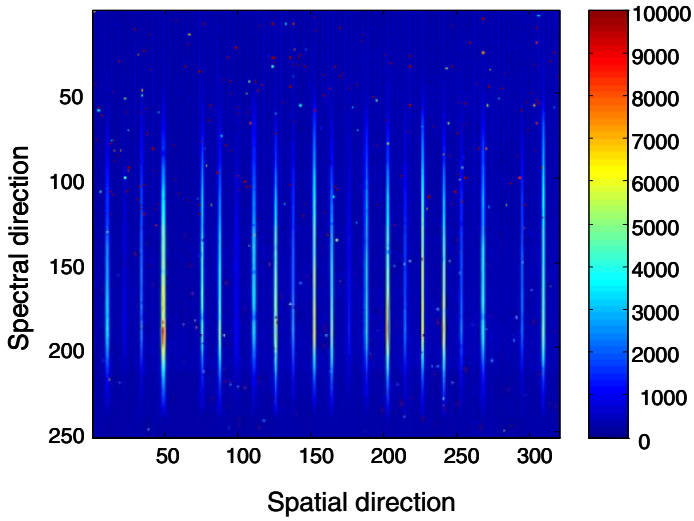

Figure 12. A measurement image collected by the spectral camera. The stripes are the spectra from the measurement channels.

Detection of the phase

As illustrated in Figure 8 and Table 1, there were three illumination phases: top phase, bottom phase and dark phase. Figure 13 presents the signal from the top reflection probe in the first measurement position at the 1859 nm wavelength. The illumination phases show up in the periodically changing intensity level. The phases are marked in the figure. Detecting the phases was done by a Matlab program. After detecting the phase, the program proceeds by subtracting the

nearest dark measurement from the top and bottom illumination phase measurements. All this is performed for all 253 wavelengths and for all 22 channels.

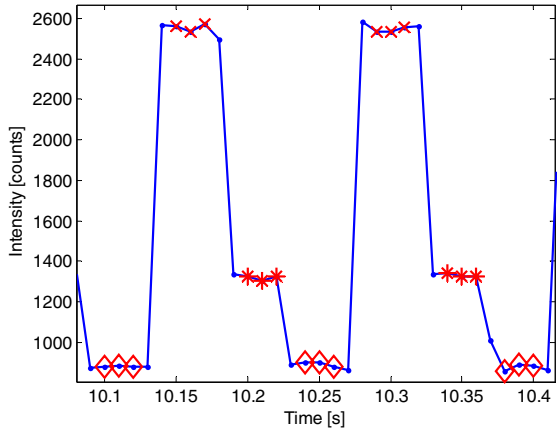

Figure 13. Measurement signal (solid line with dots) at the 1859 nm wavelength and fibre channel 1. The x-marks show the detected top illumination phase, the stars the bottom illumination phase, and the diamonds the dark phase. The detection of the phases was done by the Matlab program.

The result is 43 raw intensity spectra in the following fashion:

- 6 spectra from each of the measurement positions 1–7:
  - top illumination phase: top reflection and top-to-bottom transmission spectra, specular reflection spectrum
  - bottom illumination phase: bottom reflection and bottom-to-top transmission spectra, collimated transmission spectrum (from the specular reflection probe)
- 1 spectrum from the reference channel.

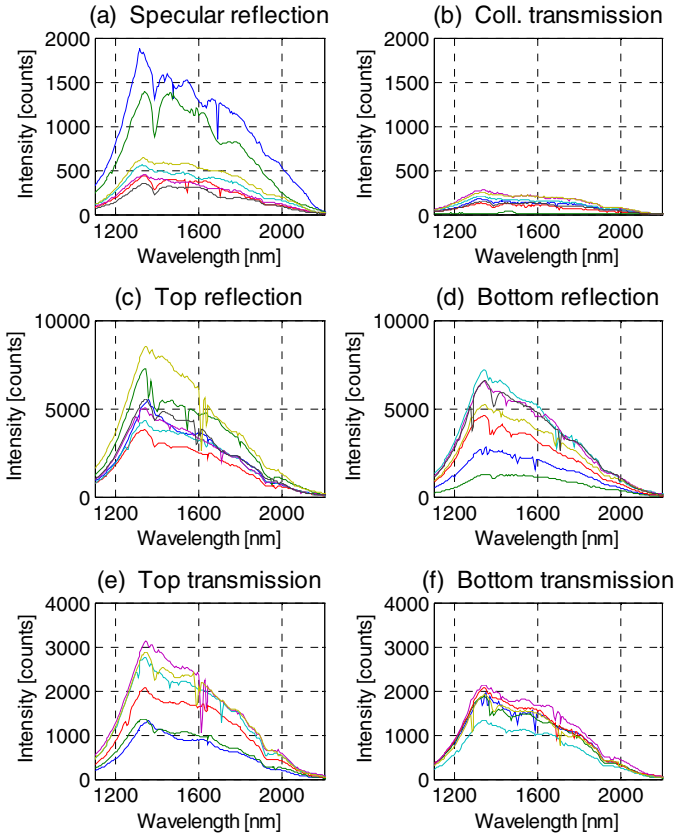

Figure 14. Specular reflection (a), collimated transmission (b), top reflection (c), bottom reflection (d), top transmission (e), and bottom transmission (f) raw intensity spectra measured during a typical trial point. The different colours correspond to the seven measurement positions.

Figure 14 shows the raw intensity spectra from measurement positions 1–7. The signal is much weaker in the transmission channels (Figure 14(b), (e) and (f)) compared to the reflection channels (Figure 14(c) and (d)). This is typical with paper samples having a basis weight greater than about 30–40 g/m^2. The specular reflection signal, Figure 14(a), is also rather weak, but one has to remember that the dynamic range of the specular reflection signal is large. With a very glossy paper the signal maximum can be at about 10,000 counts. The signals from different measurement positions, but with the same geometry, also differ from each other. There are many factors behind this behaviour, including

installation and adjustment differences, differences between illumination fibres, and so on. At longer than 2000 nm wavelengths the low transmission of the optical fibres makes the signal rather weak. This causes a poor signal-to-noise ratio in this region, as will be discussed later.

There are local variations in the refractive index, scattering and absorption coefficients and thickness in the coating layer and the base paper. These variations only have a minimal effect in the spectra in Figure 14, since the spectra are a result of averaging about 250 raw spectra.

Absorbance and corrected intensity spectra

In order to calculate quantities of interest from the spectra, they had to be normalised to a reference. The measurements made with the reference plate were used as a reference for the concentration calculations (moisture and water vapour concentration). The absorbance spectra were calculated in the normal way: the raw intensity spectra were divided by the references, and then the 10-base logarithm was taken and the sign of the result was changed (see Equation (1)).

For specular reflection and scattering, the reference plate measurements were not suitable for use as a reference. Instead, the ratio of the raw intensity spectra to the base paper spectra was calculated. The specular reflection and scattering signals reported in this thesis are always normalized in this way.

The resulting absorbance spectra are shown in Figure 15, and Figure 19 shows the typical spectra from specular reflection and scattering measurements. In the absorbance spectra the water absorption band centred at about 1940 nm is clearly seen, as well as the cellulose band at 2100 nm. The overlapped water and cellulose bands around 1500 nm are the other visible features in the spectra. There are also water vapour absorption bands at 1340–1400 nm, and at 1800–1900 nm, although only faintly visible. See Figure 16 and Figure 17 to see these bands more clearly.

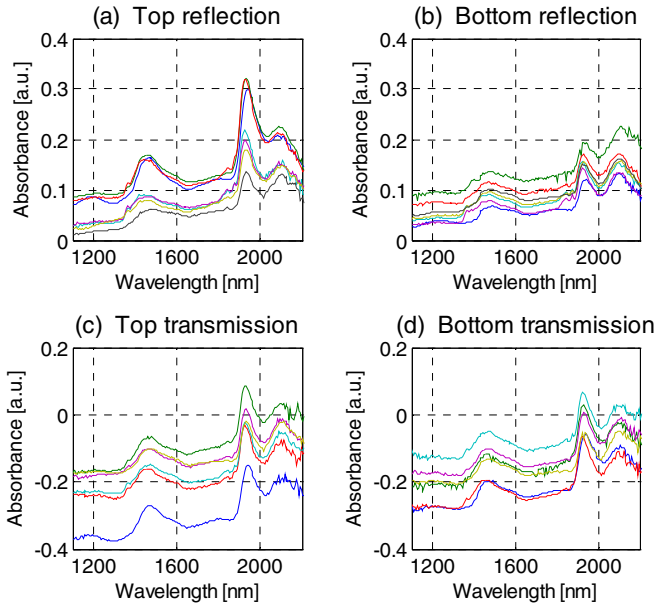

Figure 15. Top reflection (a), bottom reflection (b), top transmission (c), and bottom transmission (d) absorbance spectra collected during a typical trial point. The different colours correspond to the seven measurement positions.

Final quantities of interest

The final quantities of interest can be divided into two categories: concentration measurements (moisture and water vapour) and absolute measurements (specular reflection and scattering). Their reference methods were different, as discussed above. Another difference is that baseline correction had to be employed in calculating the concentrations. Baseline variation is a common problem in NIRS measurements. There are many reasons for baseline variation, but the most important are variation in the measurement distance, dirt build-up in the measurement probes, and changes in the scattering and absorption properties of the sample. In this work, dirt (mainly dust) was removed using compressed air and the paper web was stabilised in the measurement positions. However, baseline correction was still needed for the measured spectra, as can be seen in Figure 15.

Baseline correction is usually done by selecting some points in the spectra that are free from absorption, and do not have other interferences. If there are changes in the slope of the baseline, at least two baseline correction points have

to be used. In practice, the points are replaced by regions, over which the signal is averaged. In this way the effect of noise in the baseline corrected spectra is minimised.

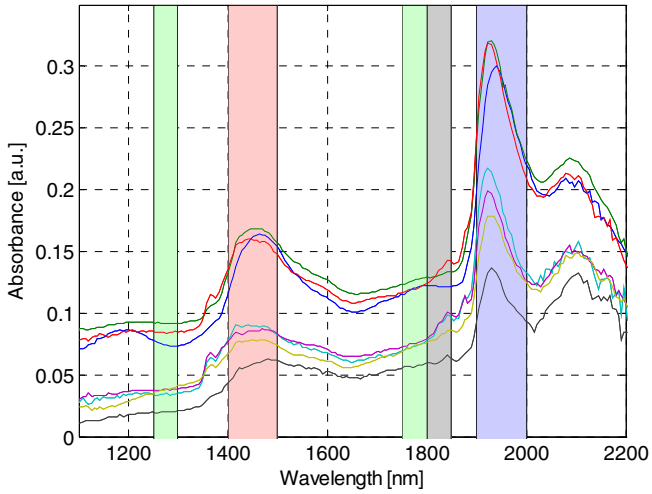

Figure 16. Different regions used for absorption band height calculations. Baseline correction regions (green), water 1440 nm band region (red), water vapour band region (grey), and water 1940 nm band region (blue) are shown. Some top reflection absorbance spectra are shown for reference (solid lines).

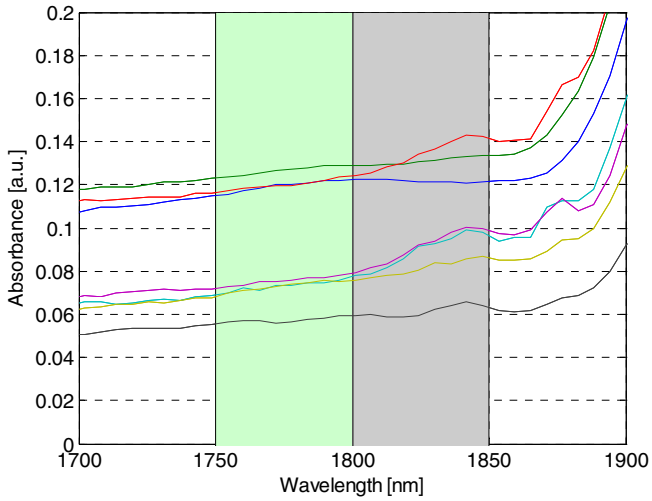

Figure 17. Top reflection absorbance spectra with a baseline region (green) and the water vapour band region (grey).

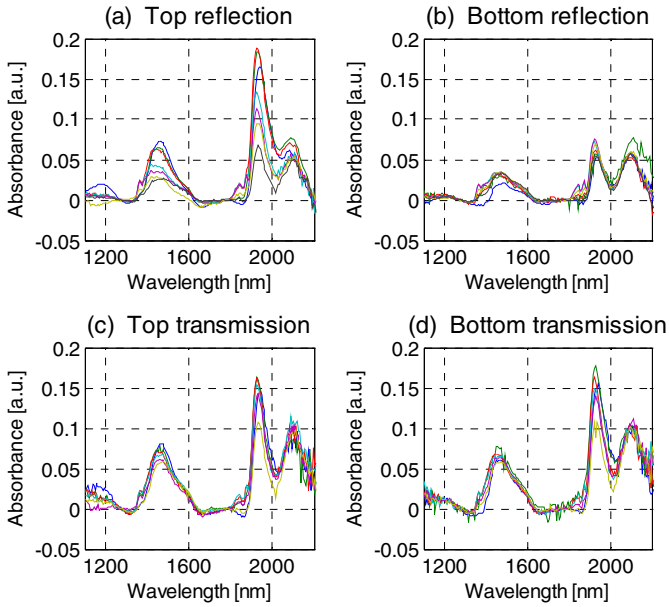

Figure 18. Top reflection (a), bottom reflection (b), top transmission (c), and bottom transmission (d) absorbance spectra collected during a typical trial point. Baseline correction has been applied to the spectra. The different colours correspond to the seven measurement positions.

At least two baseline correction regions had to be used since there are slight slope variations in the baseline (see Figure 15). On the other hand, there were only limited possibilities to use more regions. According to tests, two baseline correction points was enough to remove the baseline variations from the spectra. The spectral regions 1250–1300 nm and 1750–1800 nm were selected for the baseline correction (see Figure 16). These regions are sufficiently far away from each other that the slope of the baseline is not sensitive to noise. The 1750–1800 nm region is close to the water absorption band at 1940 nm, which is desirable in baseline correction. Moreover, the water vapour bands [60] at 1340–1400 nm and 1800–1900 nm are avoided.

The result of the baseline correction is seen in Figure 18. For all practical purposes, only the variation in the water bands is left. In the top reflection case the high amount of water at the beginning of the coating process makes the 1940 nm water band overlap with the cellulose band at 2100 nm. In all other cases the cellulose absorption band does not change with changing moisture levels,

meaning the baseline correction has removed the effects of changes in the scattering properties. This is good news since it also means that the water band should now correlate linearly with the moisture content of the paper.

The selection of the absorption band for moisture predictions was rather straightforward. There were two possibilities: the 1440 nm band and the 1940 nm band. The 1940 nm band was chosen because of its better sensitivity to water, and because the cellulose band at 2100 nm is not overlapping (Figure 16). In the 1440 nm water band the cellulose band at about 1490 nm is overlapping, introducing an offset into the water response and making the interpretation of results somewhat harder. Still, some results using the 1440 nm water band will be examined because it is interesting from a measuring equipment point of view. The devices providing wavelength response up to 1700 nm are cheaper than those providing response up to 2000 nm or higher. In addition, the different absorption and scattering properties at the 1440 nm region make it interesting to compare with the 1940 nm region.

Another issue that had to be taken into account is the effect of temperature. It is generally known that it shifts the absorption bands of water [103], and this can actually be seen in Figure 16. A broad integration region of 1900–2000 nm was chosen for the water band to minimise the interference from this shifting effect. The use of narrower regions was tested but it led to dependence of results on the shift of the band, i.e. on temperature.

The top-side reflection moisture value indicates the moisture of the coating and the uppermost part of the paper. Similarly, the bottom reflection moisture indicates the moisture in the lowermost part of the paper. On the other hand, the transmission measurements probe the whole paper. In the blade coating process, water is added only on the top side of course. Many conclusions about what is happening in the coating process can be drawn based on considering the different moisture values as a function of time. The conclusions especially include the absorption of water into the base paper, and drying of the paper.

Typically, NIRS moisture measurements are calibrated against the gravimetric method to show the absolute moisture content of the sample. This kind of calibration was not performed in this work for three reasons. First, the primary goal was to monitor the changes taking place during the coating process, and

exact moisture calibrations are not necessarily needed for this. Second, since different coating colours, different base papers and different coat weights were tested, a lot of calibration work would have been needed to get reliable results. Third, it is very difficult to measure calibration samples with a wet coating layer and a dry base paper. In fact, the NIR moisture measurement is a primary moisture measurement method in this work, as long as moisture depth profiling is concerned. However, estimates of the absolute moisture levels can be made based on the response of water in the spectra.

There were two alternatives to predict the concentration of water vapour: the 1340–1400 nm region and the 1800–1900 nm region [60]. Here again the better response of the 1800–1900 nm region made it the choice. The same baseline correction method and regions as in the moisture calculations could be used in this case. The water band absorption region had to be limited to 1800–1850 nm since above 1850 nm the liquid water begins to absorb significantly (see Figure 17). The water vapour absorption band is small in the spectra, but it has enough signal-to-noise ratio to provide valuable information on the process.

In addition to the moisture and water vapour calculations, two important results were calculated from the measured spectra. The specular reflection intensity and the diffuse reflection intensity (called scattering in this thesis) at a certain wavelength indicate the state of the coating colour during the coating process. The specular reflection intensity was obtained by calculating the average value of the specular reflection spectrum over a region that is free of absorption. The scattering signal was obtained in a similar way from the top reflection spectrum. Recall that the spectra were normalised with the base paper spectra.

A good choice for the calculation region was the first baseline correction region, 1250–1300 nm (see Figure 19). The dynamics in the specular reflection signal are large, whereas the scattering changes are rather small. Note that the specular reflection result is calculated in the NIR range. Thus, the results may not be directly comparable to gloss measurement results, which are typically done in the visible spectral range and with a 75 degrees measurement angle. In fact, the specular reflection measurement is slightly wavelength-dependent at high specular reflection values (see Figure 19). This is probably due to the fact that the coating looks more uniform the longer the wavelength. This means that using

different wavelength regions to calculate the specular reflection and scattering intensities would result in slightly different results.

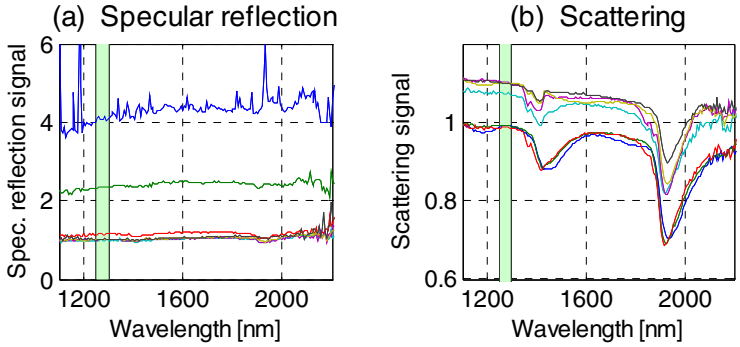

Figure 19. The normalised specular reflection and scattering spectra in measurement positions 1–7 (different colours). The green area is the calculation region of specular reflection and scattering.

However, despite the normalisation, the specular reflection signal suffered from small systematic errors. The signal from the specular reflection probe comes from two sources: first, the actual specular reflection signal is due to specular reflection on the surface, and second, the light that is not specularly reflected produces a diffusely reflected signal from the inner layers of the paper. When there is no coating on the paper the actual specular reflection signal is very weak and the specular reflection measurement resembles the scattering measurement. On the contrary, when there is a wet coating layer on the base paper the actual specular reflection signal is very strong, but the diffuse reflection signal is still on an approximately same level as in the uncoated situation.

Regarding the two sources of the specular reflection signal, it can be concluded that the normalisation with the base paper only normalises the diffuse reflection part of the signal. The diffuse reflection part is not sensitive for small angle deviations, but the actual specular reflection signal is. Thus there is a need to normalise the specular reflection signal with a glossy standard to get rid of small deviations from probe to probe arising from geometrical deviations. A glossy paper was used for this purpose. It was run through the machine with the dryers not functioning, in the same way as the base paper before each trial point.

The corrected signal G_n^{corr} is obtained in the following way:

$$G_n^{corr} = c_n \left(G_n - 1 \right) + 1 , \tag{12}$$

where G_n is the measured specular reflection signal (normalised by the base paper signal), and c_n is the correction coefficient for measurement position n. The coefficients are determined from signal of the glossy paper by the following formula:

$$c_n = \frac{\bar{G}^{glossy} - 1}{G_n^{glossy} - 1} \tag{13}$$

where G_n^{glossy} is the signal of the glossy paper from measurement position n, and $\bar{G}^{glossy}$ is the mean of these signals.

In Figure 20 the specular reflection signal before the correction is shown in (a) and the signal after the correction in (b). There are quite remarkable differences between the specular reflection signals of different measurement positions. However, the correction ensures that the specular reflection signals are comparable to each other, at least on the specular reflection levels of 1–4.

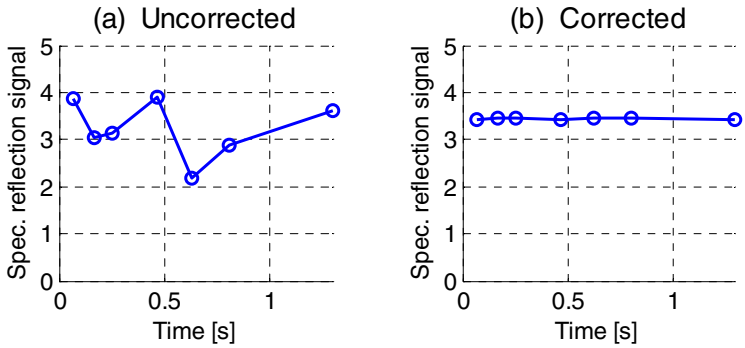

Figure 20. Specular reflection signal before correction (left) and after correction (right).

4.3 Measurements on laboratory coater

This section describes the measurements that were performed on the laboratory-scale coater KCL-Saukko (hereafter referred to as "laboratory coater"). KCL-Saukko is intended to simulate the paper coating process on the laboratory scale. It has a jet applicator and a coating blade, and uses a closed, circulating paper web. In a typical coating experiment the paper web is accelerated to about 1000 m/min, the coating is applied and the web is decelerated in fractions of a second, after which the paper web remains stationary.

In this thesis the laboratory coater measurements are only briefly described, concentrating on the cases, which are helpful in understanding the on-line measurements. More detailed description of the laboratory measurements can be found in the Master of Science thesis "Paper moisture depth profiling by using near infrared spectroscopy and gloss measurement" by Lehtonen [104]. That thesis concentrated on the laboratory coater measurements and on other laboratory measurements that were carried out to study the properties of the measurement system.

4.3.1 Configuration at laboratory coater

The same probes were used in the laboratory coater measurements as in the on-line measurements. However, there was only one measurement point and the specular reflection, scattering and moisture values were followed as a function of time. This is in contrast to the on-line measurements, where seven measurement positions were distributed along the drying section. Yet another difference is that there was no drying machinery in the laboratory measurements.

The MCT spectral camera was used in the same manner as in the on-line measurements, and a similar double-chopping light source was used (see Section 4.1). The only difference was that the light source only provided the illumination to one measurement position. The measurement setup at the laboratory coater is depicted in Figure 21. The measurement principle was exactly the same as in the on-line case (see Section 4.1). The distance from the coating blade to the measurement position was about one meter. This means about 0.06 seconds on the time scale with a web speed of 1000 m/min.

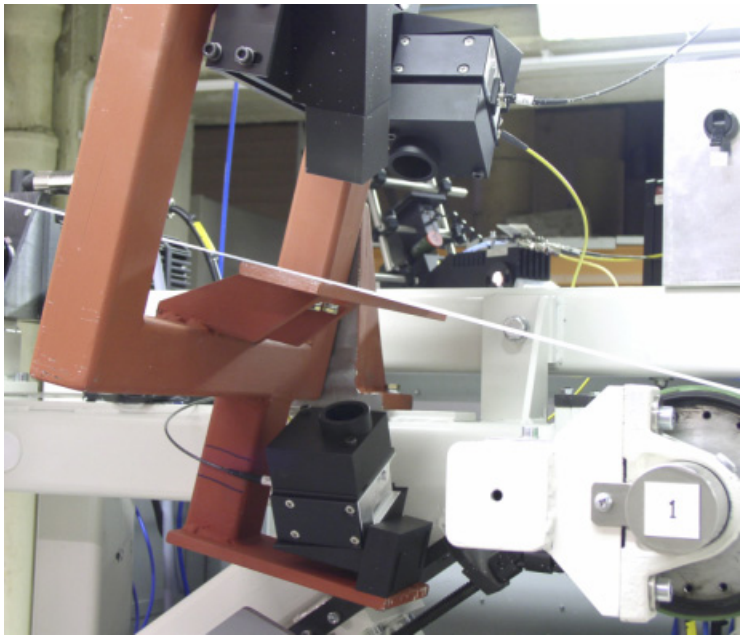

Figure 21. The measurement setup installed on the laboratory coater.

4.3.2 Coating and water spraying experiments

Two kinds of measurements were performed on the laboratory coater: coating trials and water spraying trials. The coating trials mimicked the situation in a real paper coating process, whereas the water spraying trials were performed to gain understanding of the measurement system and its depth-profiling properties.

A typical coating trial measurement was done in the following way:

1. The web was stationary and the collection of data was started.
2. The web was accelerated and the coating was started. The coating process lasted some fractions of a second.
3. The web was decelerated until it was stationary.
4. The optical measurement was stopped after a suitable collection time.

In the water spraying trials the measurement was started, water was sprayed onto the measurement spot and the measurement was continued until the paper was dry, or at least up to the point where the water concentration gradient had levelled.

Processing of the measurement data was done in a similar fashion to the on-line measurements case. The data processing methods are discussed in detail in Section 4.2.3. The difference was that there was only one measurement point in the laboratory coater measurements, so any data processing related to standardisation between measurement points was not needed. The calculation of absorbance spectra, and specular reflection, scattering and moisture data was done as described in Section 4.2.3. The only difference was that the temporal behaviour of these quantities was examined, as compared to the on-line case where the different measurement positions formed the “time scale”.

5. Determination of the optical properties

One of the main goals of this thesis is the theoretical analysis of the depth profiling properties of the measurement method described in the previous chapter. The analysis is based on a theoretical model for the measurement method, which will be described in detail in Section 6.2. The model is phenomenological in nature and needs some experimentally determined parameters as input. The most important of these parameters are the optical properties of the base paper and coating colour as a function of moisture. The optical properties include the absorption and scattering coefficients and the anisotropy factor as a function of wavelength. The measurements and theoretical calculations to determine the optical properties are described in this chapter, and the resulting absorption and scattering coefficients and anisotropy factors are presented.

5.1 The inverse Monte Carlo model

The radiative transfer equation (Equation (3)) and different approximations to solve it were discussed in Section 2.3. However, regardless of the approximation used, the optical properties of the sample must be known in order to be able to simulate diffuse reflection or transmission signals. In most approximations this means knowing the absorption and scattering coefficients. The more sophisticated approximations also use the scattering phase function, which is often described by the anisotropy factor. The determination of these parameters requires careful measurements and calculations. It should also be noted that the definition of the coefficients may differ in different approximations. The most well known example of this is the difference in the absorption and scattering coefficients defined in the framework of the Mie theory, as opposed to those of the Kubelka–Munk theory [46].

The MCML Monte Carlo code provides an approximation to the RTE, which uses the Henyey–Greenstein function (Equation (5)) to describe the scattering phase function. The diffuse reflectance, diffuse transmittance and collimated transmittance of a one-layer sample can then be expressed as functions of the absorption and scattering coefficients and the anisotropy factor: $R = R(\mu_a, \mu_s, g)$, $T = T(\mu_a, \mu_s, g)$ and $C = C(\mu_a, \mu_s, g)$. From a mathe-

matical point of view, these expressions constitute the forward model. To determine the absorption and scattering coefficients and the anisotropy factor from the measurements, the inverse problem has to be solved, i.e. the functions $\mu_a = \mu_a(R,T,C)$, $\mu_s = \mu_s(R,T,C)$ and $g = g(R,T,C)$.

If the analytical forms of the *R*, *T*, and *C* functions were known, it would be possible to express the absorption and scattering coefficients and the anisotropy factor as analytical expressions. This kind of inversion is possible, for example, for the Kubelka–Munk expressions for reflectance and transmittance, Equations (6) and (8). But, in the case of the Monte Carlo simulation, the functions *R*, *T*, and *C* can only be approximated at one point at a time by running the simulation with the optical properties as parameters. The solution to the inverse problem must, therefore, employ the direct model. There are two common ways of dealing with this kind of problem: one is to use iterative methods [49] and the other is to use lookup tables [105]. In this work the iterative method was chosen, and more precisely the iterative Newton algorithm. Algorithms of this kind have been well described in the literature [49]. Thus the description of the algorithm used in this work is left to the Appendix.

5.2 Measurements

The optical properties of the base paper and the coating colour as a function of moisture are needed for the Monte Carlo simulation of the measurement signals. The optical properties include the absorption and scattering coefficients and the anisotropy factor, as well as the refractive index. All these are needed to know as a function of wavelength in the near-infrared spectral region. Section 5.1 described the inverse Monte Carlo technique to calculate the optical properties based on diffuse transmission and reflection, and collimated transmission measurements. In this section the emphasis is on the details of these measurements. The refractive index of the base paper or the coating colour was not measured, but it was estimated based on some special criteria.

5.2.1 Instrumentation

The inverse Monte Carlo method needs the absolute diffuse reflection, diffuse transmission and collimated transmission measurements as input. Absolute collimated transmission measurement is just the normal way of doing transmission measurements, but the absolute diffuse reflection and transmission measurements have to be performed with the aid of an integrating sphere. The Varian Cary 5000 spectrometer (Figure 22) has been used for the measurements in this thesis. It is a two-beam spectrometer based on a monochromator, with a spectral range of 175–3500 nm. The two-beam operation principle provides high accuracy in the measurements since it compensates for various drift effects, for example the drift in light source intensity.

Figure 22. The Varian Cary 5000 spectrometer.

The standard transmission accessory of the Varian spectrometer was used for collimated transmission measurements. For diffuse reflectance and transmittance measurements, the DRA-2500 integrating sphere accessory was used (see Figure 23). The DRA-2500 has a polytetrafluoroethylene coating, a PbS detector for the NIR spectral range and a photomultiplier tube for the ultraviolet – visible spectral range. The spectral range of the integrating sphere is 200–2500 nm. It has ports for transmission and reflection measurements, and a reference port.

In the two-beam operation mode of the spectrometer the sample beam and reference beam are alternately illuminating the integrating sphere. In addition to the high accuracy this gives the advantage of compensating for the effects arising from the integrating sphere wall reflectance and port sizes. In a normal single-beam instrument these have to be corrected by calculations [49].

The geometry used in the integrating sphere measurements is shown in Figure 24. The plane of the reflectance port was tilted so that the specular reflection from the sample hits the wall of the integrating sphere. This was done to ensure that the specular reflection is included in the measurement, which is the easiest case from the inverse Monte Carlo calculations point of view. It would also have been possible to exclude the specular reflection by directing it out from the sphere. However, the surface roughness of the samples makes the specular reflection angle distribution quite wide. The inclusion of the specular reflection in the integrating sphere should then be more similar to the Monte Carlo simulations, where one cannot account for the angle distribution of the specular reflection.

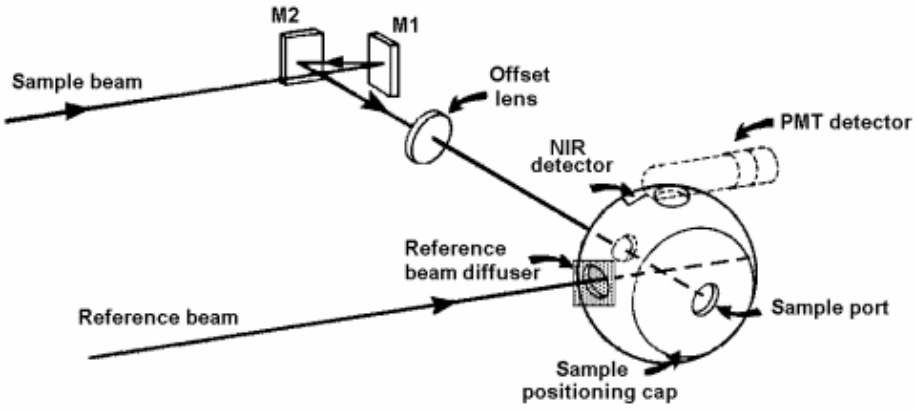

Figure 23. The ports and detectors of the DRA-2500 integrating sphere accessory used with the Varian Cary 5000.

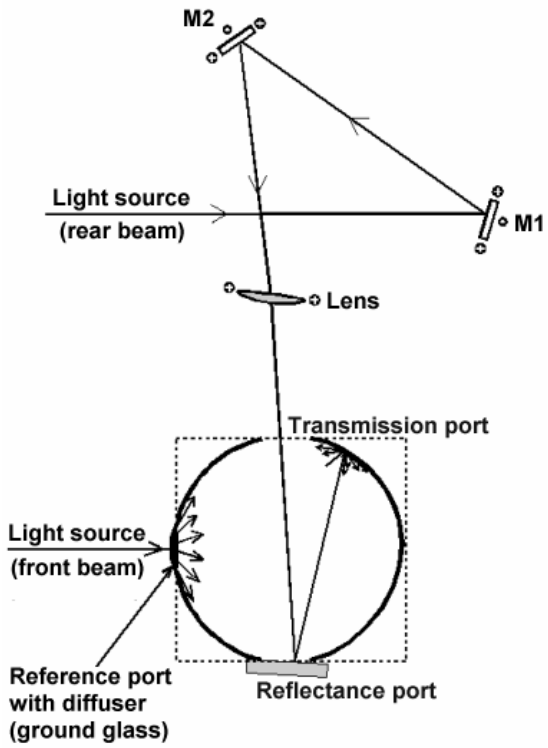

Figure 24. The geometry used in the integrating sphere measurements.

5.2.2 Measurement procedure for the base paper

The measurement procedure for the diffuse reflection and transmission from a base paper sample as a function of moisture was selected after testing several alternatives. The main difficulty is how to keep the moisture content of the paper constant during the measurements. This was achieved by sandwiching the wet paper between two 1 mm quartz plates. This combination will be called the *base paper cuvette.*

Because of the standardisation procedure of the Cary spectrometer, the diffuse reflection and transmission measurements were performed separately. The procedure for both measurements was as follows:

1. The sample was thoroughly wetted under a normal tap. The excess water was removed by placing the sample between two paper towels. After that, the sample was placed in between the quartz plates.

2. The weight of the base paper cuvette with the paper was measured using precision scales before the diffuse reflection or transmission measurements.

3. The sample was placed on the reflection port or transmission port of the integrating sphere (see Figure 24).

4. The measurement was performed; it took a few minutes with the measurement parameters used.

5. The sample was removed from the integrating sphere and weighed again.

6. The base paper cuvette was opened and the paper was left to dry for a while.

7. The base paper cuvette was closed and the procedure was repeated from step 2 until the paper achieved its equilibrium moisture content.

The above measurement procedure was first used to measure the diffuse reflectance as a function of moisture. After that, the paper was rewetted and the same procedure was used in the measurement of the diffuse transmittance as a function of moisture. Finally, the paper was dried in an oven at 105 °C and the diffuse reflectance and transmittance were again measured, along with the weighing before and after the measurements.

The moisture content of the paper sample in each measurement was calculated based on the mean of the weights before and after the integrating sphere measurement, the dry weight of the sample, and the weight of the quartz plates. An attempt was made during the measurements to get the same moisture content of the paper sample in the reflection and transmission measurements. However, this was not achieved exactly. The diffuse reflection and transmission have to be measured at exactly the same moisture levels in order to be usable in the inverse Monte Carlo calculations. To achieve this, the measurement results were

interpolated to the same moisture contents. This is justified by the slow changes in the measured spectra as a function of moisture. On the other hand, the standardisation procedure of the instrument makes it difficult to measure the diffuse reflection and transmission in succession.

The collimated transmission measurements were only performed for room-dry base paper since they are only needed for the determination of the anisotropy factor. Because of the difficulties discussed in Section 5.3, the anisotropy factor was not determined as a function of moisture.

5.2.3 Measurement procedure for the coating colour

The measurement procedure for coating colours was also selected based on several tests. Here again the problem is that the moisture content has to be kept constant during the measurements, and there must also be a way to dry the sample gradually. Quartz plates were used to form the base paper cuvette in the base paper measurements described in the previous section. The same quartz plates were used in this case. This time, however, spacers were inserted between the glass plates. The coating was applied onto one of the quartz plates, and the other was placed on top of the spacers to prevent the quartz plate touching the surface of the coating layer. A schematic of the cuvette is shown in Figure 25. The cuvette can be opened to let the coating layer dry. When the cuvette is closed, the moisture content of the coating layer stays constant within the accuracy of the precision scales.

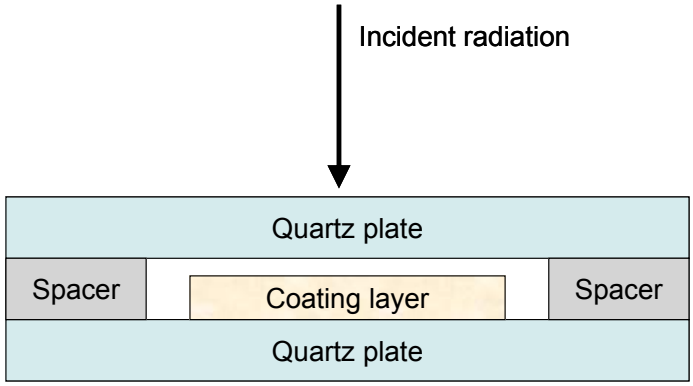

Figure 25. The structure of the cuvette used in coating colour measurements.

The coating colour was applied to the quartz plate using 30 µm or 50 µm thick aluminium sheet stencils. There was a 30 mm diameter hole in the sheets to define the area of the coating layer formed on the quartz plate. The procedure for applying the coating was as follows:

1. The stencil was placed on top of the quartz plate.

2. A small amount of coating colour was placed in the middle of the stencil hole.

3. The stencil was swept several times with the edge of a glass plate so that a uniform coating layer was formed.

4. The stencil was removed.

The procedure yielded quite nice coating layers with a circular shape. There were small amounts of coating colour outside the circle, but their weight was negligible compared to the weight of the circle. The uniformity of the coating layer was studied by eye and by a gauge micrometer. Of course, only the dry coating layer could be measured by the gauge micrometer. Within the accuracy of the micrometer, the coating layer was uniform, and it also looked uniform to the eye. Of course, the coating layer was not exactly uniform, but the coating method described above was the best that could be found in this work.

The thickness of the wet coating layer was selected for use in the inverse Monte Carlo calculations. The average thickness was calculated by calculating the grammage of the wet coating layer based on its area and weight, and converting it to thickness by dividing by the measured density of the wet coating colour. Typically, the average wet coating layer thickness was about 40 µm when using the 50 µm stencil, and about 25 µm when using the 30 µm stencil.

The procedure for measuring the diffuse reflection and transmission of the coating colour sample was somewhat different to the base paper case described in the preceding section. The reason was that the diffuse reflection and transmission are needed at the same moisture levels. However, in the case of the coating layer one cannot use the interpolation technique described in the previous section because the changes in the measurement results are very rapid

when the coating colour reaches the second critical concentration. Therefore, the diffuse reflection and transmission were measured in succession, without standardising the instrument between these measurements. This introduces a small error in the diffuse reflection measurements, but the error was estimated to be below 0.5 percentage units. Compared to other sources of error in the preparation of the sample, this is negligible.

The procedure for measurement of the diffuse reflection and transmission of the coating colour as a function of moisture was the following:

1. The coating layer was formed on the bottom quartz plate. The spacers and the top quartz plate were put onto the bottom plate immediately.

2. The weight of the cuvette was measured using precision scales before the diffuse transmission measurement.

3. The sample was placed on the transmission port of the integrating sphere (see Figure 24).

4. The transmission measurement was performed.

5. The sample was removed from the integrating sphere and weighed again.

6. The sample was placed on the reflection port of the integrating sphere (see Figure 24).

7. The reflection measurement was performed.

8. The sample was removed from the integrating sphere and weighed again.

9. The cuvette was opened and the coating colour was left to dry for a while.

10. The cuvette was closed and the procedure was repeated from step 2 until the coating colour achieved its equilibrium moisture content.

The moisture content of the coating colour in its equilibrium state under room conditions was about 0.5%. This was determined separately with a thick coating colour layer, which was dried in the oven at 105 °C for two hours. The error caused by the precision scales in the moisture was about 0.7%. Thus the equilibrium moisture content was taken as the zero moisture level.

The most important source of error in the above procedure is that the coating colour begins to dry from the edges first. Thus the coating colour reaches the critical points at different times at different positions on the coating layer. Fortunately, the edge effects were not so effective in the central part of the coating layer and there the critical concentrations were reached simultaneously. Therefore, the reflectance and transmittance were measured in the central part of the coating colour. However, the non-uniform drying of the coating colour has an effect on the results since it affects the weight of the coating layer. The moisture content in each measurement is the average moisture content of the whole coating layer, but not the moisture content at exactly the measurement position. The error introduced by this is very difficult to avoid. This error was estimated to be no more than a few percentage units. This is low enough for the purpose of the coated paper simulations.

The collimated transmission had to be measured separately because the integrating sphere accessory and the normal transmission accessory cannot be used simultaneously. Because of this, one coating layer sample was measured with the following procedure: the collimated transmission of the wet coating layer was measured first. The accessory was then changed to the integrating sphere, and the diffuse reflection and transmission were measured. After that, the coating layer was dried to room-dry moisture, and the diffuse reflection and transmission were measured, followed by the collimated transmission after the replacement of the accessory. In this way, all three measurements for the wet coating and dry coating were obtained. The collimated transmission at other moisture levels was not measured because it would have required the change of the accessory at each moisture level.

5.3 Optical properties of the base paper

The determination of the absorption and scattering coefficients, as well as the anisotropy factor, requires careful measurements and theoretical calculations. The measurements were described in Section 5.2. The inversion procedure needed to convert the measurements into optical properties was discussed in Section 5.1.

5.3.1 Measurement results

The starting point for the determination of the optical properties is the measurements. The diffuse reflection and transmission spectra of the base papers at different moisture levels were collected as described in Section 5.2.2. The results are shown in Figure 26 and Figure 27. The diffuse reflection intensity decreases when increasing the moisture, whereas the opposite is true for the diffuse transmission. These observations are caused by the increase in scattering coefficient with moisture. The water absorption bands at 1440 nm and 1940 nm are also clearly seen in the curves.

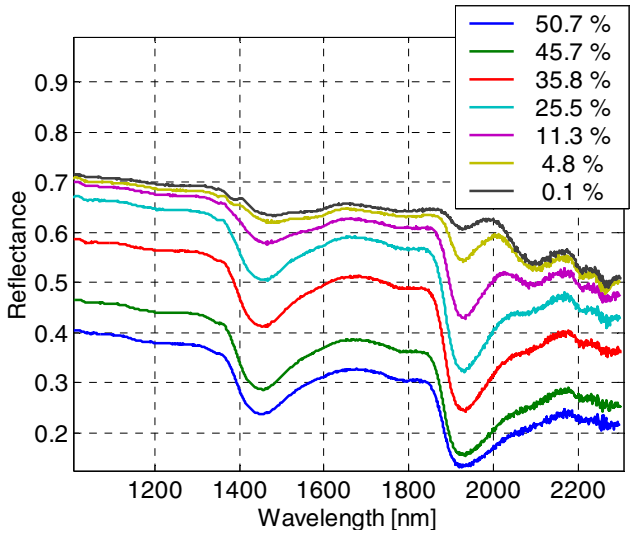

Figure 26. The diffuse reflection spectra of the base paper at different moisture levels.

In the calculation of the optical properties, the sample must not change between the measurements of diffuse transmission and reflection. An attempt was made to measure the diffuse reflection and transmission at exactly the same moisture levels. However, this was not achieved. Thus interpolation methods had to be used to get artificial diffuse reflection and transmission spectra with the same moisture levels. The errors introduced by this procedure are negligibly small since the spectra behave smoothly as a function of moisture (see Figure 26 and Figure 27).

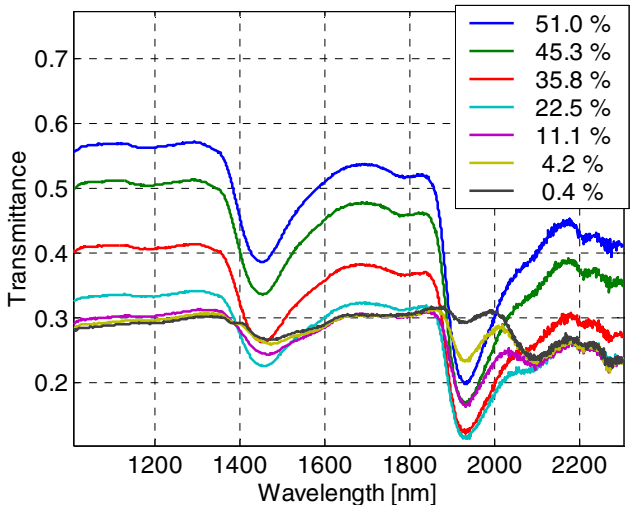

Figure 27. The diffuse transmission spectra of the base paper at different moisture levels.

5.3.2 Assumptions used in the calculations

The determination of the optical properties is based on some assumptions about the paper sample. The homogeneous, or continuum, approximation described in Section 2.3 is used. In a nutshell, the approximation assumes that the paper is a homogeneous slab of material with known refractive index, absorption and scattering coefficient, anisotropy factor and thickness. All polarisation effects are neglected.

The absorption and scattering coefficients and the anisotropy factor are determined by the inverse Monte Carlo procedure. In the calculations, the other parameters

need to be given as input, namely the thickness of the sample and its refractive index. A slide calliper was used to measure the thickness of a stack of 24 base paper sheets, which resulted in a thickness value of 75 μm for one paper sheet.

The determination of the refractive index of the paper is a challenge for two reasons. First, the homogeneous approximation uses an *effective* refractive index, which should be chosen so that the behaviour of light in the sample is as realistic as possible. Second, the effective refractive index may depend on the moisture content of the paper.

In the MCML Monte Carlo model, the refractive indices of the layers make the rays reflect and refract on the boundaries according to the Fresnel equations. However, the paper fibres are up to 20 μm thick, so the surface of the paper is optically very rough for the 1–2 μm wavelengths considered in this thesis. Thus the light rays do not refract and reflect according to the laws of geometrical optics in the air–paper and coating–paper interfaces.

In the determination of optical properties of powder samples, the effective refractive index of the sample is usually assumed to be one [73]. This is a reasonable assumption for a loose powder with particle sizes much greater than the wavelength. With paper samples, there are no fundamental reasons why one could not make the same approximation. It means that no reflection and refraction occurs on the paper surfaces. In reality, there are complex reflections and refractions from the fibres and other particles, but these are similar to the refractions and reflections occurring inside the paper. The reflections and refractions are accounted for by the effective scattering coefficient of the paper. Thus when a light ray passes the air–paper interface, it is not reflected or refracted according to the laws of geometrical optics in planar boundaries. It only deviates from its original direction when it encounters a scattering centre. The paper–air interface is modelled as a transition from a scattering to a non-scattering medium, much like a transition from a cloud to air. Of course, this approximation leads to some non-physical results such as too short time-of-flight for the light rays, which, however, is completely irrelevant to the simulation goals of this work. Moreover, setting the refractive index larger than one would lead to some peculiarities in the MCML Monte Carlo model. For example, the inverse model would not converge at low absorption regions.

The above reasoning may not be valid for very wet paper (moisture content above 30–40%). At these high moisture levels most of the pores of the paper are filled with water. Therefore, the Fresnel reflections and refractions begin to behave more like in a homogeneous slab of material. However, for the sake of simplicity, the value 1.0 was selected for the effective refractive index of the base paper at all moisture levels. This is justified by the fact that in the paper coating process the base paper is mostly dry throughout the whole process.

5.3.3 The anisotropy factor

The inverse Monte Carlo code is, in principle, able to determine the anisotropy factor, in addition to the absorption and scattering coefficients. The determination of the anisotropy factor was tested with a dry base paper sheet, based on measurements of diffuse reflection and transmission, and collimated transmission. The calculation results in an anisotropy factor ranging from about 0.2 to 0.3. This is surprisingly low since the diameter of the fibres in the paper sample is much larger than the wavelength of the light. However, the calculation of the anisotropy factor for paper is not very stable for two reasons. First, the intensity and signal-to-noise ratio of the collimated transmission measurement are low. Second, the illumination and collection half-angle of the Varian Cary 5000 spectrometer collimated transmission measurement are about 4–5 degrees. The number of snake photons (photons scattered by chance so that they are collected as collimated transmission) is even greater than the number of ballistic photons when measuring the base paper. This can be seen by comparing the simulated collimated transmittance with the measured one. In practice, much smaller illumination and collection half-angles would be needed to get a reliable estimation of the anisotropy factor; the measurement of g is usually done with lasers.

Because of the difficulties described above, it was decided to use $g = 0$ in the simulations of the paper samples since the determined anisotropy factor is so near zero, and since the determination of g for the paper samples was not fully reliable. Since relatively thick paper samples are considered in the simulations (compared to the mean free paths of the photon), the effect of this assumption is quite small. Note that this assumption also means the determined scattering coefficient is, in practice, the *reduced scattering coefficient*.

5.3.4 Absorption and scattering coefficients

The absorption coefficient spectra of the base paper as a function of moisture are shown in Figure 28. The changes in water absorption bands at 1440 nm and 1940 nm dominate the structure of the spectra. The cellulose absorption band at 2100 nm is only visible at low moisture values. The height of the 1940 nm water band at the 50.7% moisture level is about 135 cm^{-1}. The height of this band for pure water is about 115 cm^{-1}, as reported by Hale and Querry [5]. At first glance there is a clear discrepancy. One reason for this is that the paper swells as its moisture content increases. For simplicity, it has been assumed in the determination of the optical properties that the thickness of the paper does not change. This assumption leads to an overestimation of the absorption coefficient at high moisture levels. Another reason for the high absorption coefficient is that the homogeneous model of the paper is very simple; it cannot take account of all reflections, refractions and scattering events occurring in the sample. Yet another reason for the high absorption coefficient is that an anisotropy factor of zero was assumed in the calculations. This makes the absorption coefficients higher since zigzag photon trajectories are effectively replaced by straight lines in this assumption.

The assumption of non-swelling paper is used in all simulations exploiting the calculated absorption and scattering coefficients. This means that although this assumption overestimates the absorption coefficient of the wet paper, the same assumption corrects the situation in the simulation; the effect of the overestimated absorption coefficient is compensated by the underestimated thickness of the paper.

The reduced scattering coefficients of the base paper at different moisture levels are shown in Figure 29. They behave as expected in many respects. First, they decline towards longer wavelengths. Second, the scattering coefficient decreases as a function of moisture. Third, the mean free path for photons in dry paper calculated from the scattering coefficient is about 20 μm, meaning practically all light transmitted through the base paper is multiply scattered. As expected, the water absorption bands at 1440 nm and 1940 nm do not show up, apart from the small anomalies at high moisture levels. These are due to the homogeneous approximation used in the calculations, which cannot account for all scattering, reflection and refraction effects taking place in the sample. The approximation of effective refractive index of one may also play a role.

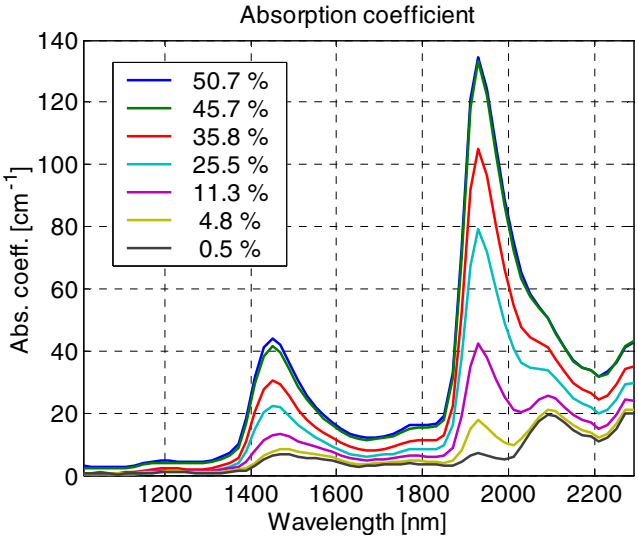

Figure 28. The absorption coefficients of the base paper at different moisture levels.

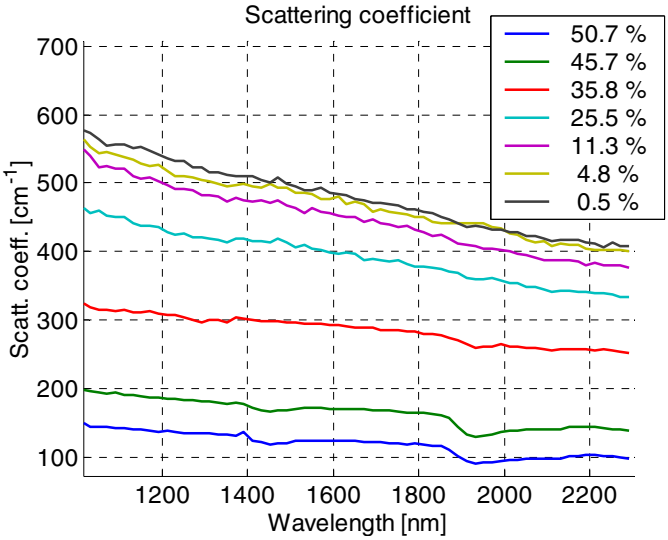

Figure 29. The reduced scattering coefficients of the base paper at different moisture levels.

5.4 Optical properties of the coating colour

5.4.1 Assumptions used in the calculations

The same homogeneous sample approximation that was used in the calculations of the optical properties of the base paper (see Section 5.3.2) also applies in the case of coating colour. The thickness of the coating colour has to be measured and the refractive index has to be determined in some way.

The measurement procedure for the diffuse reflection and transmission for the coating colour was described in Section 5.2.3. The determination of the thickness of the coating colour layer is not trivial, mainly because the thickness changes as a function of moisture. Details of this shrinking phenomenon are not known well, and the amount of shrinking depends on many conditions [20]. Because of this, a constant thickness of coating layer was used, i.e. the shrinking as a function of moisture is not taken into account. This approximation simplifies the simulations. Specifically, the thickness of the wet coating layer is used. It can be easily determined from the density, mass and area of a coating layer formed on a quartz substrate (see Section 5.2.3).

There are three reasons for selecting the thickness of the wet coating layer as the thickness parameter. First, the thickness of the wet coating is relatively easy to determine, as discussed above. Second, the thickness of the wet coating does not remarkably depend on the drying conditions or substrate; this may not be true for the thickness of the dry coating because different drying and different substrate materials can lead to a different structure of the dry coating layer. Third, the interest in the simulations is particularly on the situation at the beginning of the drying phase of the coated paper, where the coating layer is rather wet. The effect of the constant thickness approximation in coated paper simulations is rather small, as was discussed in the case of the same approximation for the base paper (see Section 5.3.2).

The refractive index, as in the case of the base paper, is rather challenging to determine. As discussed above, the emphasis of the simulations will be on the wet coating. Coating colours typically include particles that are smaller than 2 μm in diameter – that is, their size is comparable to the wavelengths used in the measurement system of this thesis. Thus the reasoning that led to an effective

refractive index of one in the case of the base paper is not applicable here. On the contrary, there are reflections and refractions in the coating layer – air and coating layer – base paper interfaces. To a first approximation, the reflections and refractions obey the laws of geometrical optics. Thus an effective refractive index that is something in between the refractive indices of water and the solid materials is anticipated.

The measurement of the refractive indices of coating colours or pigment slurries has received some attention in the literature [106]. However, the studies usually concentrate on the visible spectral region, and it is also very difficult to find measurement results for coating colours that resemble those used in this work. Therefore, an approximate theoretical treatment is presented to get a reasonable approximation for the effective refractive index. Different refractive indices for the coating layer have been tested in the Monte Carlo simulations. As a result, the refractive index differences have to be in the order of 0.1 before they have a significant effect on the simulation results. Hence the goal of the theoretical treatment is to find an approximate effective refractive index that is accurate enough for the Monte Carlo simulations.

The theoretical calculation of the effective refractive index of suspensions has received quite a lot of attention in the literature [107–110]. The Mie theory has been used to calculate the effective refractive index for spherical particles. The relatively simple formula derived by van de Hulst [65] and cast in a different form by Champion et al. [107] was selected for the calculations:

$$n_{eff} = n_w + \frac{3 n_w v_s}{8 x_r} P'_{sca}, \tag{14}$$

where n_{eff} is the effective refractive index, n_w is the refractive index of water, v_s is the volume fraction of solids, $x_r = 2\pi r n_w / \lambda$ is the size parameter with r the radius of the solid particles and λ the wavelength. P'_{sca} is the so-called refraction efficiency, which depends only on x_r and the relative refractive index $n_{rel} = n_c / n_w$, where n_c is the refractive index of the solid particles. The refraction efficiency is given in terms of the Mie coefficients as follows [107]:

$$P_{sca}^{'} = \frac{4}{x_r^{\,2}} \cdot \mathrm{Im}\{S(0)\}$$
$$S(0) = \frac{1}{2}\sum_{k=1}^{\infty}(2k+1)(a_k + b_k) \qquad (15)$$

where $S(0)$ is the complex forward scattering amplitude, and a_k and b_k are the Mie coefficients [65].

Equation (14) is strictly valid only for spherical particles, and for dilute suspensions. However, Alexander et al. [110] have performed experiments on turbid suspensions and show that n_{eff} is linearly dependent on the volume fraction, even at high values of v_s, which is just what Equation (14) predicts. The shape of kaolin particles is far from spherical [111], but taking the particle shape into account would require the use of very sophisticated simulation techniques.

To calculate the effective refractive index based on Equation (14), one needs the radius of the particles, wavelength of interest, the refractive index of water and the solid materials, and the volume fraction of the particles. The coating colours used in this thesis consisted mainly of calcium carbonate, kaolin, and latex. The volume fraction of latex is ca. 20% from solid material. There are also small amounts of thickeners and other substances. For simplicity, only the calcium carbonate and kaolin are taken into account in the following calculations. The mean particle size of calcium carbonate and kaolin pigments used in coating colours is typically roughly one micrometer [111]. Thus the particle radius is approximated to be 0.5 µm. The particle size distribution is neglected for simplicity.

The wavelength region of interest in this thesis is 1.0–2.2 µm. The refractive index of the particles is approximated to be 1.55. This is an approximate compromise of the refractive indices of calcium carbonate (1.53–1.54) [112] and kaolin (1.56) [113] in the near-infrared region. It should be noted that calcium carbonate is a birefringent material. However, because the MCML Monte Carlo model does not take polarization into account, the birefringence may have an effect on the optical properties determined. Such effects are most probably small. The refractive index of water at 1.0–2.2 µm varies between 1.327–1.296

[5]. The imaginary parts of the refractive indices are neglected since they are very small.

The volume fraction of the solid materials has yet to be determined. It can be expressed in the following way:

$$v_s = \frac{V_s}{V_c} = 1 - \frac{V_w}{V_c} = 1 - m\frac{\rho_c}{\rho_w}, \tag{16}$$

where V_s is the volume of solids, V_w is the volume of water, V_c is the total volume of the coating colour, m is the moisture content and ρ_c the density of the coating colour, and ρ_w the density of water. The density values used were ρ_c = 1.56 g/cm^3 (a measured value for one of the coating colours used in the trial runs at KCL), and ρ_w = 1.00 g/cm^3. With a moisture content m = 37% (a typical initial moisture content of the coating colour) one gets the value v_s = 0.42 for the volume fraction of solids.

Table 2. Calculation parameters for the effective refractive index of the coating colour, used in Equations (14), (15) and (16).

Parameter	***Symbol***	***Value***	***Reference/source***
Radius of particles	R	0.5 µm	[111]
Wavelength	λ	1.0–2.2 µm	–
Refractive index of water	n_w	1.327–1.296	[5]
Refractive index of solids	n_c	1.55	[112, 113]
Density of coating colour	ρ_c	1.56 g/cm^3	Measured
Density of water	ρ_w	1.00 g/cm^3	–
Moisture content of coating colour	m	37%	Coating colour recipe

Using the values for parameters described above, and summarised in Table 2, one can calculate the effective refractive index of the coating colour. The result is n_{eff} = 1.408–1.419 in the spectral range 1.0–2.2 µm. The result is almost exactly in between the refractive indices of the solid particles (1.55) and water (1.327–1.296).

The particle size dependence was neglected in the calculation. Recalculations with different particle radii showed that this dependence is only remarkable above 2 μm particle sizes. The particles in the coating colours used in this thesis are mostly smaller than 2 μm. For example, 90% of the particles in the HC-90 calcium carbonate pigment are smaller than 2 μm. Hence the assumption that the average particle radius a = 0.5 μm is a good approximation.

According to Equation (14), the effective refractive index changes as a function of moisture since the volume fraction of solid particles also changes. The coating is dried in the paper coating process, i.e. its moisture content decreases and the volume fraction of solid particles increases. At the second critical concentration the volume fraction of solids is typically about 0.8. Since Equation (14) was originally derived for the dilute approximation, it cannot be reliably used to estimate the effective refractive index at the SCC. However, one can roughly estimate that the effective refractive index must be rather close to the refractive index of the solid particles, namely 1.55.

After the second critical concentration, air begins to penetrate the coating layer. The refractive index of the dry coating layer may be rather different from the wet coating layer. For reasons already discussed in the case of the base paper (see Section 5.3.2), it is also questionable whether the use of an effective refractive index higher than one is justified in the dry coating layer. For the sake of simplicity, an effective refractive index n_{eff} = 1.45 has been selected to be used in all coating layer simulations. It has been rounded up slightly from the values 1.408–1.419 calculated above. The reason is that the interest in the simulations is mostly in coating colour moisture levels occurring between the coating blade and the SCC. The value n_{eff} = 1.45 is an approximate average over the effective refractive indices at these moisture levels.

5.4.2 The anisotropy factor

The measurements to determine the optical properties of the coating colour were performed with the Varian Cary spectrometer equipped with an integrating sphere accessory as described in Section 5.2.3. Due to the details of the measuring equipment, it is rather difficult to measure the diffuse reflection, diffuse transmission and collimated transmission from the same coating colour sample in succession. All these measurements are needed if the anisotropy factor

is to be determined in addition to the absorption and scattering coefficients. Because of this difficulty, the anisotropy factor was determined at only two moisture levels: wet coating colour and dry coating colour.

The measured diffuse reflection and transmission, as well as collimated transmission spectra of the coating colour for 36.3% and 2.7% moisture levels, are shown in Figure 30. The scattering coefficient of the dry coating is higher than that of the wet coating. This shows up in the higher diffuse reflectance intensity of the dry coating, and, correspondingly, in lower intensities in the transmittance curves of the dry coating.

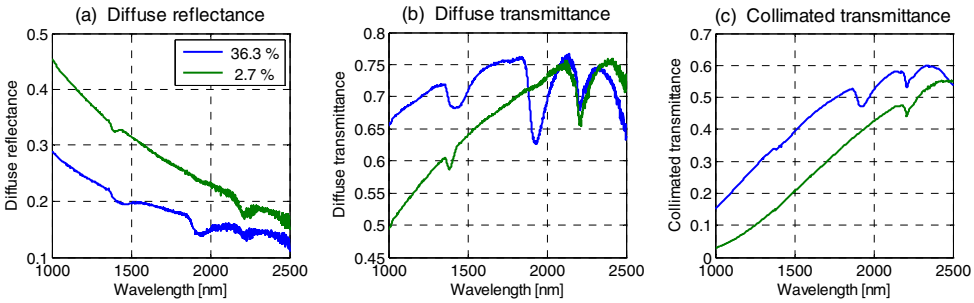

Figure 30. Diffuse reflectance (a) and transmittance (b), and the collimated transmittance (c) of the coating colour at two moisture levels.

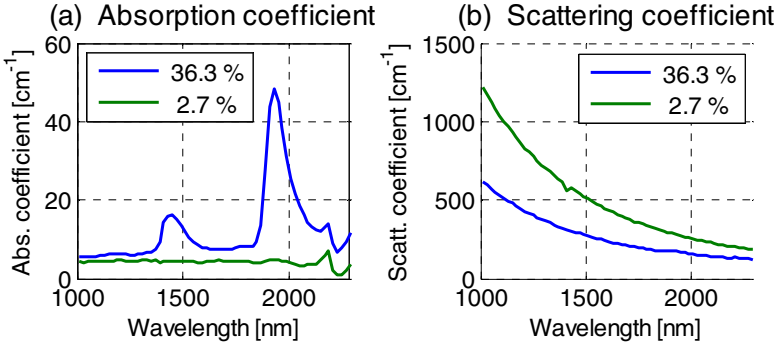

Figure 31. The absorption coefficient spectra (a) and scattering coefficient spectra (b) of the coating colour at two moisture levels.

The absorption and scattering coefficient spectra of the coating colour are shown in Figure 31. The absorption is dominated by the water absorption bands at 1440 nm

and 1940 nm. The spectral features at 2200 nm are due to the quartz material of the cuvette used in the measurements. Although the absorption and refractive index of the quartz is taken into account in the inverse Monte Carlo calculations, the model is not perfect and some anomalies are left in the spectra. Fortunately, the 2200 nm spectral region is not used in the analysis based on the simulation data. The scattering coefficient approximately doubles when the coating colour dries.

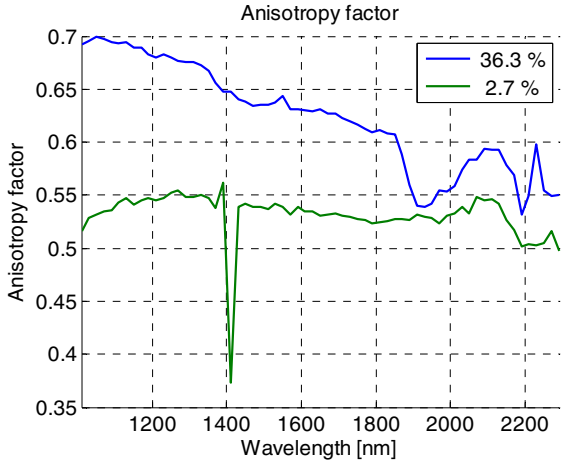

Figure 32. The anisotropy factor g of the coating colour at two moisture levels.

The calculated anisotropy factor is shown in Figure 32. There is some anomaly at 1400 nm in the 2.7% curve, most probably due to the stochastic nature of the inversion procedure. Since the anisotropy factor differs remarkably from zero, and the coating layer is optically rather thin, the anisotropy has to be taken into account in the simulations. However, as discussed above, the anisotropy factor was only determined at two extreme moisture levels. A reasonable approximation is to assume a mean anisotropy factor of $g = 0.6$, which has been used in the inverse calculations and also in the simulations for this thesis. The approximation is justified by the relatively small changes of the anisotropy factor between wet and dry coating colours, and by the small dependence of g on wavelength.

5.4.3 The absorption and scattering coefficients

To calculate the optical properties of the coating colour as a function of moisture, the diffuse reflectance and transmittance spectra were measured at 11

different moisture levels. The starting moisture percentage was 38.3%, and the end moisture was 3.9%. The decrement was about 3 percentage units. Figure 33 shows the measured diffuse reflectance and transmittance for six moisture levels. The spectra at the remaining five moisture levels are not shown for clarity. When the coating colour starts to dry, the diffuse reflectance decreases first. This decrease is due to the particles getting closer to each other, which makes their scattering power weaker [20]. There is a turning point at about the 20% moisture level, where the diffuse reflection starts to increase again. This is the second critical concentration.

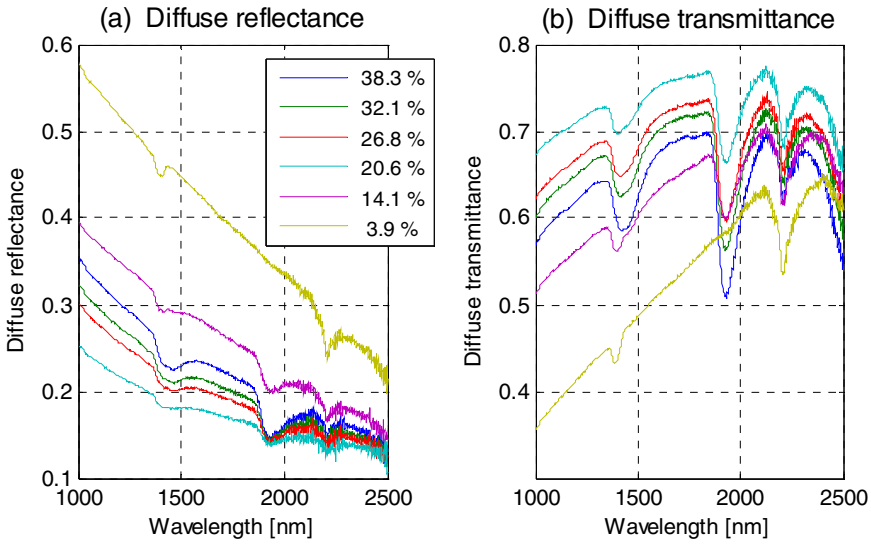

Figure 33. Diffuse reflection (a) and diffuse transmission (b) spectra of the coating colour at different moisture levels.

The absorption coefficient spectra at the different moisture levels are presented in Figure 34. A somewhat surprising feature is that the water absorption bands are so weak at 3.9% moisture, which indicates that the water may be bonded to the coating particles so that it is not visible in the normal water absorption bands.

Figure 35 shows the scattering coefficient spectra. Here again, the second critical concentration is clearly observable. Note that the scattering coefficient is calculated with $g = 0.6$, which means the reduced scattering coefficient is 0.4 times smaller than the values reported here.

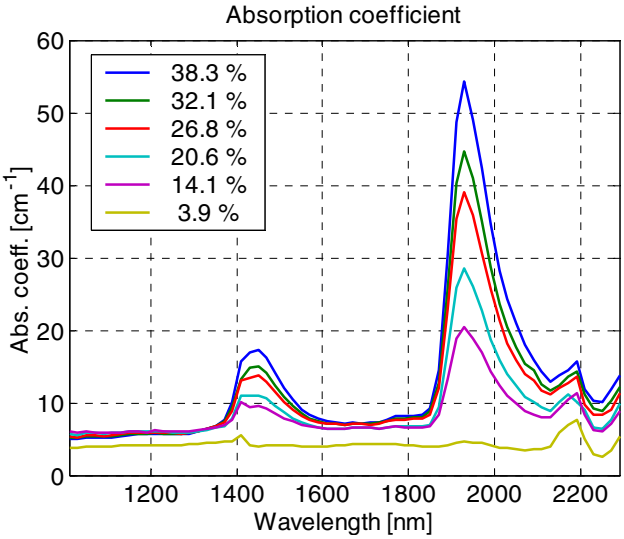

Figure 34. The absorption coefficient spectra of the coating colour at different moisture levels.

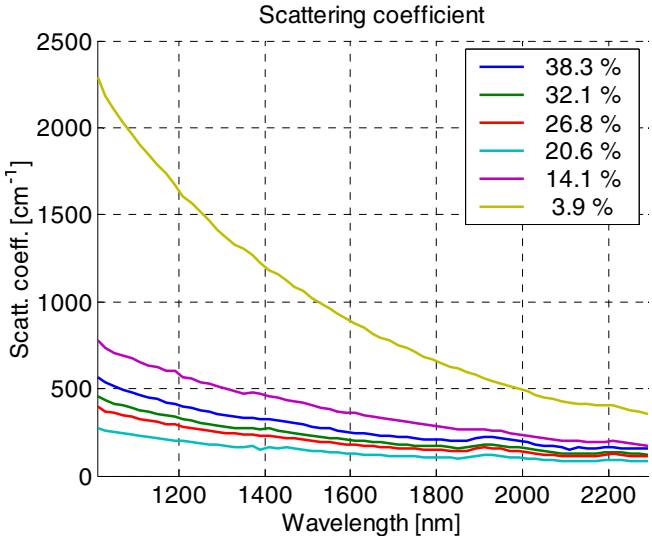

Figure 35. The scattering coefficient spectra of the coating colour at different moisture levels.

It is interesting to compare the absorption coefficient at 1940 nm water band to the absorption coefficient reported in the literature for pure water, which is about

113 cm^{-1} [5]. The density of the coating colour is 1.56 g/cm^3, meaning a basis weight of 15600 g/m^2 for a 1 cm layer. At the 38.3% moisture level there is 5970 g/m^2 of water in the layer, which corresponds to 0.597 cm thickness. From this it can be concluded using the Lambert–Beer law that the absorption coefficient of the coating colour should be $0.597 \cdot 113\ cm^{-1} = 67.5\ cm^{-1}$. The corresponding absorption coefficient determined by the inverse Monte Carlo method is about 53 cm^{-1} (Figure 34). There is a slight discrepancy, which may be related to the very small water absorption band at 3.9% moisture, as discussed above. Another issue here is the fact that the absorption and scattering coefficients determined by the inverse Monte Carlo method are effective. In fact, there is a small bump in the scattering coefficient spectra at about 1940 nm at high moisture levels (see Figure 35). This bump makes the absorption coefficient smaller since it increases the photon path lengths inside the sample. However, the important thing from the point of view of the simulations is that the absorption coefficient is approximately the same as that for a corresponding layer of liquid water. This means that the Monte Carlo model describes the physics of the light propagation in the sample reasonably well.

6. Theoretical analysis of the measurement method

In this section, some important properties of the measurement system and method are analysed theoretically. The motivation for this analysis is twofold. First, the measurement signals from the coated paper are difficult to interpret because of the inhomogeneity of the sample. Second, there are many measurement geometries used, and the goal is to extract the moisture depth profile from the measurement results. This is a demanding task, which requires a thorough understanding of the physics of the measurement. The theoretical analysis gives a better understanding of what is actually being measured, and makes it possible to get more quantitative depth profiles. The properties of the model are described first, and then the simulation results are compared with the measurement results. After this, the depth-profiling properties of the measurement system are simulated and analysed.

6.1 Monte Carlo model

As discussed in Section 2.3.3, the structure of the paper samples is very complicated. In modelling radiation behaviour inside the paper samples there are three possibilities. First, one may try to take the structure of the paper into account as accurately as possible. Second, a very simple structural model can be used. Third, the paper can be treated as a homogeneous substance, and the light propagation described by scattering and absorption coefficients. This is called the continuum approximation.

The continuum approximation was used in this thesis since the interest is not particularly in the structure of the coating layer or the base paper. In fact, the moisture depth profiling goal itself uses the continuum ideology: the interest is in the moisture content in the coating layer or at different depths in the base paper, but not in exactly where the water is located in the structure of the coated paper. Another reason for using the continuum theories is the fact that, as discussed earlier, the structure of paper and the coating layer is very complex and the structure extends from the nano scale to even the millimetre scale. The continuum theories offer a simple approach to the situation: it is simply assumed

that the coating layer and the base paper are homogeneous, and the calculations and conclusions are based on this assumption. Still, some points will be made about the weaknesses of this assumption whenever they are obvious and could have an essential influence on the modelling results.

In the case of this work, a reasonable level of complexity satisfying the modelling needs in a coated paper sample would have the following properties:

- The sample consists of plane-parallel layers.
- Each layer is homogeneous.
- The optical properties of the layers taken into account are
    - scattering coefficient μ_s
    - absorption coefficient μ_a
    - scattering phase function p as a parameterised expression
    - refractive index n_l
    - thickness t_l.
- Capability of calculating the diffuse reflectance and transmittance, and collimated transmittance of the sample.

The so-called MCML Monte Carlo code by Wang et al. [48] offers all the capabilities listed above, and was selected as the simulation engine of this thesis. A Matlab interface to the MCML Monte Carlo code was developed. This combines the well-tested and fast code of the MCML with the powerful numerical processing and graphical presentation capabilities of Matlab.

The MCML code assumes a pencil beam of light impinging perpendicularly on the sample surface. This assumption is not valid in the experimental measurement system; of course, the illumination light beam never has an infinitely small radius, but also the beam subtends an angle of 30 degrees with regard to the sample surface normal. A modification of the MCML code was made to take this into account. The geometry implemented in the modified MCML code is shown in Figure 36.

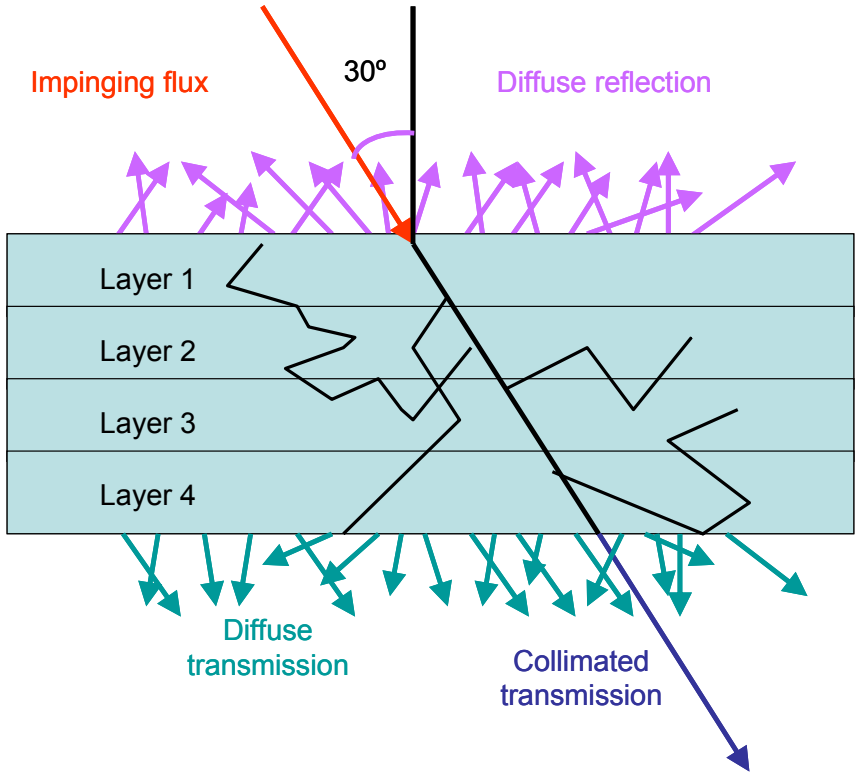

Figure 36. The geometry implemented in the modified MCML code. The diffuse reflection and transmission, and collimated transmission directions are also shown.

The MCML code simulates the behaviour of one light ray at a time in the sample. The algorithm used for scattering and absorption procedures inside the sample can be summarised as follows:

1. Randomly generate the free path for the light ray according to the total attenuation coefficient $\mu_a + \mu_s$.
2. Move the ray to a new position.
3. Decrease the intensity of the ray according to the absorption coefficient.
4. Simulate the scattering process by randomly generating a new direction to the ray according to the Henyey–Greenstein scattering phase function.
5. Go back to 1.

The above is a simplified version of the actual algorithm used in the MCML code. The reflections and refractions in the interfaces of the layers are also taken into account, among other things.

Only a brief description of the MCML code has been given here. This thesis does not go into further details since they are well described elsewhere [48].

6.2 Theoretical model for the measurement method

The theoretical model used to simulate the reflection and transmission signals arising from a coated paper sample is described in this section. The model will be referred to as the "measurement system simulation model", and briefly as MSSM. The MCML Monte Carlo code (see the previous section) is used as a workhorse in the model. This section concentrates on the models for the absorption and scattering coefficients of the coating layer and base paper, and also on the calculation of the output signals.

6.2.1 Approximations used in the model

Since the MCML code is used as the simulation engine, the approximations of the MCML code also apply to the model for the coated paper. From the point of view of light behaviour in a coated paper, these approximations mean the following:

- The coating is a uniform layer on the base paper; in practice, the coating thickness varies and the surface of the base paper is rough.
- The coating and the base paper are treated as being homogeneous; in practice, they comprise different particles and fibres that scatter, reflect, and refract light in a very complex way.
- The specular reflection on the surface of the coating layer, and in the boundary between the coating layer and the base paper, are described by the Fresnel equations, where the surfaces are plane-parallel; in practice, the specular reflections in these surfaces are very complicated. However, the Fresnel equations provide a simple approximation, which is quite

reasonable. More complex approaches would require information about the roughness of the surfaces, which is very difficult to obtain.

- The swelling or shrinking of the base paper and the coating as the moisture content varies is not taken into account. This is called the *non-shrinking approximation*.

The main assumption is that the paper is divided into plane-parallel, homogeneous layers. For example, three layers can be used: the coating layer, the penetration layer just beneath the coating layer, and the rest of the base paper. All of these layers have four parameters: type (coating or base paper), refractive index, thickness and moisture content. The refractive index and thickness can be passed directly to the MCML code, but the moisture content along with the type information has to be converted into the optical properties of the layer. This conversion is done with the the functions $\mu_a^{coating}(m,\lambda)$, $\mu_s^{coating}(m,\lambda)$, $g^{coating}(m,\lambda)$, $\mu_a^{base}(m,\lambda)$, $\mu_s^{base}(m,\lambda)$, and $g^{base}(m,\lambda)$, where m is the moisture content, and λ is the wavelength. The analytical form of these functions is difficult to determine; one has to use interpolation to estimate these coefficients based on measurement data. Details of the measurements and interpolation methods involved can be found in Section 5.2.2.

6.2.2 Comparing simulations to measurements

Once the moisture information on the layers has been converted into the optical properties, all parameters can be given to the Monte Carlo code. The Monte Carlo code calculates the intensity of the scattered light as output. However, the intensity information cannot be used as such because it should be compared to the measurements. To this end, two issues must be considered: simulation geometry and the reference sample.

Simulation geometry

Ideally, the simulation geometry should mimic the measurement geometry as well as possible. This is reasonable in the case of an integrating sphere measurement setup where the total diffuse transmission or total diffuse reflection is collected. However, in a typical NIR on-line measurement, the collection solid

angle is only several thousandths of the whole hemisphere. Moreover, the illumination and collection beam diameters and their position relative to each other are important.

While constructing the exact measurement geometry in the Monte Carlo simulation is possible in principle, it leads to very long simulation times in order to obtain adequate statistical estimates. Thus a trade-off between resemblance of the simulation to the measurement, and reasonable simulation times has to be considered. In the on-line measurement system of this thesis, the diffuse reflection is collected at a 30 degrees angle to the surface normal. A collection cone of 10 degrees half-angle was used in this work. The justification for selecting 10 degrees is twofold. First, the angle has to be below 30 degrees since a collection cone of 30 degrees half-angle would have led to acceptance of rays subtending angles of 0 degrees and 60 degrees to the normal of the sample. This would be too far from the collection at 30 degrees used in the measurements. The second reason is that going to smaller collection half-angles than 10 degrees leads to very long calculation times.

In addition, the illumination beam has a zero radius and the collection beam an infinite radius. The measurement system uses an illumination spot of about 7 mm in diameter and a collection spot of about 2 mm in diameter. However, the relative positions of these spots depend on the measurement distance, and on the sample thickness. The exact modelling of the spot sizes would be a very challenging task. Moreover, since the paper sample is very thin compared to the spot sizes, the effect of the spot sizes on the simulation results should be minimal.

Reference sample

The measured reflectance or transmittance is not usually used as such, but the ratio of the signal to the signal measured from a reflectance standard, or the *reference sample*, is calculated. To be able to compare the simulated reflectances and transmittances to the measured ones, a similar ratioing procedure has to be performed for the simulated quantities. To this end, the absorption and scattering coefficients of the optical teflon disk used as a reference material in the on-line measurements were determined. Then, the reflection and transmission signals from the optical teflon sample were simulated with the same geometry as was used

in the simulation of the coated paper. The simulated reflectance and transmittance can then be divided by the corresponding simulated quantities of the reference sample. With this procedure one gets simulated reflectance and transmittance that are directly comparable to the measured reflectance and transmittance.

Once the intensity of the scattered radiation has been converted into quantities comparable to measurements, the reflectance and transmittance as a function of wavelength can be calculated, i.e. the reflectance and transmittance spectra. From this point on, the calculation proceeds in exactly the same manner as in the processing of the real measurement data, including transformation into the absorbance units and baseline corrections. This allows the direct comparison of simulated and measured results of scattering and moisture values. Details of the measurement data processing can be found in Section 4.2.3.

6.3 Simulation of on-line measurements

The MSSM model to simulate on-line measurements was presented in Section 6.2. In this section the feasibility of the model in predicting base paper and coated paper spectra is tested. The simulation results are compared with the measurement results from the trial runs. The optical properties determined in Chapter 5 are used in the simulations.

The most important parameters of the MSSM model include the number of photons used in the simulation, the wavelength to be considered, the number of layers and their type (base paper or coating), and the thickness and moisture content of the layers. Typically, the diffuse reflection and transmission spectra were simulated in the wavelength range 1000–2300 nm, with 20 nm intervals. One million photons were used at each wavelength. This produces a reasonable approximation of the reflection and transmission spectra. The simulation time using a normal personal computer with a Pentium 4 processor is about one minute per wavelength, resulting in about one hour total simulation time for one simulated measurement. When considering only simulated moisture results, not the whole spectra, it sufficed to simulate only those wavelengths that are used in the water absorption band height calculations, namely the baseline correction and absorption band regions.

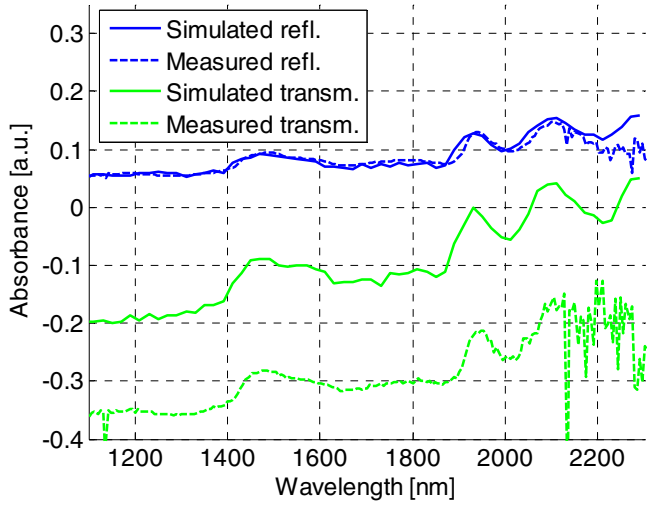

Figure 37. The simulated and measured diffuse reflection and transmission spectra of the uncoated base paper. The measured spectra are from trial runs and the simulated spectra are calculated with the MSSM model.

The simulated and measured diffuse reflection and transmission spectra of the uncoated base paper are compared in Figure 37. The measurement results are from the trial runs before the start of one trial point. Thus there is no coating on the paper. The measurement results are from measurement position one, where the paper still has its original moisture content of about 4%. The MSSM model was used with the optical properties of the base paper at the 4% moisture level in the simulations. The spectra are not distinguished as "top" or "bottom" reflection or transmission because there is no difference between "top" and "bottom" in the case of base paper.

The correspondence between the measured and simulated results is excellent, especially for the reflection spectra. There is an offset between the simulated and measured transmission spectra, but in other respects the spectra are very alike. The offset is mainly due to the slightly inhomogeneous transmission properties of the reference disk used in the on-line measurements. This inhomogeneity causes intensity variations in the reference measurement, which leads to baseline variations in the measured transmission spectra. The signal-to-noise ratio of the

measurement system above 2100 nm is low, which is shown in the wild behaviour of the spectra in that region.

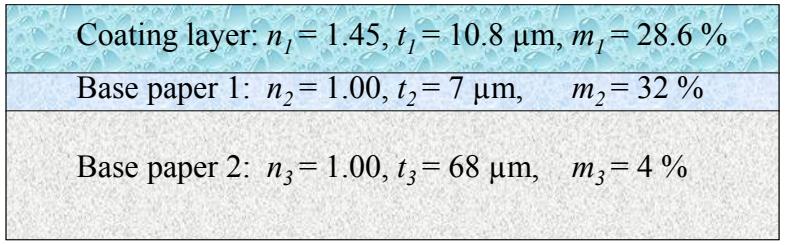

Figure 38. The depth profile used in the coated paper simulation. The refractive index n_l, thickness t_l and moisture content m_l (l is the layer number) are specified for each of the three layers.

Figure 38 shows the structure of the coated paper and an associated moisture depth profile that are used in the simulation of coated paper with the SMMS model. The moisture depth profile has been selected to resemble that of a particular trial point from the trial runs at the first measurement position on the KCL coating machine. The refractive indices are those selected for the coating layer and base paper in Sections 5.3 and 5.4. The thickness of the coating layer is calculated from the coat weight at the trial point (10.6 g/m^2) and the solids content and density of the coating colour (63% and 1.56 g/cm^3 respectively). The thickness of the base paper is 75 µm, and it is divided into two layers: the penetration layer (layer 1) and layer 2. The thickness and moisture content of the penetration layer are approximate values from the mass and heat transfer calculations performed at KCL. The moisture content of the coating layer has been adjusted using the assumption that no water has evaporated from the coated paper at this position, i.e. only transport of water has occurred. Layer 2 has the initial moisture content of the base paper. This layer structure is a simplistic model of the situation at measurement position one, where some of the water has penetrated from the coating layer to the base paper but drying has not been started.

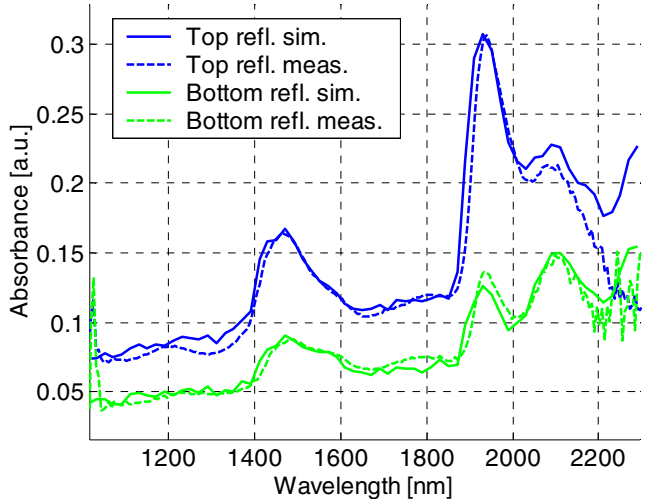

Figure 39. Simulated and measured absorbance spectra of the reflection measurements.

The spectra from the coated paper simulations, along with the corresponding measurement results, are shown in Figure 39 and Figure 40. As opposed to the base paper simulation above, there is now a difference between "top" and "bottom" geometries. The simulated and measured reflection spectra (Figure 39) show excellent correspondence with both the "top" and "bottom" geometries. Note that the bottom reflection spectra resemble those of the reflection geometry in Figure 37, which is an indication that the bottom reflection moisture measurement does not see the excess water in the coating layer. This is equally true for both simulated and measured spectra.

The simulated and measured transmission spectra (Figure 40) much resemble each other in respects other than that there is an offset. The reason for the offset is the slightly inhomogeneous reference material, as was discussed above when analysing the base paper simulation results. The same reason also explains why the top and bottom transmission signals do not coincide as their simulated counterparts do.

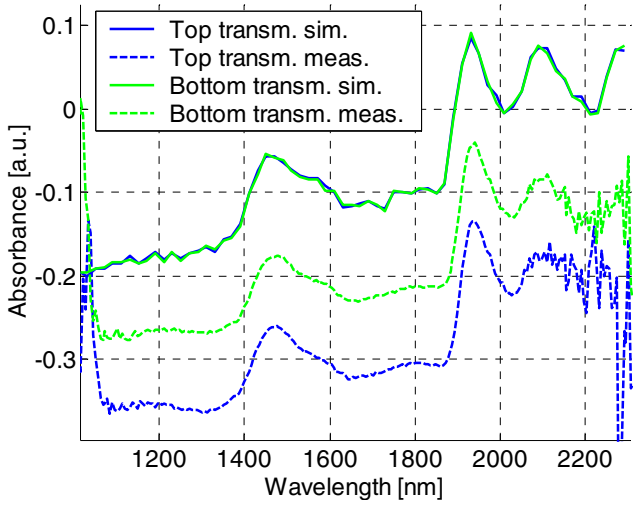

Figure 40. Simulated and measured absorbance spectra of the transmission measurements.

Kurki et al. [58] presented a more detailed and complete feasibility study regarding the use of Monte Carlo-based techniques in the simulation of NIR measurements on paper. Kurki et al. show that Monte Carlo models similar to that used in this thesis can be used to predict the NIR measurement signals of real process instruments.

The conclusion of this feasibility study on the SMMS model is that an excellent correspondence between the measured and simulated spectra was attained for both base paper and coated paper simulations. Thus the SMMS model captures the essential physics of the measurement and the model can be used for analysis of the properties of the measurement method. Note that the optical properties are separately determined for the coating colour and the base paper using a laboratory instrument that differs from the on-line measuring equipment in many aspects. The good correspondence between the baseline levels of the measured and the simulated spectra is especially surprising since, typically in spectroscopic measurements, the baseline levels are more or less arbitrary.

6.4 Depth profiling properties of the measurement method

The spectral simulation results from the MSSM model were presented in the previous section. The MSSM model also gives the possibility to theoretically analyse the properties of the multimeasurement system developed. A detailed analysis of the depth profiling properties of the multimeasurement system is performed in the following sections. First, the depth sensitivity of the measurement is defined theoretically, and then the depth sensitivities of the measurements in base paper and coated paper are calculated and analysed. The results give new insight into the physics of the measurements, as well as provide valuable information for the analysis of the measurement results.

6.4.1 Definition of depth sensitivity

The top and bottom reflection moisture measurements are inherently depth-sensitive. They see the water on the surface of the paper most efficiently, but their ability to detect moisture from the inner layers of the sample decreases rapidly as a function of the depth of the layer. The depth sensitivity or effective sample size of near-infrared diffuse reflection spectroscopy has attained some interest in the literature [40, 41]. Berntsson et al. [40] point out that the penetration depth of the radiation does not define the effective sample size. They introduce a theoretical and experimental method to assess the effective sample size in pharmaceutical powders. Both methods are based on calculating the ratio between the reflectance of a finite-thickness sample and a sample of infinite thickness. Berntsson et al. then draw conclusions about the contribution of layers at different depths to the diffuse reflection spectrum. They also qualitatively distinguish between the fraction of reflected light from a certain layer and the fraction of information from that layer. However, they do not even define what is exactly meant by “information”. An exact definition of depth sensitivity of NIR spectroscopic measurements is lacking.

There are two questions about depth sensitivity that naturally arise: first, how sensitive to different depths is the spectrum of a particular NIR spectroscopic measurement? And second, how sensitive to different depths is the concentration predicted from the spectrum? The *spectral depth sensitivity* provides the answer

to the first question, and it will be defined first. Then, it will be generalised to get the *application-specific depth sensitivity*, which provides an answer to the second question. The diffuse reflection measurement of moisture will be used in the terminology in the definitions, but the definition is directly applicable to other measurement geometries and other analytes as well.

Assume an infinitely large planar, turbid sample, and let z be the coordinate in the thickness direction of the sample. The sample extends from $z = 0$ to $z = d$. The sample is also assumed to have an arbitrary moisture depth profile, described by the function $m(z)$, as depicted in Figure 41. Of course, $m(z) \equiv 0$ outside $0 \le z \le d$. The diffuse reflectance at a certain wavelength λ can be expressed as a functional of the moisture depth profile: $D_\lambda = D_\lambda[m(z)]$.

The response of the functional D_λ to a small change in the function $m(z)$ is the functional derivative of D_λ, denoted by δD_λ. The functional derivative is itself a functional, and may be evaluated with a test function f as follows [114]:

$$\langle \delta D_\lambda[m], f \rangle = \frac{d}{d\varepsilon} D_\lambda[m + \varepsilon f]\Big|_{\varepsilon=0}. \tag{17}$$

The ε is merely a parameter used to evaluate the derivative. This equation is useful when one wants to know the response of the diffuse reflection measurement D_λ to a certain variation f of the moisture depth profile. If the analytical form of the functional D_λ is not known, one can approximate the functional derivative in the following way:

$$\langle \delta D_\lambda, f \rangle \approx D_\lambda[m(z) + f(z)] - D_\lambda[m(z)]. \tag{18}$$

Applications of this formula are presented in Sections 6.4.2 and 6.4.3. Note that although $m(z)$ was defined to be the moisture depth profile, it can be replaced by any function that is dependent on z and alters the value of D_λ.

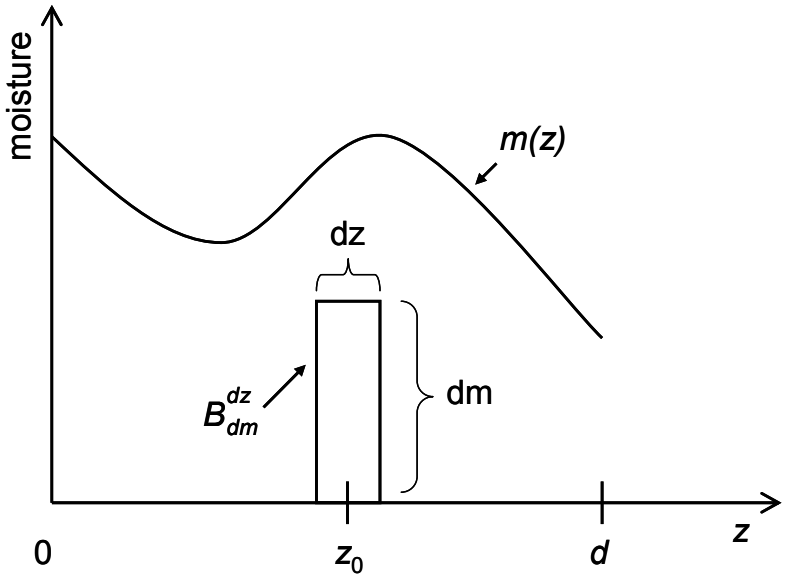

Figure 41. Schematic representation of the moisture depth profile function $m(z)$ *and the perturbation function* $B_{dm}^{dz}(z-z_0)$*. The sample extends from z = 0 to z = d.*

To get the formal definition for the depth sensitivity, one needs to define the test function. Let us introduce a boxcar-type test function $B_{dm}^{dz}(z)$ such that $B_{dm}^{dz}(z)=dm$ when $-(dz/2)<z<(dz/2)$, and $B_{dm}^{dz}(z)=0$ otherwise (see Figure 41). The function $B_{dm}^{dz}(z)$ will be referred to as the *perturbation function* hereafter. The *spectral depth sensitivity* is now defined as

$$\Delta_\lambda(z') = \lim_{dz,dm\to 0} \frac{\left\langle \delta D_\lambda, B_{dm}^{dz}(z-z') \right\rangle}{dzdm}. \qquad (19)$$

In other words, $\Delta_\lambda(z')$ tells the response of the diffuse reflection measurement D_λ to an infinitesimally small perturbation at depth z'. The result is normalised so that it tells the depth sensitivity for a perturbation having a unit thickness and unit moisture difference.

Again, if the analytical form of D_λ is not known, one may approximate the depth sensitivity numerically by

$$\Delta_\lambda(z') = \lim_{dz,dm\to 0} \frac{D_\lambda\left[m(z) + B_{dm}^{dz}(z-z')\right] - D_\lambda\left[m(z)\right]}{dzdm}. \qquad (20)$$

In the calculations of this thesis the function D_λ is approximated by Monte Carlo simulations. Hence the limit of Equation (20) has to be estimated numerically by making *dz* and *dm* sufficiently small.

Equations (19) and (20) give the depth sensitivity of the measurement at each wavelength. The generalisation to the application-specific depth sensitivity is straightforward. The moisture content may be predicted from the measured diffuse reflectance spectrum D_λ by developing a suitable calibration algorithm, denoted by the function C_m:

$$\begin{aligned} m_{pred} &= C_m\left[D_{\lambda_1}, D_{\lambda_2}, \ldots, D_{\lambda_j}\right] \\ &= \tilde{C}_m\left[m(z)\right] \end{aligned}, \qquad (21)$$

where the last row is justified by the fact that each D_{λ_k} is a functional of $m(z)$. The *application-specific depth sensitivity* is now defined as

$$\Delta_m^C(z') = \lim_{dz,dm\to 0} \frac{\left\langle \delta\tilde{C}_m, B_{dm}^{dz}(z-z')\right\rangle}{dzdm} \qquad (22)$$

and can be approximated numerically by

$$\Delta_m^C(z') = \lim_{dz,dm\to 0} \frac{\tilde{C}_m\left[m(z) + B_{dm}^{dz}(z-z')\right] - \tilde{C}_m\left[m(z)\right]}{dzdm}. \qquad (23)$$

The superscript C in $\Delta_m^C(z')$ denotes that the depth sensitivity is specific to the calibration function C_m, and the subscript m denotes that the depth sensitivity function is specific to the moisture depth profile $m(z)$.

Thus, generally speaking, the application-specific depth sensitivity is specific to the measurement method (illumination and collection geometries, wavelength region, etc.), but also to the analyte being considered and to the depth profile of that analyte. This is not only a mathematical curiosity but often occurs in practice, as will be seen in the next two sections.

Finally, the *analysis depth* of diffuse reflection measurement is defined to be the depth where the function $\Delta_m^C(z')$ has decreased to 1/*e* times its value at zero, i.e. to $e^{-1}\Delta_m^C(0)$. Similar definitions are often used with exponentially decaying functions. Although $\Delta_m^C(z')$ is typically only approximately exponentially decaying, the definition stated above is useful in the analysis of depth sensitivity results.

The definitions stated above may be generalised to the three-dimensional case, where the functional $D_\lambda = D_\lambda\left[m(x,y,z)\right]$. The perturbation function changes from a boxcar function to a "cube function", where the moisture content is different in a cube as compared to the surroundings. The depth sensitivity functions change into *spatial sensitivity functions*. The generalisations of the equations stated above are straightforward.

6.4.2 Depth sensitivity in base paper

This section deals with the depth sensitivity of the moisture measurement in the base paper of the trial runs. The definitions of application-specific depth sensitivity stated in Equations (18) and (23) will be used. The evaluation of the limit is done numerically in the fashion depicted schematically in Figure 42. A 15 µm layer of wet paper is positioned in the 75 µm thick base paper. The wet layer is moved through the base paper in 5 µm increments, starting from the top surface and ending on the bottom surface. A Monte Carlo simulation with the MSSM model using 5 million photons in the wavelength range 1250–2000 nm is performed at each position of the wet layer, and the height of the water absorption band is calculated. In this way, the moisture-specific depth sensitivity of the measurement is obtained.

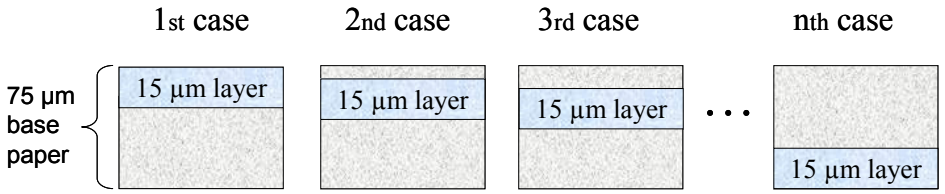

Figure 42. Moisture depth profiles used in the determination of the depth sensitivity of the moisture measurements in base paper.

The analysis was performed for four different cases. In the first case the moisture content of the base paper (hereafter called ambient moisture) is set to 4% and the moisture of the wet layer to 14%. In the second case the base paper moisture value is 14% and that of the wet layer 24%. The corresponding numbers in the third case are 24% and 34%, and in the fourth case 34% and 44%. The perturbation function $B_{dm}^{dz}(z)$ (see the preceding section) has height Δm = 10% and width Δz = 15 µm in these simulations (note that the infinitesimal dm and dz have been replaced by finite Δm and Δz). In principle, smaller values would lead to better estimates of the depth sensitivity. However, the calculation time increases rapidly when the perturbation is made smaller. The finite width Δz = 15 µm of the perturbation function means that the depth sensitivity can only be calculated in the interval $[\Delta z/2, d - \Delta z/2]$.

Figure 43 presents the results of the depth sensitivity analysis. The application-specific depth sensitivity $\Delta_m^C(z')$ as a function of the depth of the wet layer is shown. The depth is calculated as the distance from the surface of the paper (z = 0) to the middle of the wet layer (z = z_0), as depicted in Figure 41. The analysis depth is shown by the x-marks in Figure 43. The analysis depths and sensitivity to the bottom layer (i.e. the endpoint values of the curves in Figure 43) are also presented numerically in Table 3. The sensitivity to the bottom layer is also calculated in percentages of the peak sensitivity.

There are interesting differences between the graphs of different ambient moisture levels in Figure 43. First, the initial level is different, meaning that the response to moisture is different at different moisture levels. Second, the analysis depth becomes shallower with higher ambient moisture levels. Third,

the behaviour of the curves at the bottom layers of the paper is different. These differences show that the depth sensitivity is dependent on the ambient moisture level, and, generally speaking, on the moisture depth profile.

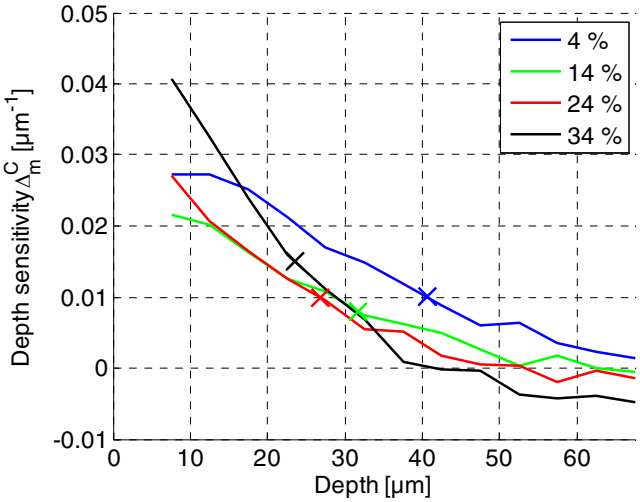

Figure 43. Depth sensitivity of the diffuse reflection moisture measurement $\Delta_m^C(z')$ *for the base paper at different moisture levels. The x-marks denote the analysis depths.*

Table 3. The analysis depth and sensitivity to the bottom layer of the paper at different ambient moisture levels. The sensitivity is also shown as percentages of the peak sensitivity.

Ambient moisture [%]	Analysis depth [µm]	Sensitivity to bottom layer [µm^{-1}]	Sensitivity to bottom layer [%]
4	40.6	0.0015	5.4
14	31.7	–0.0006	–2.8
24	26.8	–0.0014	–5.3
34	23.5	–0.0047	–11.5

The shallower analysis depth with increasing ambient moisture level is a result of two counteracting effects: the higher the ambient moisture of the paper, the higher the absorption coefficient and the lower the scattering coefficient (see Figure 28 and Figure 29). A higher absorption coefficient means shallower

analysis depths, but lower scattering coefficient works in the opposite way. The results indicate that the increase in the absorption coefficient is the more powerful effect.

With 4% ambient moisture, the measurement is only very slightly sensitive to the moisture in the bottom layers of the paper (see Table 3). Surprisingly, at higher ambient moisture levels the measurement shows an increasing negative sensitivity to moisture changes in the bottom layers of the paper. The reason behind this behaviour is probably the remarkable changes in the scattering coefficient: the scattering coefficient approximately halves when changing from a 34% to 44% moisture level (see Figure 29). Hence the amount of light reflected back from the wet 15 µm layer also roughly halves. This has approximately the same effect as removing a 7.5 µm layer of paper. Thus the decrease in the amount of back reflection from the bottom layers has a stronger effect than the increase of moisture content in these layers.

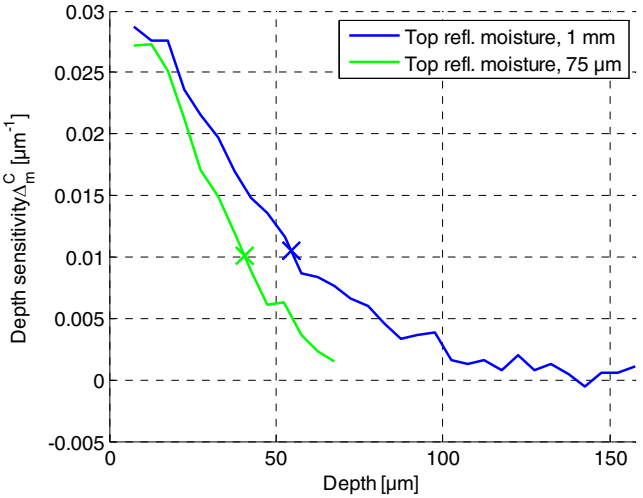

Figure 44. Depth sensitivity of the diffuse reflection moisture measurement in a 1 mm-thick base paper at 4% ambient moisture level (blue line). The depth sensitivity in a 75 µm-thick base paper is shown as the green line. The x-marks show the analysis depths.

Figure 44 shows the same depth sensitivity curve as the 4% curve in Figure 43, but now compared to a similar depth sensitivity curve calculated with a 1 mm-

thick base paper. The 1 mm base paper is infinitely thick from the point of view of the diffuse reflection measurement. The curves start from about the same level but there is increasing deviation when going deeper into the paper. The main reason for the deviation is that the layers beneath 75 µm in the 1 mm base paper act as a "back reflector". When the wet layer is situated on the top of the base paper, almost all collected photons have reflected back from the deeper than 15 µm layers of the base paper, and have travelled twice through the wet layer. The relative number of these photons only changes slightly, whether or not the "back reflector" is present. On the contrary, when the wet layer is situated in the bottom of the 75 µm base paper, the presence of the "back reflector" remarkably increases the fraction of photons travelling twice through the wet layer. The deviation is the largest at z = 67.5 µm, i.e. at the end of the 75 µm base paper sensitivity curve. Also, the analysis depths of the 1 mm and 75 µm base papers are different: 54 µm and 41 µm respectively.

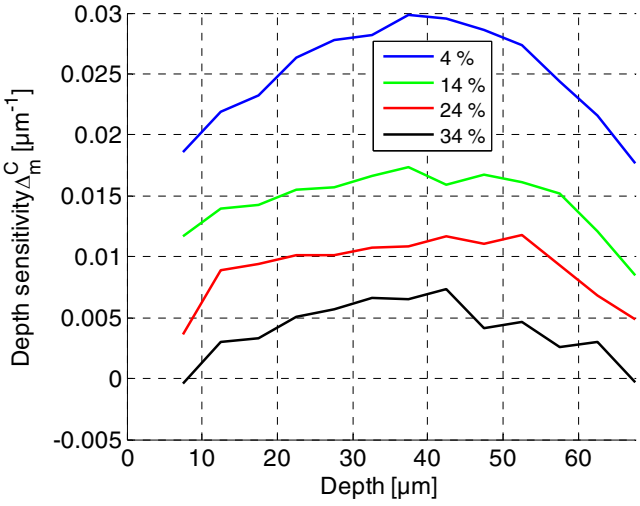

Figure 45. Depth sensitivity of the diffuse transmission moisture measurement in the base paper at different moisture levels.

Figure 45 shows the depth sensitivity of the diffuse transmission moisture measurement. Specifically, the results are calculated based on the top transmission, but the bottom transmission results are identical within the simulation accuracy. The transmission measurement is also dependent on the location of the wet layer inside the paper, but now the sensitivity curves are

symmetric. The sensitivity to the top and bottom surfaces is lower than to the middle layers of the paper. The reason for this behaviour is that the photon density is lower on the surfaces since the photons are escaping from the paper surfaces. As a consequence, the photons gather most of their optical path in the inner layers of the paper. If the wet layer is in the middle of the paper, the photons pass through it more often than if the wet layer is on the surface of the paper.

Another interesting feature that can be seen from Figure 45 is the change in the measurement response to water, as the ambient moisture level is changed. The sensitivity curves not only flatten, but the sensitivity to surface moisture changes goes to zero at the 34% ambient moisture level. The reason is analogous to that discussed above when analysing the reflection measurements. When the wet layer is located in either surface of the paper, the lower scattering coefficient of the wet layer constitutes a more straightforward route for photons to get out of the paper. Thus the wet surface layer decreases the mean optical path of the photons, which makes the water absorption band smaller. This is a more significant effect than the increase in water absorption band caused by the excess water in the wet layer.

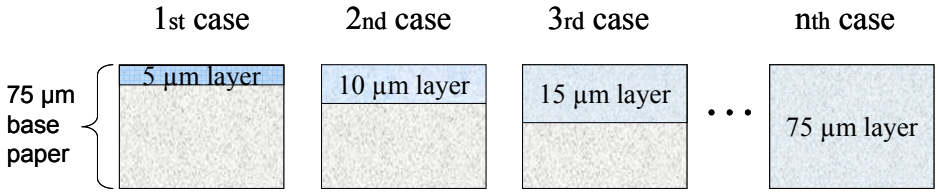

Figure 46. Moisture depth profiles used in the determination of the sensitivity to the distribution of water.

The depth sensitivity results presented above can be used in the analysis of the measurement results. However, in practice, the distribution of water often changes in a way schematically shown in Figure 46. The same amount of water is first put into a 5 µm layer, then to a 10 µm layer, then to a 15 µm layer, until the water is distributed uniformly through the whole paper. This kind of depth profile occurs, for example, when the surface of the paper is wetted and the depth profile is levelled via the processes of capillary suction and diffusion. The amount of water was chosen so that with the 15 µm wet layer the moisture of the

layer is 14%. This means the results are comparable to the 4% case in Figure 43 and Figure 45.

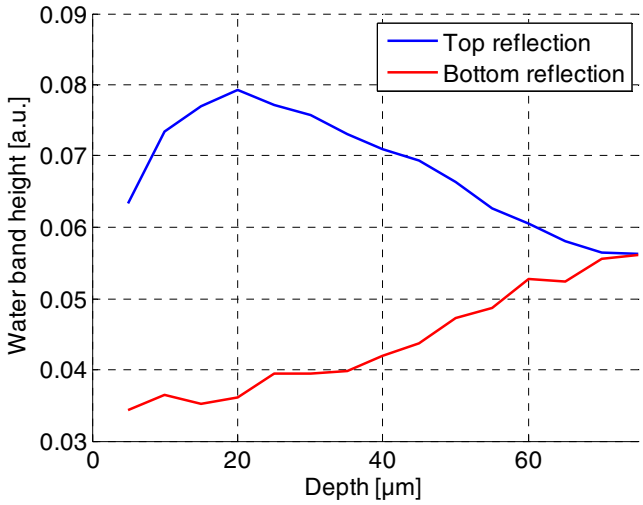

Figure 47. The sensitivity of reflection measurements to the distribution of water.

Monte Carlo simulations using the depth profiles represented in Figure 46 were performed to get the simulated water band heights. The resulting band heights of top and bottom reflection measurements are shown in Figure 47. They were not converted into depth sensitivity results for two reasons. First, the depth sensitivity definition of Equation (23) does not apply since the perturbation function is different. Second, this choice allows a direct comparison to measurement results because the measurements also give the water band height. The depth scale in Figure 47 tells the thickness of the wet layer.

Interestingly, the top reflection measurement sees the water most efficiently when it is located in a 20 µm thick layer. When the wet layer is thinner, the low scattering coefficient at high moisture levels diminishes the sensitivity of the reflection measurement to the moisture of the wet layer. On the other hand, when the wet layer is thicker than 20 µm, the lower sensitivity of the reflection measurement to deeper layers in the paper makes the moisture result lower. The bottom reflection moisture measurement sees the wet layer better and better when the moisture depth profile levels out.

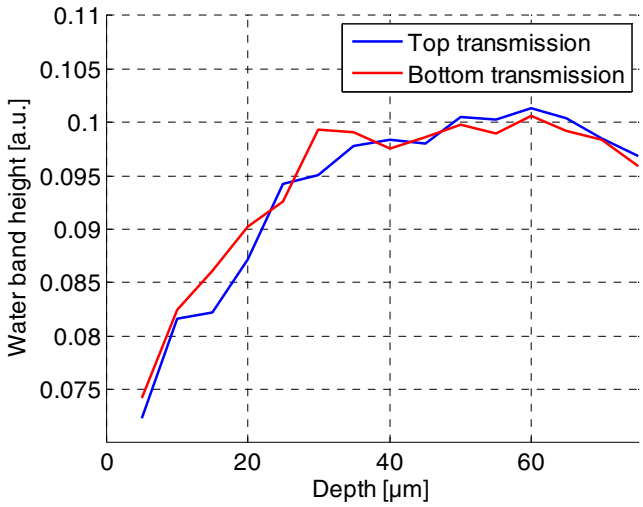

Figure 48. The sensitivity of transmission measurements to the distribution of water.

Figure 48 shows the sensitivity of transmission measurements to the distribution of water in the paper sample. The moisture depth profiles depicted in Figure 46 were again used in the Monte Carlo simulations. Ideally, the transmission moisture measurement should provide the mean moisture content of the whole sample. However, Figure 48 clearly shows that both the top and bottom transmission moisture measurements are sensitive to the distribution of the water inside the sample. Moreover, the two transmission moisture geometries give the same results within simulation accuracy, as expected. The distribution dependence is a result of two effects. First, the scattering coefficient decreases as a function of the moisture content of the paper. This shortens the optical paths of photons in a thin wet layer as compared to a thicker wet layer. Second, the depth sensitivity of transmission moisture measurements (see Figure 45) also affects the sensitivity to the distribution of water.

6.4.3 Depth sensitivity in coated paper

The analysis in the previous section concentrated on the depth sensitivity of diffuse reflection and transmission moisture measurements with the base paper as a sample. The coated paper is considered next. The existence of the coating layer

complicates the situation since its optical properties are different from those of the base paper, and they also change with moisture in a different way. The moisture depth profiles used in the analysis of the depth sensitivity for coated paper are shown in Figure 49. The only difference to the base paper consideration (Figure 42) is the existence of the coating layer, and that the first case has a moisture depth profile where the wet coating layer constitutes the wet layer.

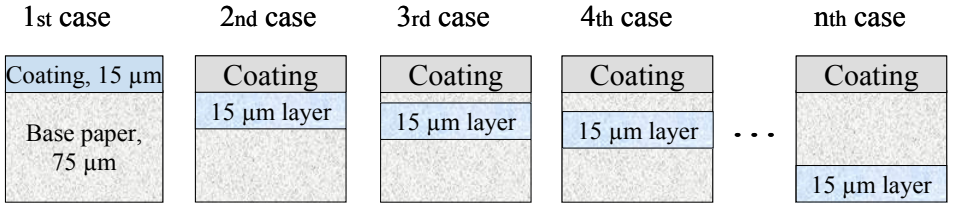

Figure 49. Moisture depth profiles used in the determination of the depth sensitivity for coated paper.

An ambient moisture level of 4% was used in the simulation, and the moisture content of the wet layer was 40%. These values were chosen because the resulting depth profiles resemble those expected to occur in the coating process.

The idea in the simulation is to move the same amount of water from the top to the bottom of the paper, and to calculate the response of the measurements to that. In the base paper, a wet layer with 40% moisture content is moved through the paper. In the case of the coating layer, it has to be considered what constitutes the same amount of water as compared to the wet layer in the base paper. This is achieved if the grammage (weight per square meter) of the water in the whole coated paper is the same for all cases of Figure 49.

The grammage of solid materials can be calculated for the coating layer (the first layer) by the following formula:

$$w_c^s = t_c \rho_c s_c \,, \tag{24}$$

where t_c is the thickness of the coating layer, ρ_c is the density of the coating colour, and s_c is the solids content of the coating colour at density ρ_c. The grammage of solid materials is calculated using the thickness, density and solids

content of the *wet* coating. The grammage of solid materials for the base paper can be calculated by a corresponding formula:

$$w_l^s = t_l \rho_b s_b , \tag{25}$$

where ρ_b is the density of the base paper and s_b its solids content at density ρ_b. The subscript l denotes the lth layer, so that t_l is the thickness of the base paper layer in question.

The grammage of solid materials can be converted into the grammage of water by the following formula:

$$w_l^w = w_l^s \frac{m_l}{1 - m_l} , \tag{26}$$

where m_l is the moisture content of the layer. Table 4 summarises the values for the densities and solids contents used in the calculations.

Table 4. The density and solids content values used in the water grammage calculations.

Layer	***Density [g/cm³]***	***Solids content [%]***
Coating layer	1.56	63
Base paper layer	0.69	96

Table 5 and Table 6 show how the formulas presented above are used to get the same grammage of moisture for the whole coated paper in two cases: the first case and the third case in Figure 49. The moisture content of the wet layer in the base paper (base paper layer 2 in Table 6) was selected to be 40% and the moisture content of the wet coating layer (coating layer in Table 5) was then adjusted so that the total moisture grammage for the whole coated paper was the same for both cases. This guarantees that exactly the same amount of water is

moved through the coated paper, which is required in adequate calculations of the depth sensitivity of the measurements.

Note that here the non-shrinking approximation has been used (see Section 6.2.1) in that the thicknesses of the coating layer or the base paper do not change as their moisture content is changed. This has two effects on the depth sensitivity results: First, the depth scale is not exact in the sense that, in practice, the base paper swells as its moisture is increased. Second, in the simulations it is assumed that the thickness of the coating layer is that of the wet coating layer, regardless of the moisture content. However, these effects do not change the general picture of the depth sensitivity since the swelling and shrinking are in the order of micrometers. On the other hand, if one would (and could) take these effects fully into account, the depth sensitivity results would be rather difficult to interpret since the position of the coating layer – base paper boundary, for example, would shift as the moisture depth profile changed.

Table 5. Calculation of water grammage corresponding to case 1 in Figure 49.

Layer	***Thickness [µm]***	***Moisture [%]***	***Water grammage [g/m^2]***
Coating layer	15	31.64	6.82
Base paper layer 1	25	4	0.69
Base paper layer 2	25	4	0.69
Base paper layer 3	25	4	0.69
Total	90	–	8.89

Table 6. Calculation of water grammage corresponding to case 3 in Figure 49.

Layer	***Thickness [µm]***	***Moisture [%]***	***Water grammage [g/m^2]***
Coating layer	15	4	0.61
Base paper layer 1	5	4	0.14
Base paper layer 2	15	40	6.62
Base paper layer 3	55	4	1.52
Total	90	–	8.89

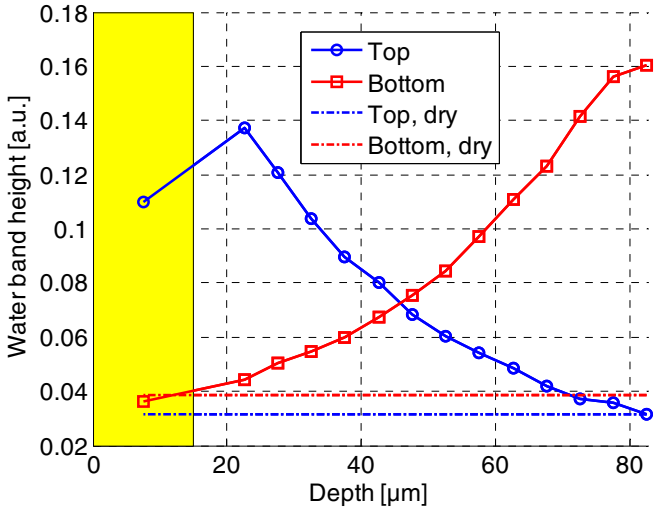

Figure 50. The depth sensitivity of the reflection moisture measurements for the coated paper. The dashed line is the moisture value of the dry paper for each measurement. The yellow region marks the coating layer.

Figure 50 shows the depth sensitivity of the top and bottom reflection moisture measurements for the coated paper. The results have not been converted into the depth sensitivity function as defined by Equation (23) since the presence of the coating layer complicates the use of the definition. The functional derivative (Equation (17)) may not exist at the boundary between the coating layer and the base paper. Thus the numerical approximation to the functional derivative (Equation (18)) is used, i.e. the water band height is shown as a function of the depth of the wet layer. Furthermore, the water band heights are directly comparable to the measurement results.

The bottom reflection moisture curve resembles the corresponding one in Figure 43. The depth sensitivity of the top reflection moisture behaves approximately as its bottom reflection counterpart, apart from the first depth point at 7.5 µm. This point corresponds to the situation where all excess water is situated in the coating layer (see Figure 49). The reason for this decrease in sensitivity is that the absorption coefficient of the coating colour is smaller than the absorption coefficient of the base paper at the 1940 nm water absorption band when comparing the moisture levels shown in Table 5 and Table 6. The result means

that the depth profiling results of the reflection moisture measurement of coated papers must be interpreted with care since the moisture content can even seem to increase when the water is penetrating the base paper from the coating layer.

The depth sensitivity of the transmission moisture measurements is shown in Figure 51. Here, the sensitivity difference between moisture in the coating layer and in the base paper is even greater than in the case of the reflection measurements. The reasons are the same as were discussed above for diffuse reflection measurement. In addition, the transmission measurements are also sensitive to the location of the moisture in the base paper. The measurement is most sensitive to the water located in the middle part of the paper and least sensitive to the surface water. This effect is due to the distribution of photons inside the paper, as was discussed in detail in Section 6.4.1.

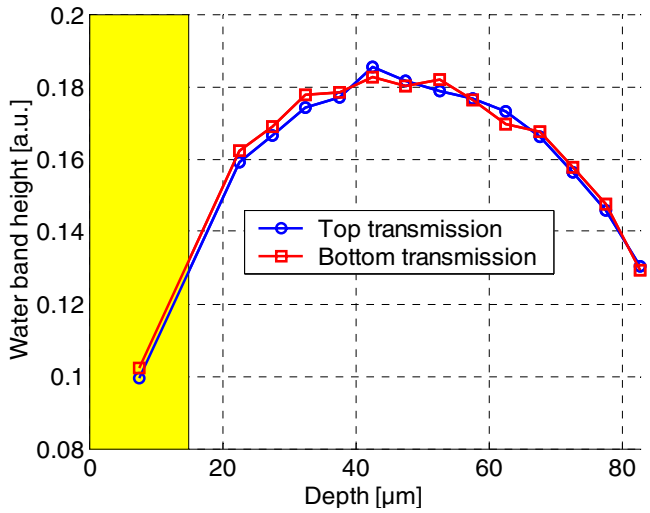

Figure 51. The depth sensitivity of the transmission moisture measurements for the coated paper. The yellow region marks the coating layer.

6.4.4 Conclusions

At this point, conclusions are drawn from the analysis of depth profiling properties performed in the two preceding sections. The conclusions will be helpful when analysing the measurement results in Chapter 7. The main

conclusion is that the depth sensitivities of the diffuse reflection and transmission moisture measurements depend on the moisture depth profile, on the thickness of the sample, and on whether there is a coating layer or not.

The conclusions of the theoretical analysis of the depth profiling properties with regard to the on-line measurement system in the coating machine can be summarised as follows:

- Top reflection moisture measurement:
    - The greatest part of the measurement signal comes from the topmost 40 micrometers of the coated paper; at the 40 µm depth the sensitivity to moisture has dropped to 50%.
    - The sensitivity of the measurement to moisture in the coating layer is considerably lower than to moisture in the base paper.
- Bottom reflection moisture measurement:
    - The greatest part of the measurement signal comes from the lowest 25 micrometers of the paper; at the 25 µm depth the sensitivity to moisture has dropped to 50%.
    - The measurement does not see the moisture in the coating layer.
- Transmission moisture measurements:
    - The measurement is considerably more sensitive to moisture in the base paper than in the coating layer.
    - The measurement signal is higher if the water is distributed uniformly in the paper, as compared to one thin, wet layer in base paper, or a wet coating layer, where the amount of water is the same as in the uniform case.
    - The measurement sees the water in the middle of the paper more efficiently than on the surface of the paper.

These properties of the measurement method make the interpretation of the depth profiling results challenging. However, the theoretical analysis results provide helpful tools for the analysis of the on-line measurement results. In the

next chapter the theoretical results are compared to measurements with the laboratory coater. There the moisture measurement results are considered together with the specular reflection measurement results, which gives a new perspective to the moisture depth profiling issue. Moreover, the comparison between measurements and simulations is continued in Chapter 7, where the results of the on-line measurements are presented.

7. Experimental results

The experimental results obtained with the measurement system are presented in this chapter. First, the results from the laboratory coater measurements are presented and analysed. Then the interpretation of the on-line measurement results is discussed, and the performance of the measurement system in on-line conditions is examined. Finally, the results of the on-line measurements performed during the coating trials are presented along with a thorough analysis of the water transport characteristics deduced from the measurement results.

7.1 Laboratory coater measurements

In this section the results of the measurements on the laboratory coater KCL-Saukko are presented. As discussed in Section 4.3, there were two types of trials: the coating trials and the water spraying trials.

The moisture, specular reflection and scattering results from a water spraying experiment on the laboratory coater are shown in Figure 52. The top and bottom reflection, and top and bottom transmission moisture signals are shown in Figure 52(a). The same curves are shown with a smaller time interval in Figure 52(c). The specular reflection (Figure 52(b)) and scattering (Figure 52(d)) are also shown with this smaller time interval.

The water is sprayed onto the paper at about t = 1.8 s. This shows up in the abrupt change in all measurement quantities, except in the bottom reflection moisture. The spraying forms a thin water film on the surface of the paper, but, according to the specular reflection measurement, the film has vanished at t = 2 s. At this time, most of the water has penetrated into the surface layer of the paper. The top reflection moisture goes up rapidly, but begins to decrease after the peak value at t = 2 s. On the other hand, the transmission moisture measurements continue to increase up to about t = 5 s, and the bottom reflection moisture even after that. Finally, the top and bottom reflection moisture measurements meet each other, meaning that the moisture depth profile in the paper has levelled out.

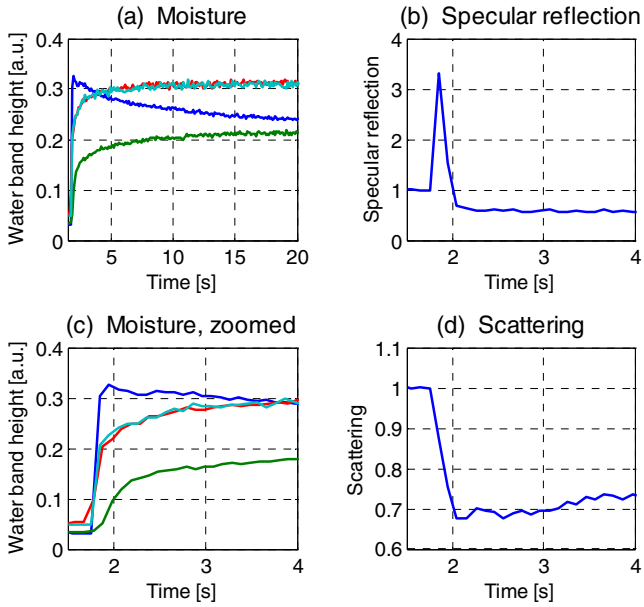

Figure 52. Moisture ((a) and (c)), specular reflection (b) and scattering (d) results from a water spraying experiment on the KCL-Saukko laboratory coater. In (a) and (c) the colours of the curves correspond to different measurement geometries: top reflection (blue line), bottom reflection (green line), top transmission (red line) and bottom transmission (cyan line).

In Figure 52(c) the bottom reflection moisture curve changes its slope at about t = 2.4 s, indicating a remarkable change in the absorption speed of water. This change is most probably a transition between capillary and diffusive water absorption processes. When the water film exists on top of the paper, the water goes into the pores of the paper, which is a very fast capillary process [39]. When all the water has penetrated the pores, the main water transport mechanism is either movement of water on the surface of the fibres or diffusive transport through the fibres. These are slower processes than the capillary transport [39].

It is very interesting to compare the measurement results to the theoretical analysis of the depth sensitivity of the measurements in Section 6.4.1. The simulated case that mostly resembles the water spraying experiment is the analysis of the response to the distribution of water (see Figure 47 for reflection measurements and Figure 48 for transmission measurements). Recall that in

these figures the same amount of water was first placed on a 5 µm surface layer of the paper, then a 10 µm layer, then a 15 µm layer, and so on, until at the last point the water was evenly distributed through the paper. This resembles the situation in the water spraying experiment, where the water first penetrates a thin surface layer of the paper, and then continues until the depth profile is flat.

The measurements in Figure 52 and the simulated results in Figure 47 and Figure 48 share the following common properties:

- The transmission moisture value is dependent on where the water is located; a thin wet layer gives about 25–30% lower transmission moisture value than the same amount of water distributed evenly through the paper.
- The top reflection moisture measurement is also sensitive to the distribution of water; the response is 30–50% bigger for water located mostly on the same side of the paper as the measurement, compared to an even distribution of water through the paper.
- The bottom reflection measurement does not see the water at the beginning of the spraying experiment, where the water is located as a thin film on top of the paper. In the simulations the bottom reflection measurement does not see a thin wet layer from the other side of the paper.
- Although the amount of water is different in the measurement (lots of water) and in the simulation (less water), the shapes of the curves resemble each other.

Figure 53 shows the moisture, specular reflection and scattering curves of a typical laboratory coater coating trial. The base paper was the same in the coating trial as in the on-line trials. The coat weight in this particular coating trial was 10.8 g/m^2. The coated area arrives at the measurement position at t = 1.2 s. Most of the curves have a sharp increase at this moment.

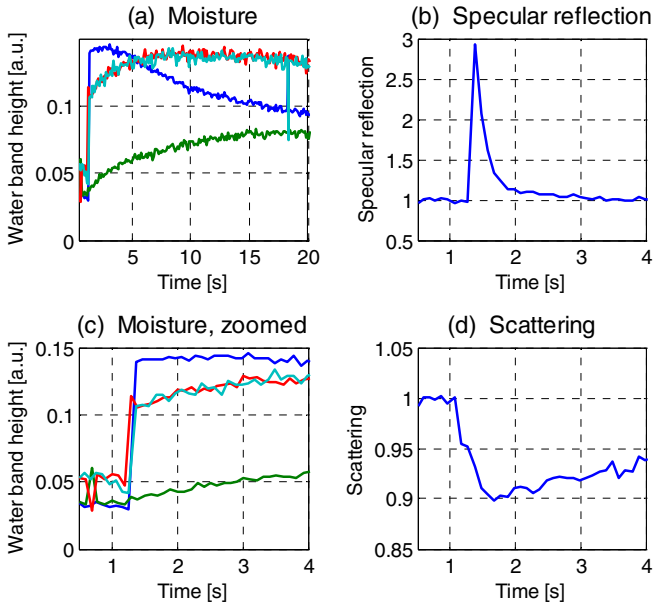

Figure 53. Moisture ((a) and (c)), specular reflection (b) and scattering (d) results from a coating trial on the KCL-Saukko laboratory coater. In (a) and (c) the colours of the curves correspond to different measurement geometries: top reflection (blue line), bottom reflection (green line), top transmission (red line) and bottom transmission (cyan line). The base paper was the same as used in the on-line trials, and the coat weight was 10.8 g/m^2.

Similar effects as in the water spraying experiment (Figure 52) are again observable in the moisture curves. After the arrival of the coated area in the measurement position, the transmission moisture increases until about t = 10 s, which is somewhat slower than in the case of the water spraying. This is because the water cannot move from the coating colour to the base paper as easily as from the water film. The increase in the bottom reflection moisture is also slower than in the water spraying trial. The top reflection moisture stays constant for a while, before it starts to decrease, again indicating slower water absorption in the base paper.

The specular reflection curve drops a little bit slower in Figure 53(b) than in the water spraying experiment (Figure 52(b)). This is again due to the water retention capability of the coating colour. However, there is no indication of the first critical concentration, but the specular reflection curve begins to decrease immediately

after the arrival of the coated area in the measurement position at t = 1.2 s. Instead, the second critical point is easily located at approximately t = 2 s, according to the scattering curve. It was very typical of the laboratory coater trials that the FCC was impossible to determine but the SCC was quite easy to find.

The laboratory measurements confirm some of the conclusions that were made based on the theoretical analysis in Section 6.4.4. The most important of these are that the bottom reflection moisture measurement does not see the moisture in the coating layer, that the transmission measurement is dependent on the distribution of the water, and that the top reflection measurement also sees the moisture on the top part of the base paper. The specular reflection and scattering measurements give information on the state of the coating layer. However, according to the laboratory coater measurements, the determination of the FCC position may be problematic. Instead, the SCC position is found more easily.

The most important conclusion from the laboratory coater measurements is that by analysing the moisture, specular reflection and scattering measurements together it is possible to get an overall picture of the water transport during the coating process. In addition, the measurement results should be analysed with the depth sensitivity properties of the measurements in mind to avoid misleading conclusions about the moisture transport in the coating process.

7.2 Interpretation of the on-line measurement results

As was discussed in Section 4.2.3, one can calculate the specular reflection, scattering with multiple geometries, moisture with multiple geometries, and water vapour band height from the measured spectra. Of these, the specular reflection, top reflection scattering and moisture results are the most important. In Figure 54 these quantities are shown in a typical trial point measurement. In this case the coat weight was 10.0 g/m^2 (measured in the laboratory afterwards), and the drying strategy was HLL.

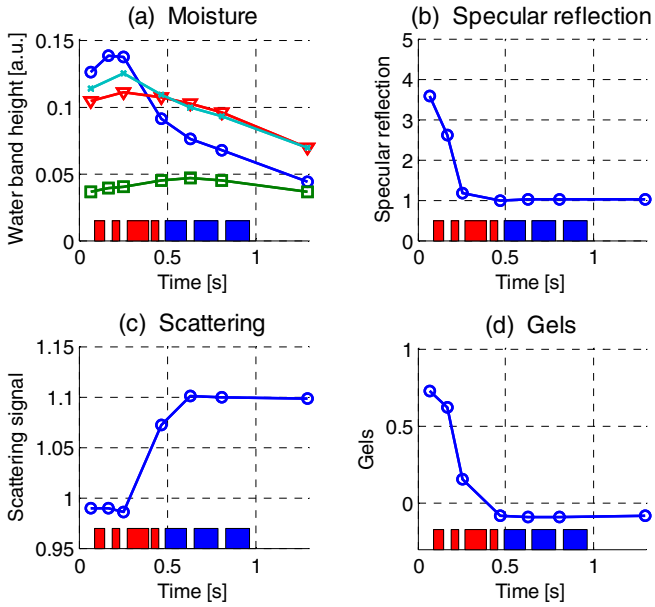

Figure 54. Typical results from the pilot runs. In (a), the blue line with circles is the top reflection moisture, the green line with squares is the bottom reflection moisture, the red line with triangles is the top transmission moisture and the cyan line with x-marks is the bottom transmission moisture. The small boxes just above the x-axes indicate the positions of the infrared dryers, whereas the wide boxes indicate the positions of the air foils. The red colour indicates that the dryer is functioning and the blue colour that the dryer is cold.

In Figure 54(a), moisture calculated from the top side diffuse reflection is shown with blue line and circles, moisture from bottom side reflection is the green line with squares, moisture from top-to-bottom transmission is the red line with triangles, and moisture from bottom-to-top transmission is the cyan line with x-marks. The small boxes indicate the positions of the infrared dryers, whereas the wide boxes indicate the positions of the air foils. The red colour indicates that the dryer is functioning and the blue colour that the dryer is cold.

In the HLL drying strategy the drying starts at about $t = 0.1$ s. Soon after that the top reflection moisture curve begins to drop steeply, but the transmission moisture curves not so steeply. This indicates that the paper begins to dry. Note the increase in the top reflection and transmission moisture curves after the first

measurement position. Based on the theoretical analysis in Chapter 6, this is an indication of the moisture transfer from the coating layer into the base paper. It is also possible that the moisture content of the paper actually begins to decrease slightly before the inflection point of the moisture curves at t = 0.3 s. The decrease would be obscured by the false increase in the moisture measurements. The bottom reflection moisture gradually increases to about t = 0.6 s. This shows the penetration of water into the base paper. In this case, however, it is difficult to say how deep into the base paper the water penetrates. At the last measurement position the top and bottom reflection moisture curves coalesce, which means the moisture depth profile is quite uniform at this point.

The specular reflection value in Figure 54(b) begins to decrease almost immediately, and it is very difficult to determine the position of the first critical point. On the other hand, the position of the second critical point is clearly seen in the specular reflection curve at t = 0.25 s. At this point the scattering curve (Figure 54(c)) also begins a very rapid increase, which also indicates the position of the SCC. The specular reflection and scattering curves give more information on the moisture content of the coating layer than the actual moisture measurements. However, this information is qualitative by nature. The moisture content of the coating layer is typically about 20% at the SCC [20].

The gels value as proposed by Alexander et al. [2] has also been calculated. It is defined as

$$Gels = 1 - \frac{S_n}{G_n}, \tag{27}$$

where S_n is the scattering signal and G_n the specular reflection signal at measurement position n. In some situations the gels value provides a better view of the phase of the coating immobilisation than the separate specular reflection and scattering results, and particularly emphasises small differences in low specular reflection values.

In analysing the measurement results it is important to take the conclusions of the theoretical analysis into account (see Section 6.4.4). The false increase in the top reflection moisture and transmission moisture measurements is a good example of this.

7.3 Performance of the measurement system on-line

In this section the signal-to-noise ratio (SNR) and comparability are analysed between different measurement positions of the measurement system in on-line conditions. The emphasis is on the moisture, specular reflection and scattering measurements.

7.3.1 Signal-to-noise ratios

The signal-to-noise ratios of the spectra collected during a reference measurement with the optical teflon sample are shown in Figure 55. The SNR estimates are based on about 230 spectra. The SNR results are only shown for top reflection and top transmission measurements since the bottom reflection and bottom transmission measurements are identical in geometry. In this section there is no differentiation between "top" and "bottom" reflection or "top" and "bottom" transmission since all results are equally valid for both "top" and "bottom" geometries. The SNR results in Figure 55 have been calculated in measurement position 1, but other positions are not remarkably different.

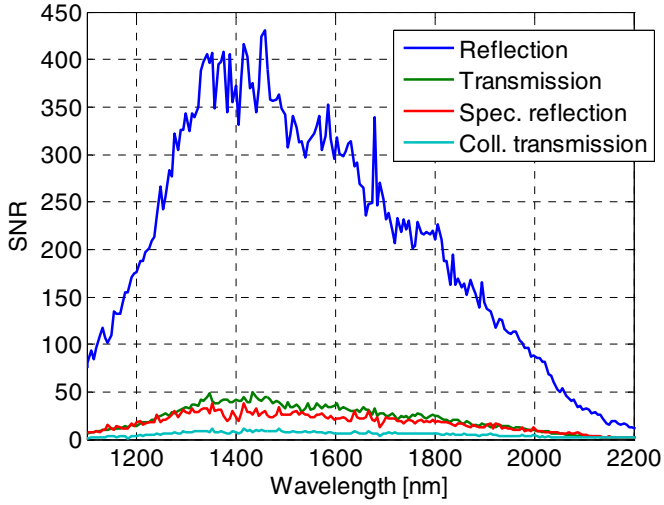

Figure 55. The signal-to-noise ratio of different types of measurement with the optical teflon sample.

The SNR of the reflection measurement is the best, and the SNR of the other measurements is quite poor. However, the optical teflon has lower transmission than the base paper, which means the transmission SNR estimate in Figure 55 is somewhat too low. Likewise, the specular reflection signal from the optical teflon is quite low. The dynamic range of the specular reflection measurement was selected so as to be able to measure the specular reflection of the base paper and the specular reflection of the wet coating layer, which may be about 20 times higher than that of the base paper. Thus it is natural that the SNR of the specular reflection measurement is quite low with diffuse samples.

Because the interest is in the performance of the measurement system when measuring paper, the SNR results have been recalculated with the base paper as a sample (Figure 56). The measurements were performed before a trial point, before the coating process was started. Figure 56(a) shows the SNR results with no signal corrections. They are remarkably poorer than those in Figure 55. The reason is the baseline variation in the spectra, which is most probably due to the distance variations in the measurement positions. Although an attempt was made in the design of the probes to make this effect as small as possible, it is still strong enough to make the SNR results poor. However, in the calculation of the moisture results a baseline correction is performed to the spectra (see Section 4.2.3). The SNR results were recalculated with the baseline corrected spectra (Figure 56(b)). In the calculation, the intensity spectra were first converted into absorbance spectra, the baseline correction was performed and the spectra were converted back to intensity spectra, after which the SNR could be calculated in the normal way. With this correction, the SNR results are more like those in Figure 55. Now the transmission SNR is also better. The collimated transmission SNR is still quite poor. This is because it uses the specular reflection collection optic, which is not, of course, optimised to collect the collimated transmission. In fact, the collimated transmission is more a “by-product” of the probe construction used. Still, the measurement results can be useful in some situations, as will be shown later.

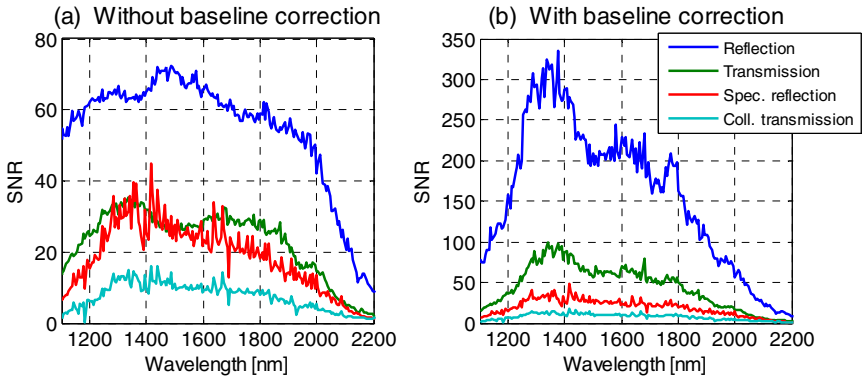

Figure 56. The signal-to-noise ratio for different types of measurement. The sample was the base paper measured on-line. In (a), the SNR is shown without any correction, and in (b), the SNR after applying the baseline correction.

Regardless of the sample or corrections used, the SNR is very poor at longer than 2000 nm wavelengths. This is partly due to the weak response of the MCT spectral camera at long wavelengths and partly due to the O–H groups absorption of quartz fibres. The absorption is significant even with the infrared-grade silica fibres used since the length of illumination and collection fibres were 12–15 meters.

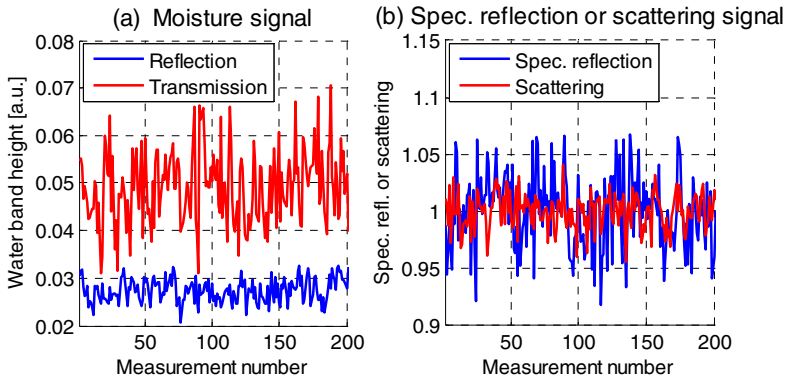

Figure 57. The variation in the moisture signals (a) and specular reflection and scattering signals (b) measured from the base paper on-line.

Figure 57(a) shows the calculated water band heights corresponding to the measurements used to calculate the SNR results in Figure 56, i.e. a base paper

sample measured on the coating machine. The result for the collimated transmission is quite noisy, and it is not shown to make the reflection and transmission moisture results more visible. Figure 57(b) shows the corresponding calculated values of specular reflection and scattering. As expected from the spectral SNR results (Figure 56), the variation in the transmission moisture signal is larger than that of the reflection moisture signal.

The signals in Figure 57 are quite noisy. However, the moisture, specular reflection and scattering values are not used as such. About 830 spectra are collected in a typical trial point measurement. The spectra are averaged prior to baseline correction, and calculation of the moisture, specular reflection and scattering results. Note that as the baseline correction and the average peak height calculation used are linear operations, the result is the same whether the spectra are averaged first and then the calculations are performed or vice versa. In Table 7 the resulting noise in the moisture, specular reflection and scattering measurements is estimated, based on the variations shown in Figure 56, and on the fact that typically about 800 measurements are averaged in the final result. The target accuracy has been set by considering the dynamic range of the calculated signals in on-line measurements. The target accuracy is achieved in all measurements except the collimated transmission. As was discussed earlier, the geometry of the collimated transmission is not at all optimised. Thus, the accuracy achieved is satisfactory and usable in some situations.

Table 7. The noise level in one measurement, and the estimated noise level in the final moisture, specular reflection and scattering results. The target accuracy is also shown.

Measurement geometry	***Noise in one measurement***	***Final noise***	***Target accuracy***
Reflection moisture	0.0025 a.u.	0.0001 a.u.	0.001 a.u.
Transmission moisture	0.0075 a.u.	0.0003 a.u.	0.001 a.u.
Coll. transmission moisture	0.0394 a.u.	0.0014 a.u.	0.001 a.u.
Specular reflection	0.0325	0.0011	0.01
Scattering	0.0157	0.0005	0.001

7.3.2 Comparability of measurement positions

The SNR analysis presented in the preceding section ensures that the calculated moisture, specular reflection and scattering results meet the accuracy requirements from the point of view of noise characteristics of the system. However, this does not guarantee the commensurability of the measurement positions. Typically, near-infrared instruments suffer from calibration transfer problems [115]. For example, the baseline corrected height of the water absorption band may be different when measured with two instruments having the same construction. In principle, this kind of problem should not exist in a measurement system employing a spectral camera. However, although the probes have exactly the same mechanical and optical construction (apart from the specular reflection probe in the zeroth position, which is an exception), there may still be some differences causing a different response to water, for example. Solutions to overcome these difficulties were discussed in Section 4.2.3. In this section the commensurability of the measurement positions is analysed based on the measurement results.

The best way to study the commensurability between measurement positions is to study the specular reflection, scattering and moisture results measured from base papers. These are shown for two base papers in Figure 58. The time between the two base paper measurements was about six hours. The reference measurement has been performed between the measurements, so the two measurements use a different reference.

The specular reflection measurement in Figure 58(a) has a peak-to-peak variability of about 0.05 specular reflection units. This is negligible since the dynamic range is from about one to about ten. In the case of specular reflection, the commensurability at high specular reflection levels also has to be considered. This has been done in Section 4.2.3, where a correction technique based on a glossy paper measurement was introduced. The scattering measurement in Figure 58(b) has a peak-to-peak variability of about 0.02 units. These errors may show up slightly in the trial point measurements since the dynamic range is approximately from 0.9 to 1.1. However, the overall accuracy is good enough to make reliable conclusions based on the measurements.

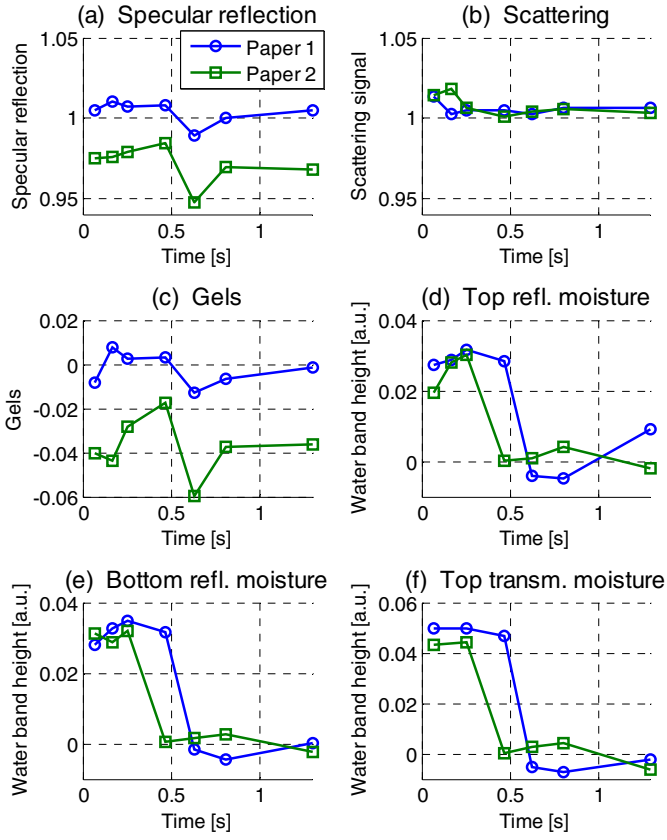

Figure 58. Specular reflection, scattering and moisture curves for two base papers. There are some minor differences in the specular reflection and scattering curves but the moisture graphs show more variation. This is due to the drying of the base paper.

In the moisture measurements in Figure 58 there is a clear drop in the results between t = 0.3 s and t = 0.6 s. This is not, however, a measurement error; it refers to the drying of the paper. The drying occurred because the air foils were still warm after the previous trial point, although they were not functioning during the base paper measurements. By comparing the top reflection and transmission, and the bottom reflection moisture measurements to each other, one can make conclusions about the commensurability of the measurement positions. Based on such analysis, the top reflection moisture (Figure 58(d)) has about 0.01 units error in the first measurement position with "Paper 2" and a

similar error in the last measurement position with “Paper 1”. It is difficult to pinpoint the source of these errors. Fortunately, the presence of the errors can be checked from the base paper measurements, which were performed just before the trial point measurements. If there is a clear systematic error like those discussed above, it usually stays the same in the trial point measurements. Thus erroneous measurements can be identified in most cases.

The behaviour of the moisture curves proves the reliability of the moisture measurement. The shape of the drying is smooth, the drying occurs in the same way in all measurement geometries, and the starting level is about the same for all base papers. The final level goes a little below zero in some cases. This is due to the baseline correction, which cannot estimate the exact shape of the baseline. This small offset does not affect the accuracy of the results; it merely shifts the curves a little bit downwards.

7.4 On-line measurement results

Some results from the trial runs on the KCL pilot coating machine are described in this section. The emphasis is on trials in which uncoated base paper was used. There are two reasons for this: first, uncoated base paper was used in the theoretical analysis of the measurement method (see Chapter 6), and, second, the coating process is also easier to understand when using uncoated base paper. Unless otherwise stated, the coatings have been applied onto the uncoated base paper. However, some comparisons between the measurement results obtained with different base papers are presented.

With the measurement system developed in this work it is possible to measure the specular reflection, scattering and qualitative moisture depth profile in several positions simultaneously. This allows the determination of the critical points and study of the water transport during the paper coating process. The variables in the coating trials were base paper type, coating colour type, coat weight and drying strategy. According to earlier research on paper coating [8, 20], the position of the critical points and the water transport are dependent on these variables. The results presented in this section explore these dependencies in detail.

7.4.1 Comparison between drying strategies

Because the two drying strategies used in the trial runs are completely different, one would expect different behaviour in the measurement results as well. Figure 59 compares two trial points with different drying strategies in terms of specular reflection, scattering and moisture measurements. The coat weight, type of base paper and other coating process variables were kept constant. The bottom transmission moisture is not shown since it is very similar to the top transmission moisture. The gels value has also been calculated [2]. There are clear differences between the two drying strategies: the specular reflection remains longer at a high level in the LLH strategy, the second critical point shifts remarkably, and the moisture curves behave in a different way.

The first critical concentration is difficult to determine from the specular reflection curve of the HLL strategy (Figure 59(a)), but in other respects the curve behaves as expected. The LLH strategy specular reflection curve is more complex. The first critical point can be located near $t = 0.2$ *s*, but after that the specular reflection level does not drop all the way down to value 1.0 as it should. Instead, there is a phase of slower decrease, which continues up to about $t = 0.8$ *s*. The gels curve emphasises this feature.

Another interesting feature is that according to the scattering curve (Figure 59(b)), the SCC occurs at about $t = 0.5$ *s*, which is in the middle of the slow decrease phase of the specular reflection. Clearly, the specular reflection curve does not behave according to the theory of Watanabe and Lepoutre [20]. Reasons for this discrepancy are discussed later.

The differences in the drying strategies show up clearly in the moisture curves, Figure 59(d)–(f). The drying is started at $t = 0.1$ s in the HLL strategy, and at $t = 0.5$ s in the LLH strategy. Before that, there is a slow increase in the top reflection and transmission moisture measurements, which is a result of transport of water from the coating layer to the base paper, as discussed above. However, because the bottom reflection moisture only increases slightly, it can be concluded that the water only goes to the surface layers of the base paper.

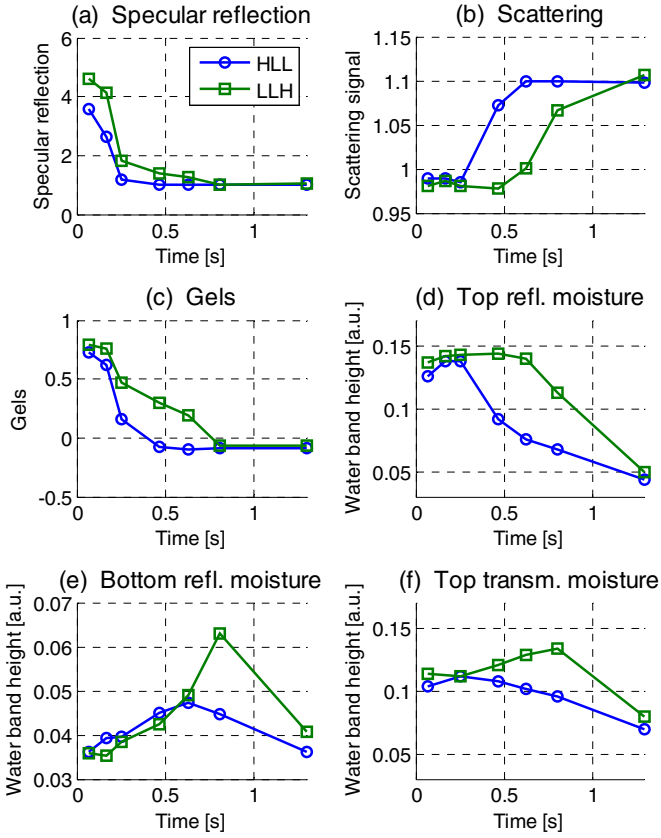

Figure 59. Specular reflection, scattering and moisture measurement results with two different drying strategies. A target coat weight of 10.0 g/m^2 has been applied on an uncoated base paper.

The top reflection moisture curves start to decrease soon after the drying starts. The HLL transmission moisture curve starts to decrease at the same point as the HLL top reflection moisture. The same is not true for the LLH strategy; the transmission curve continues to increase even up to t = 0.8 s, where the top reflection curve has already decreased considerably. At first glance there is a discrepancy between the two measurements. The reason for this behaviour can be revealed by comparing the measurement results to the depth sensitivity analysis for reflection measurement (Figure 50) and transmission measurement (Figure 51). The SCC point occurs at about t = 0.5 s, so there is about 20% of water left in the coating layer and some of the water has penetrated into the base

paper. When the drying is started it forces the water into deeper layers of the base paper. This can be concluded by considering the following changes in the measurements: the top reflection moisture decreases (cf. Figure 50) and the top transmission moisture increases (cf. Figure 51). In addition, the bottom reflection moisture increases remarkably from its initial value (cf. Figure 50) and the scattering curve increases sharply.

Because the transmission moisture curve continues to increase, the conclusion is that the paper does not dry remarkably before $t = 0.8$ s. Some drying takes place, of course, but it is impossible to determine from the measurement results exactly how much.

7.4.2 Effect of coat weight

Figure 60 shows the influence of different coat weights on the specular reflection, scattering and moisture measurements for trial points with the LLH strategy. According to Figure 60(a), the coat weight has a strong effect on the initial specular reflection level. This is somewhat surprising because the formation of specular reflection is a surface effect, and the initial value of specular reflection should not depend on the coat weight.

The first critical point cannot be unambiguously determined from the specular reflection curves, but the gels curves in Figure 60(c) show a rather clear FCC located approximately at $t = 0.2$ s. Interestingly, the FCC position does not change as a function of the coat weight, as it should according to the mass and heat transfer models [8, 100]. There is again a slow decrease phase of specular reflection after the FCC (cf. Figure 59), and the effect is the more pronounced the higher the coat weight. The SCC can again be easily detected. According to the mass and heat transfer models, the SCC should also change with coat weight, but only a slight change is observed.

The behaviour of top reflection and transmission moisture measurements are as expected: the initial moisture level is higher for higher coat weights, and after drying the moisture levels are the same since the end moisture target in all trial points was 5%. The bottom reflection moisture measurement, on the other hand, does not show any coat weight dependence. This means the transport of water into the base paper does not depend on coat weight. This is again in contradiction with the mass and heat transfer models.

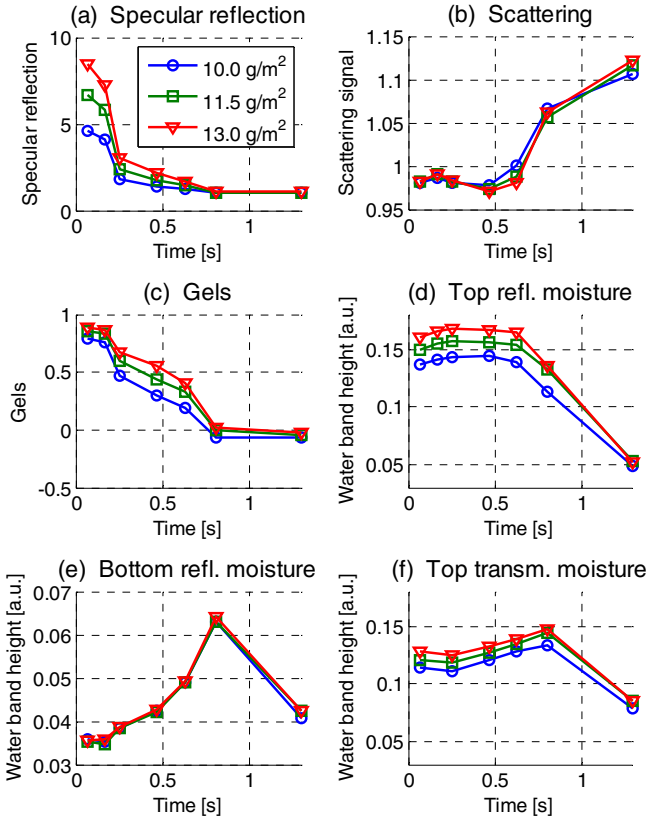

Figure 60. Influence of the coat weight on the specular reflection, scattering and moisture measurement results. The drying strategy is LLH.

It is also interesting to study the effects of different coat weights in different conditions to those above. Figure 61 shows the influence of different coat weights on the specular reflection, scattering and moisture measurements for three trial points, where the drying strategy is HLL. Another difference to Figure 60 is that there is no thickener in the coating colour. This means the water can move more easily from the coating layer to the base paper, i.e. the water retention capability of the coating colour is weaker. Because of these two differences, the specular reflection value drops more rapidly and the SCC occurs earlier than in Figure 60. The shape of the moisture measurements is different than in Figure 60, but of course they reflect the drying conditions. However, the coat weight changes do not cause remarkable changes in the measurement results, which confirms the earlier conclusion about the discrepancy with the mass and heat transfer theories.

There is an interesting feature in the measurement results of Figure 61 at $t = 0.6$ *s*, which roughly corresponds to the position where drying is stopped. The specular reflection value increases slightly, the scattering decreases and the bottom reflection moisture increases. The top reflection and top transmission moisture curves stay constant for a while in the middle of a long decrease. Combined, the results mean that at this particular point the water moves from the middle layer of the paper to the bottom layer, and to the coating. This is in concordance with an intuitive picture of the situation: during drying, the amount of water is highest somewhere in the middle of the paper since the drying takes place on the surfaces of the paper. When the drying is stopped, the water penetrates the dryer regions near the surface. In other words, the drying units maintain a non-uniform depth profile of moisture in the paper, which levels out after the drying is stopped and temperature has decreased.

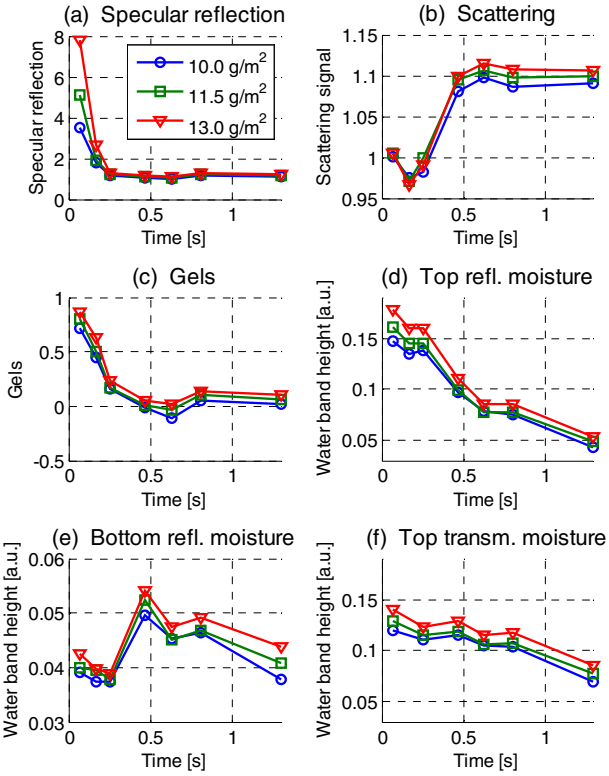

Figure 61. Specular reflection, scattering and moisture measurement results for trial points with the HLL strategy. The coating colour used has no thickener. Observe the interesting behaviour of the measurements at t = 0.6 s.

According to the bottom reflection and transmission moisture measurements, the amount of moisture in the paper in the last measurement position seems to be different for the different coat weights. The final top reflection moisture values, however, are quite similar. The target end moisture level is determined by an optical moisture gauge, which is based on the reflection principle. Thus there can be differences in the base paper moisture that the moisture gauge does not see.

7.4.3 Different coating colours

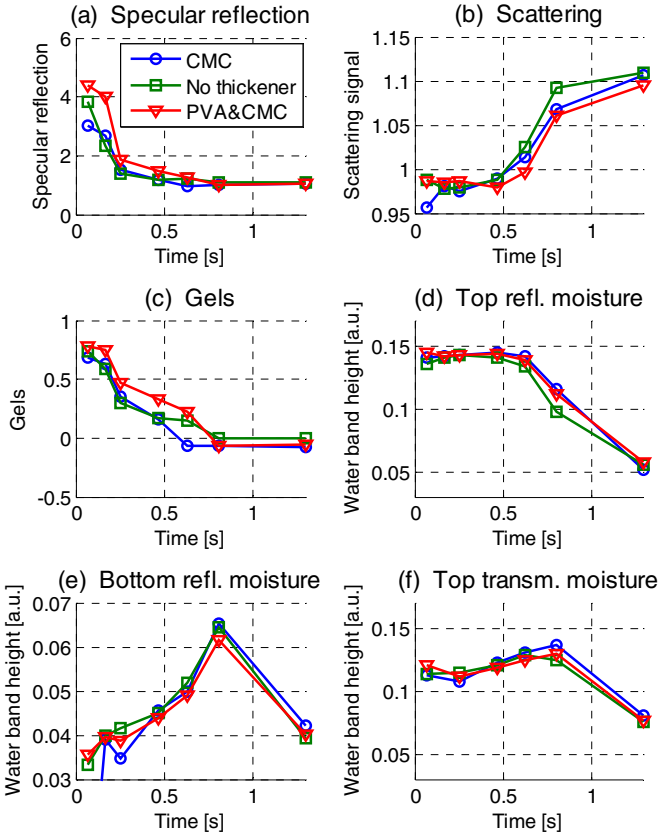

Figure 62. Specular reflection, scattering and moisture curves for different coating colours. The drying strategy is LLH and the target coat weight is 10 g/m^2.

According to the mass and heat transfer models [8, 100] and also to common sense, coating colours having different water retention characteristics should have

remarkable effects on the transport of water into the base paper, and thereby also on the location of the critical points. The measurement results of different coating colours do not fully support this, as can be seen from Figure 62. The target coat weight for all trial points was 10 g/m^2, and the drying strategy was LLH. The coating colour with no thickener has the highest water retention value (180 g/m^2), and the PVA & CMC coating colour the lowest (110 g/m^2) [57].

The location of the FCC is somewhat difficult to determine exactly, but it clearly shifts when the thickener is changed. On the other hand, the SCC only shifts slightly and the bottom reflection moisture measurement curves are almost identical. This is surprising since the water retention characteristics of the coating colours are very different. Hence after FCC the water transport does not behave as expected.

7.4.4 Different base papers

The measurement results presented in the previous sections are from trial points where uncoated base paper was used. Pre-coated base paper was also used in some trial points in the trial runs. There were two types of pre-coated paper: sized and impermeable (see Section 4.2.1). The sized paper had a thin layer of starch and hydrophobic agent, which makes the penetration of water slower than without this layer. The latex coated impermeable paper had a very low water penetration rate.

This section presents a comparison between the measurement results of trial points with uncoated, sized and impermeable base papers (hereafter called the uncoated case, sized case and impermeable case). In the comparisons, trial points with the same main variables (drying strategy, type of coating colour and coat weight) are compared. It should be borne in mind that the reference sample for specular reflection and scattering is the base paper, which has slightly different specular reflection and scattering properties depending on whether it has been pre-coated or not. Thus the specular reflection and scattering scales are not exactly the same when different base papers are used, but the difference is only about 10%.

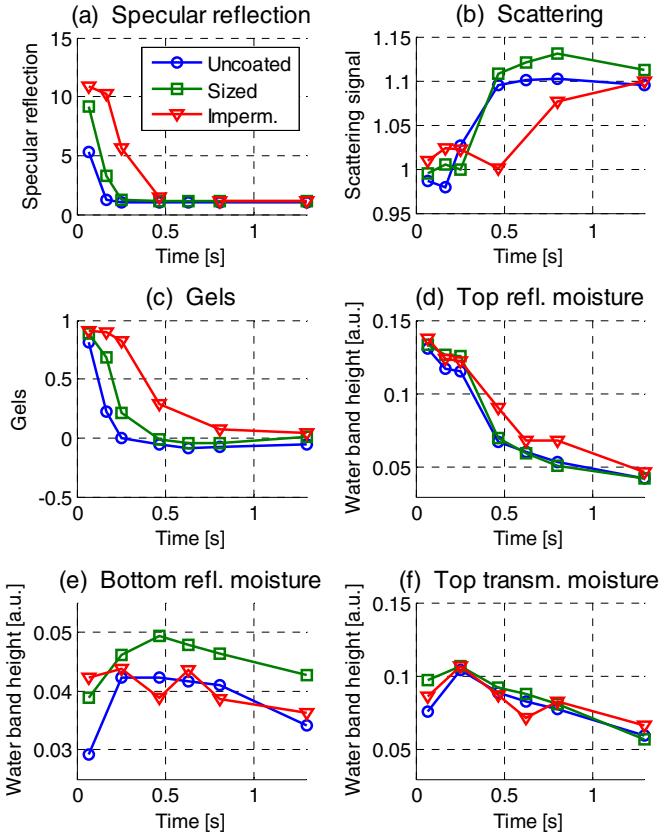

Figure 63. Comparison between trial points with different base papers. The thickener used was sodium carboxymethyl cellulose (CMC), the target coat weight was 9 g/m^2 and the drying strategy was HLL.

Figure 63 shows a comparison between three trial points with different base papers. In all trial points the drying strategy was HLL, the target coat weight was 9 g/m^2 and the coating colour included sodium carboxymethyl cellulose (CMC) as a thickener. There are differences in all curves of Figure 63. The differences are mostly related to the different water absorption properties of the base papers. The uncoated paper absorbs water quickly, the sized paper more slowly and the impermeable paper very slowly. These differences are very clearly seen in the specular reflection graphs in Figure 63(a). The initial specular reflection level is the highest, and specular reflection decrease is the slowest in the impermeable case. The FCC is evidently detectable only in the impermeable case, but the SCC

position can easily be found either in the specular reflection graphs or in the scattering graphs of Figure 63(b). The SCC shifts according to the water absorption properties of the base paper, and the immobilisation rate in general also obeys the absorption properties.

The fact that the base paper gets most water in the uncoated case and least water in the impermeable case is also seen in the top reflection moisture curves (Figure 63(d)) and especially in the bottom reflection moisture curves (Figure 63(e)). The different initial levels of the bottom reflection moisture are due to the different scattering properties of the base papers. The magnitude and rate of increase of the bottom reflection moisture are highest in the uncoated case and somewhat slower in the sized case. In the impermeable case there is hardly any increase. According to the simulation results and laboratory tests (Sections 6.4.3 and 7.1), this increase is directly related to the amount of water in the lower parts of the base paper. The top reflection moisture curve of the impermeable case stays above the other two after $t = 0.3$ s, indicating that there is more water in the top part of the coated paper. Because the scattering curve of the impermeable case is lower than that of the other two, the moisture content of the coating layer stays rather high up to the end of the coating section.

The main claim of this thesis is that it is possible to do semi-quantitative moisture depth profiling with the measurement system developed. Figure 63 is an excellent example of this. The following shows how information about the moisture depth profile and water transport during the coating process can be deduced from the measurements. The depth profiling is not quantitative since exact moisture contents at definite depths cannot be calculated. However, approximate moisture contents of the different parts of the coated paper can be deduced in many cases. This is why the depth profiling in this thesis is called semi-quantitative.

Uncoated base paper

Water is transported quickly from the coating layer into the base paper from the beginning up to $t = 0.3$ s, but no remarkable drying of the paper occurs. This can be deduced from the rapid specular reflection drop and increase in bottom reflection moisture, and from the fact that the top reflection or transmission moisture values do not decrease remarkably. At $t = 0.2$ s the moisture content of

the coating layer is about 20%, which is a typical value at the SCC. The moisture content of the bottom part of the base paper is about 5–6%, based on the fact that the moisture content of the base paper before coating is about 4%, and on the rise of the bottom reflection moisture. The moisture content in the top part of the base paper is higher since the whole coated paper has not dried remarkably, and the coating layer has lost about half of its initial moisture content.

After t = 0.3 s the paper begins to dry, but water transport to the top and middle parts of the base paper continues. This can be seen by observing that the top reflection moisture drops and the scattering rises remarkably, but the transmission moisture only decreases slowly. In addition, the bottom reflection moisture stays constant.

At t = 0.5 s the moisture content of the coating layer is about 5% because the scattering value is the same as in the end, where the whole paper has a moisture content of about 5%. According to the bottom reflection moisture, the moisture content in the bottom part of the base paper remains at 5–6%. According to the top reflection and transmission measurements, the moisture content in the top part of the base paper is roughly 10%. After t = 0.5 s the paper dries and eventually reaches the target end moisture level of 5%.

Sized base paper

There are no striking differences to the uncoated case other than that the SCC is reached about 0.1 seconds later and the transport of water into the base paper is a little bit slower.

Impermeable base paper

The bottom reflection moisture does not change remarkably from its initial value. Thus it can be concluded that the moisture content of the bottom part of the base paper stays at about 4% during the coating process. The SCC is reached at t = 0.5 s and the top reflection and transmission moisture values have already decreased remarkably. This suggests that even at this point there has not been significant water transport into the base paper. Thus it can be concluded that during the coating process, most of the water is contained in the coating layer,

which dries slowly. In the beginning the moisture content of the coating layer is about 40%, at t = 0.5 s it is about 20%, and in the end about 5%.

7.4.5 First and second critical concentrations

The results presented in the preceding section showed qualitatively that the first and second critical concentrations do not behave as was expected. In some cases the position of the FCC was ambiguous in the sense that there was no distinct, sudden drop in the specular reflection curve. Methods to calculate the position of the FCC and SCC from the measured data are presented in this section. Also, a quantity related to the amount of water penetrated into the base paper is proposed. After that, a summary and comparison of measurement results in terms of these quantities is presented.

According to Watanabe and Lepoutre [20], the first critical point occurs in a position where the specular reflection curve starts a rapid decrease. This definition is difficult to use in the measurement results of this thesis for three reasons: first, there are only a few measurement positions in the range where the FCC typically occurs; second, the FCC position seems often to occur before the first measurement position; and third, in some cases there is a smooth decrease but no sudden drop in the specular reflection curve.

To be able to quantitatively compare the trial points to each other, a calculation procedure for the FCC must be defined. Taking into account the restriction mentioned above, the following definition is adopted (G_n is the specular reflection signal and t_n the time at measurement position n).

The FCC is the position where the difference quotient of the specular reflection curve, defined by

$$G'_n = \frac{G_{n+1} - G_n}{t_{n+1} - t_n} \tag{28}$$

attains its minimum.

The above formula ensures that the FCC is found in a position where the steepest decrease in the specular reflection curve starts. It should be noted that the result is very approximate since the FCC can only be found in a measurement position. However, the measurement results do not allow a more precise FCC to be found.

Finding the SCC is easier and more precise since the scattering level before and after SCC can be found quite straightforwardly. The SCC position is defined as follows:

The SCC is the position where the interpolated scattering curve has increased by 20% from its minimum value. The 100% point is at the maximum of the SCC curve.

The 20% criterion is somewhat arbitrary. Lower values lead to SCC positions that are clearly located before the rapid increase of the scattering, as judged by visual inspection. On the other hand, higher values result in an SCC positioned in the middle of this rapid increase phase.

The bottom reflection moisture indicates the penetration of water into the base paper. In quantitative comparisons the amount of penetrating water would be interesting. The exact amount cannot be calculated from the measurement results of this thesis. Instead, the bottom reflection moisture rise (BRMR) is defined in the following way:

The BRMR value is the difference between the maximum bottom reflection moisture and the value of bottom reflection moisture at the first measurement position.

The BRMR value is proportional to the amount of water penetrated in the lower parts of the base paper.

Table 8 shows the comparisons presented in the preceding sections, but now in terms of the first and second critical points, and bottom reflection moisture rise. The table shows the trial run variable that changes between the particular trial points, and its “value”. The last column of the table gives the figure at which the corresponding specular reflection, scattering and bottom reflection moisture

curves can be found. It should be noted that an FCC position < 0.07 s actually means that the FCC was not found in the region of the measurement positions; it either occurs before the first measurement position or there is no clearly defined FCC.

Table 8. Comparisons between trial points in terms of first and second critical points and bottom reflection moisture rise.

Comparison variable	***Comparison variable value***	***FCC [s]***	***SCC [s]***	***BRMR [a.u.]***	***Figure reference***
Drying strategy	HLL	0.17	0.31	0.011	Figure 59
Drying strategy	LLH	0.17	0.64	0.027	Figure 59
Coat weight	10 g/m^2	0.17	0.64	0.027	Figure 60
Coat weight	11.5 g/m^2	0.17	0.67	0.028	Figure 60
Coat weight	13 g/m^2	0.17	0.67	0.028	Figure 60
Coating colour	CMC	0.17	0.55	n.a.	Figure 62
Coating colour	No thickener	< 0.07	0.54	0.031	Figure 62
Coating colour	PVA & CMC	0.17	0.65	0.026	Figure 62
Base paper	Uncoated	< 0.07	0.21	0.013	Figure 63
Base paper	Sized	< 0.07	0.30	0.010	Figure 63
Base paper	Impermeable	0.17	0.56	0.001	Figure 63

The drying strategy affects the SCC and BRMR but not the FCC. The starting of the drying forces the coating to reach the SCC; thus the SCC position reflects the position where the drying is started. The BRMR value shows that with the LLH strategy the base paper has more time to suck water from the coating layer.

There is a clear discrepancy between the heat and mass transfer theories [8, 100] and the coat weight comparison of Table 8. The mass transfer theories predict that the critical points and the amount of water penetrated in the base paper should change as a function of the coat weight. According to Table 8, there are practically no changes.

The coating colour comparison behaves more like that predicted by the mass transfer theories. It is also intuitively reasonable that the FCC and SCC occur

earlier, and the BRMR value is higher when there is no thickener in the coating colour. However, the differences are smaller than one would expect. The BRMR for CMC coating colour could not be deduced since there is a measurement error in the first measurement position (see Figure 62).

The base paper comparison shows clear differences in all quantities. The uncoated base paper absorbs water quite effectively, the sized water less effectively and the impermeable base paper hardly absorbs any water. The FCC shifts a little bit when the base paper is changed but the difference in the whole specular reflection curve is more pronounced (see Figure 63). The SCC shift is remarkable, as is the change in the BRMR value. The results suggest that the impermeable base paper does not absorb water practically at all during the coating process.

The general conclusion is that some of the changes in the trial point variables also cause changes in the position of the critical points. The most striking changes result from base paper and drying strategy changes. The thickener used in the coating colour, i.e. the water retention characteristics of the coating colour, only slightly affects the critical points and the BRMR. However, changing the coating colour has no effect on these quantities. Thus there is a considerable contradiction between the results of this thesis and the mass and heat transfer models.

7.5 Other quantities of interest

In the preceding sections the on-line measurement results were compared in terms of specular reflection, scattering and moisture measurements, and the top and bottom reflection and diffuse transmission moisture results were presented. In this section the calculation of some other interesting quantities from the on-line spectra is discussed. Some quantities are calculated with different geometries to those presented above, some use different absorption bands and some exploit the temperature dependence of the absorption bands. In other words, the following sections explore the possibilities enabled by the spectral, spatial and geometrical dimensions of the multi-measurement system.

7.5.1 Collimated transmission moisture

The measuring equipment also produces transmission measurements with collimated geometry. They result from the bottom phase illumination, where the bottom reflection probe is illuminating and the specular reflection probe is collecting. Figure 64 shows the result of a moisture calculation with this geometry. Compared to the diffuse transmission measurement (see Figure 59), the only difference is that the false increase is somewhat less pronounced in the collimated transmission result. The main reason for this similarity between the transmission measurements of different geometry is the high scattering coefficient and the thickness of the paper. The paper diffuses the illuminating radiation so well that there is practically no difference whether the measurement has been done with the collimated or diffuse geometry.

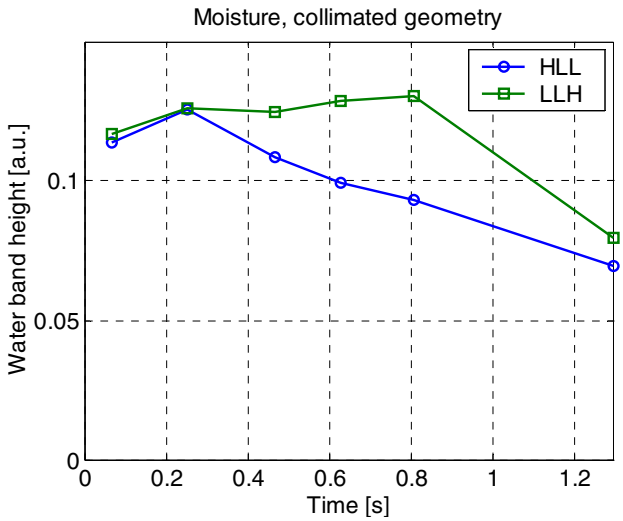

Figure 64. The moisture curves measured by the specular reflection probe, which means a transmission measurement with collimated geometry. There are no big differences with the diffuse transmission moisture measurement of Figure 59 (called top transmission moisture in the figure).

7.5.2 Moisture and other water bands

Figure 65 shows the moisture curves calculated using the 1440 nm water band. Because the shape of the moisture curves is rather similar to those in Figure 59,

one can conclude that moisture measurement is also possible using the 1440 nm water band. This is good news from an instrumental point of view since instruments capable of measuring the 1440 nm region are cheaper than those reaching the 1940 nm band. Going still lower in wavelength, the water absorption band at 970 nm could be measured with silicon-based devices, which are inexpensive but sensitive. However, the water absorption coefficient at 970 nm is so low that this band is not suitable for paper moisture measurement, except possibly at high moisture levels in heavy paper grades. The 1200 nm water band is also weak and does not provide any instrument cost benefits compared to the 1440 nm band.

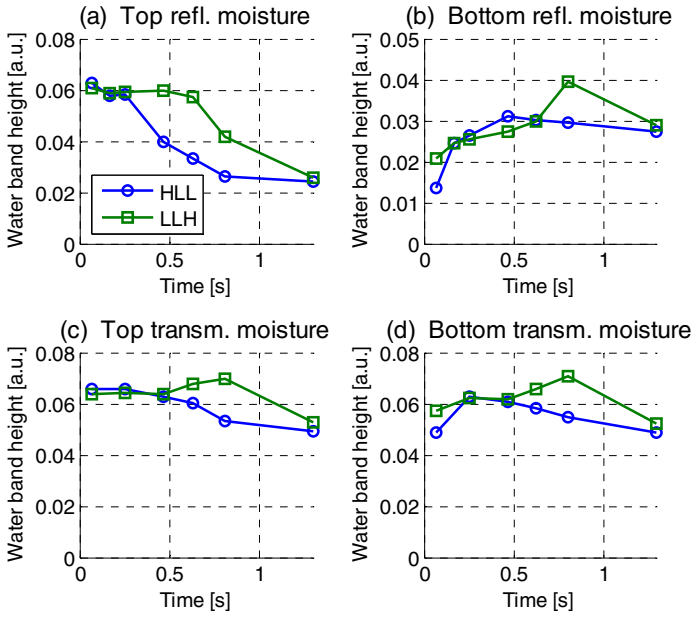

Figure 65. Moisture curves calculated using the 1440 nm absorption band of water. There are no striking differences to the results calculated with the 1940 water band (see Figure 59).

7.5.3 Scattering in all geometries

The measuring equipment also provides the scattering intensity in all the four geometries. Scattering calculated in all four measurement geometries is shown in Figure 66. The bottom reflection scattering mostly behaves like the top

reflection scattering. The biggest difference is that the bottom reflection scattering weighs the scattering changes in the base paper more than the top reflection scattering curve. Since the scattering changes occurring in the coating layer are so huge, they can still be observed rather clearly through the base paper, and they dominate the behaviour of the bottom reflection scattering.

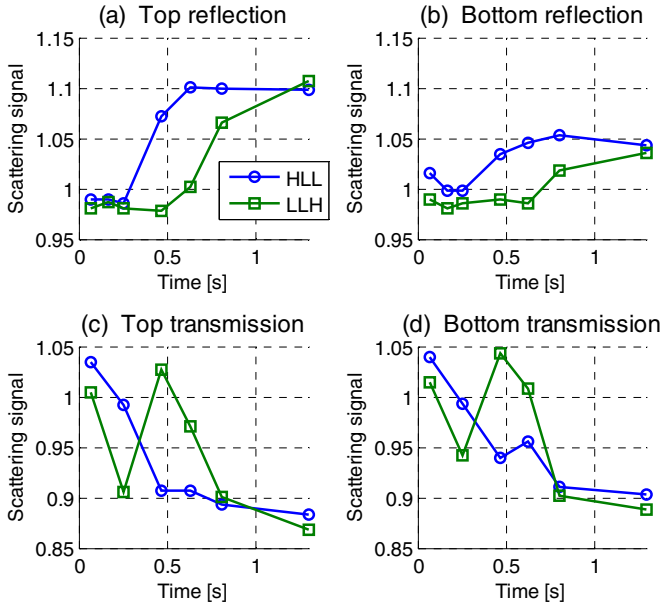

Figure 66. Scattering in all measurement geometries. The bottom reflection scattering behaves like its top reflection counterpart, but the transmission scattering curves are more difficult to interpret.

The transmission scattering curves (Figure 66(c) and (d)) of the HLL strategy can be rather easily explained. When the coating layer dries, its scattering coefficient begins to increase and less light can permeate through the coated paper. The LLH strategy is more difficult to explain. It decreases, increases and decreases again. At first, one would expect that the measurement result at t = 0.25 s is erroneous. However, both the top and bottom transmission measurements have the same feature, and the feature is also present in all LLH strategy measurement results made in the trial runs. This phenomenon is very difficult to explain. The only remarkable change in other measurement results at this point is the decrease in specular reflection, but how this could lead to the dip in the transmission results is not clear.

Figure 67 gives some new insight into the issue. It shows the same transmission scattering curves as in Figure 66, but now with collimated geometry. The dip vanishes and the transmission curve behaves as one would expect based on an intuitive picture of the phenomena in the sample. The unexpected dip may be related to the fact that the collimated and diffuse transmissions have a different behaviour as a function of the scattering coefficient. When the scattering coefficient is zero, the collimated transmission signal is at maximum but the diffuse transmission signal (with the on-line measurement geometry used in this work) is zero. When scattering coefficient is increased, the collimated transmission decreases but the diffuse transmission begins to increase. This increase continues up to the point where the penetration depth of the light becomes shallower than the thickness of the sample, after which the diffuse transmission begins to drop.

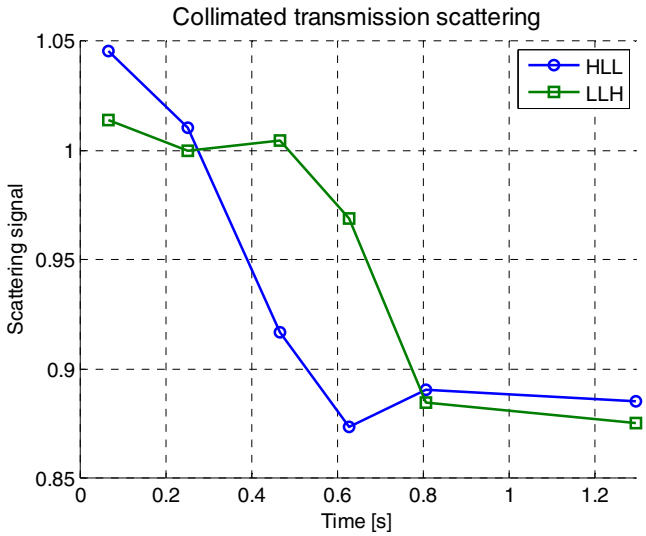

Figure 67. Scattering curves from the collimated transmission geometry. Note the difference to the transmission curves of Figure 66.

7.5.4 Temperature measurement by the infrared method

Temperature has the effect of shifting the water absorption bands [103]. Figure 68 shows the top reflection absorbance spectra around the water 1940 nm absorption band at different measurement positions. The spectra were collected

during a trial point where the temperature of the paper web varied from 26 °C to 75 °C. The moisture content of the paper is different in the spectra but the shift in the water absorption band is clearly visible.

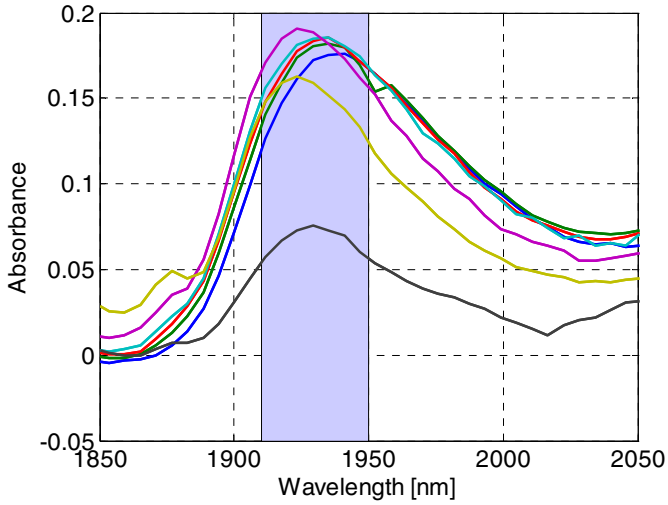

Figure 68. The top reflection absorbance spectra at different measurement positions. There is a clear shift in the water absorption band maximum. The region marked with blue is used for the determination of the water band maximum.

Based on the water absorption band shift, the temperature inside the paper can be predicted. This was done by estimating the position of the peak of the water absorption band. Since the spectral resolution of the spectral camera is only about 6 nanometres, a fourth-order polynomial was fitted to the spectra near the water absorption band. The region used in the polynomial fitting is shown with blue in Figure 68. The peak position of the polynomial was used as the water band peak position in the calculations. A calibration to predict the temperature of the paper based on the peak position was made using the temperature values measured with a hand-held thermometer during the trials. The hand-held thermometer measurement is based on the thermal emission from the paper; thus it gives the surface temperature of the paper.

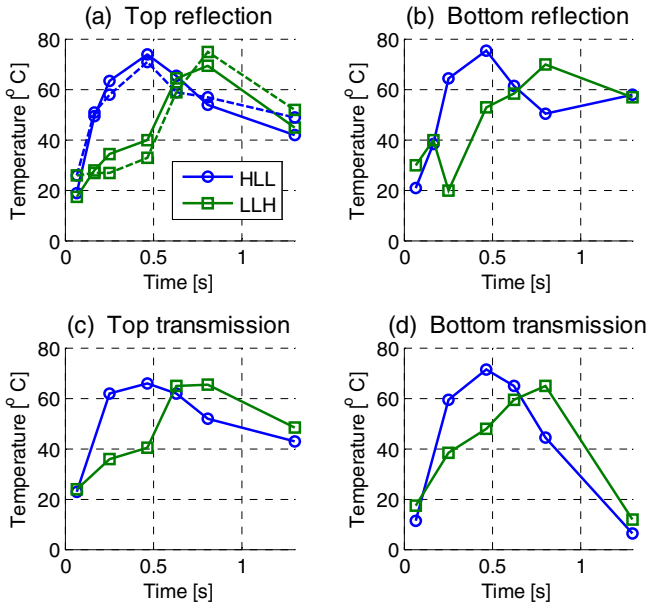

Figure 69. Temperature predicted from the position of the water band. In (a), the dotted lines with x-marks are measured temperature values.

In Figure 69 the predicted temperature values are shown in the top and bottom reflection, and top and bottom transmission geometries. In Figure 69(a) the dotted lines with x-marks are the thermometer temperature values.

The correspondence between the predicted and measured values is satisfactory. For the other geometries, there are no measured temperature values to compare. The general behaviour of the predicted temperatures makes sense but there are some peculiarities. These mainly come from the fact that the prediction is based on the shape of the water absorption band, which is not precise enough in the measured spectra. Small deviations in one wavelength may lead to 10-degree errors in the prediction. Thus the conclusion is that the measurement of temperature with this equipment is only indicative.

There is an interesting difference between the temperature measured with the actual thermometer and the temperature predicted from the spectra. The thermometer gives the surface temperature, whereas the spectrum-based temperature gives the mean temperature along the optical paths of the photons, i.e. the temperature inside the sample. Strictly speaking, it gives the temperature

of the water, but this is not expected to be very different from the temperature of the paper fibres. A near-infrared instrument specifically designed to measure the temperature based on the shift in the water absorbance band could provide interesting insight into the inside temperature of samples in many applications.

7.5.5 Water vapour

The measuring equipment also gives information on the water vapour content of the air between the measurement probes and the paper web. This is based on the mean height of the water vapour absorption bands in the wavelength region 1800–1850 nm, as described in Section 4.2.3. The water vapour results indicate the water vapour concentration at the measurement point, but how this is related to the water vapour concentration inside the driers, for example, is not clear. The surrounding mechanical constructions at each measurement position are different, which may also affect the air flow and the water vapour content. These obstructions make the results more qualitative than quantitative, but some conclusions can still be drawn based on them.

In principle, the measurement is sensitive to all water vapour, regardless of whether it is located within the paper or in the air between the probes and the paper. However, since the light path in the paper is fractions of a millimetre, and in the air about 300 mm, most of the water vapour signal comes from the air surrounding the paper. Thus the measurements qualitatively show how much water is evaporating, and also from which side of the paper (reflection measurements).

The water vapour measurement results for the drying strategy comparison are shown in Figure 70. Recall that the drying is started at t = 0.1 s in the HLL strategy and at t = 0.5 s in the LLH strategy. It takes some time for the water vapour content to go up after the drying is started. This time is needed to heat up the paper. Figure 69 shows the temperatures of the paper web measured with the hand-held thermometer along with the predicted temperature results. The water vapour and temperature curves are in good concordance with each other; high temperatures mean high water vapour concentrations, and low temperatures mean low water vapour concentrations. Of course, the exception to this rule is

that when there is little moisture left in the paper, the water vapour concentration cannot be high.

The evaporation seems to take place mainly from the top side of the paper in the HLL drying strategy. The situation is just the opposite in the LLH drying strategy. This is understandable because upon consulting Figure 59 the amount of moisture in the bottom layers of the base paper is clearly higher in the LLH drying strategy. Moreover, in Section 7.4.1 the conclusion was that starting the drying in the LLH strategy causes considerable water penetration into the deeper layers of the base paper. It also seems that the evaporation rate in the LLH strategy is higher than in the HLL strategy, but this may also be the result of the qualitative nature of the water vapour measurement.

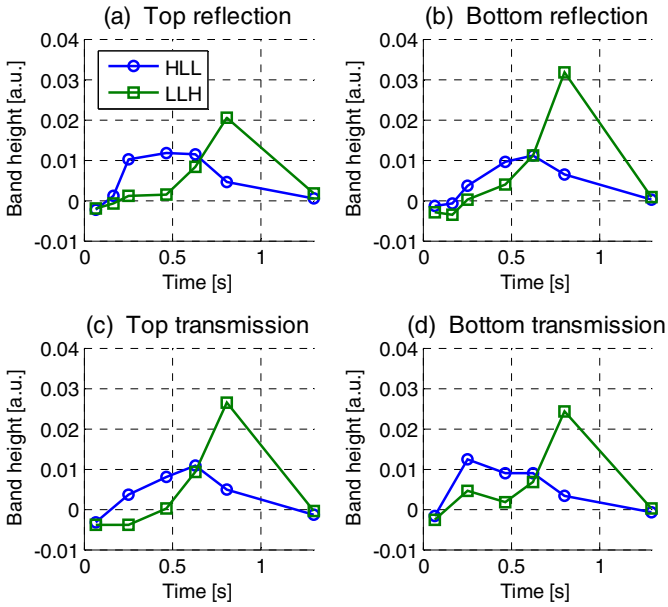

Figure 70. Water vapour band height measured from (a) top reflection, (b) bottom reflection, (c) top transmission and (d) bottom transmission. There is a great amount of water vapour in the LLH drying strategy, especially on the bottom side of the paper.

7.5.6 Wavelength dependence of specular reflection and scattering

The 1250–1300 nm spectral band was used to calculate the intensity values in all the specular reflection and scattering curves presented above. This selection was made to avoid absorption bands, to have a spectral region with good SNR, and to use a region where scattering changes would have the greatest effect.

Figure 71 shows the wavelength dependence of specular reflection and scattering. The wavelength regions at which the curves are calculated are indicated in the legend. There are regions from the extreme ends of the wavelength scale (1100–1150 nm and 2075–2125 nm) and regions with no absorption (1100–1150 nm, 1250–1350 nm and 1750–1800 nm). There are also regions at water (1915–1965 nm) and cellulose (2075–2125 nm) absorption bands.

Specular reflection has only slight dependence on wavelength. When going to longer wavelengths the curves are shifted a little bit upwards, but the position of the second critical point at about t = 0.6 s is not changed. The wavelength dependence of scattering is greater. The curves are shifted downwards when going from shorter to longer wavelengths. Because the scattering from the base paper is used as a reference, this shift indicates that the scattering from the coating layer is smaller at longer wavelengths. The same observation can be made from the measurements of the scattering coefficient of the coating colour presented earlier in Figure 35. The shape of the scattering curves is not changed as a function of wavelength. The 1915–1965 nm region is an exception, but it was intentionally chosen to be at the water absorption band. In addition to scattering changes, moisture changes also have an effect at this region. This makes the differences greater, but it also changes the shape of the curve.

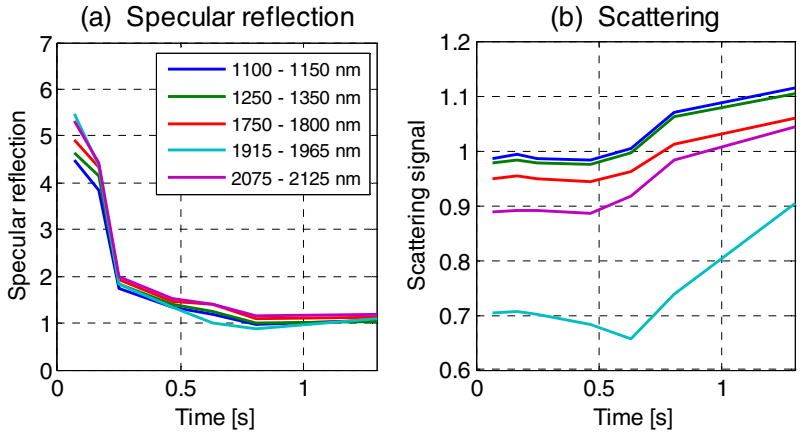

Figure 71. Wavelength dependence of specular reflection (a) and scattering (b). The regions used for calculating the specular reflection and scattering values are indicated in the legend. The results are from a trial point with a target coat weight 10 g/m^2 applied on an uncoated base paper and using the LLH drying strategy.

7.6 Comparison of simulation and measurement results

The properties of the measurement method were analysed in detail in Chapter 6, and in Section 7.4 the on-line measurement results were presented and analysed. Based on these, a qualitative understanding of how the water moves in the coated paper during the coating process was achieved. In this section the MSSM model is used to simulate the coating process, based on a sophisticated guess of the water depth profile at one particular trial point. The layer structure of the coated paper used in the simulations is depicted in Figure 72. The thickness of the coating layer corresponds to the calculated thickness at one particular trial point. The thicknesses of the two 7 µm base paper layers have been selected so that the penetration of water into the pores of the base paper can be simulated.

The assumed depth profiles of water are depicted in Figure 73. A trial point with the LLH drying strategy is simulated. At the first measurement position (the number of the measurement position is shown above the drawing) the water has already filled the pores of the first 7 µm base paper layer. The moisture content of the layer comes from the fact that the porosity of the base paper is 32%. In measurement positions 2 and 3 the water continues to penetrate the pores of the

base paper, but does not penetrate the bottom base paper layer until measurement position 4. At this point the coating reaches the second critical concentration, which means that at measurement point 5 the moisture content of the coating has decreased to 13%. Drying is started in between measurement points 4 and 5. In the depth profiles, the total grammage of moisture (see Section 6.4.3 to see how this is calculated) is not changed at measurement positions 1–4. After that, the grammage of moisture is gradually decreased until the end moisture target of 5% is achieved at measurement position 7.

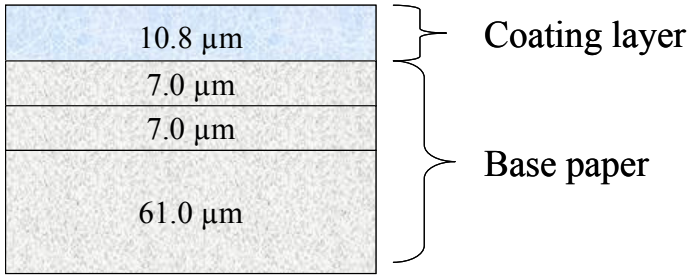

Figure 72. The layer structure of the coated paper used in the simulations.

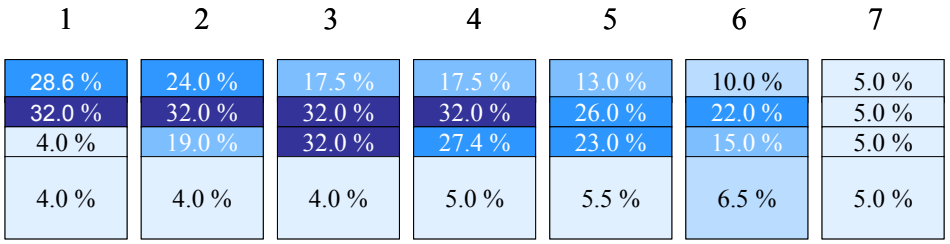

Figure 73. The assumed moisture depth profiles at the measurement positions. The numbers above the drawing denote the measurement positions and the shade of blue indicates the moisture content. The layer structure is depicted in Figure 72.

Figure 74 shows the simulated scattering and moisture results using the layer structure of Figure 72 and moisture depth profiles of Figure 73. The correspondence is good for top and bottom reflection moisture results. There is an offset between the simulated and measured results in the scattering results, but the shape of the curves is quite similar. There is no clear reason for this

offset, but it is probably related to the homogeneous approximation used in the simulation, and to the roughness of the paper. The simulated transmission moisture result increases too much compared to the measured one. However, the qualitative behaviour is similar: the false increase is there, and the end moisture value is about the same.

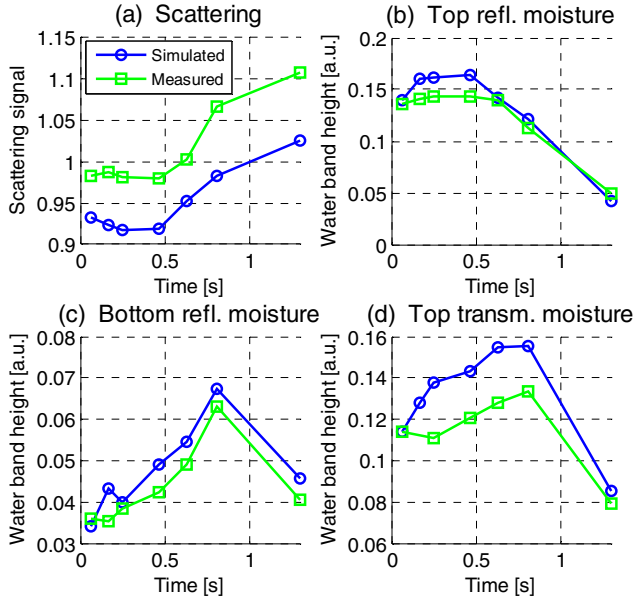

Figure 74. Comparison between the simulation and measurement results for scattering, and for moisture values with different geometries.

The good correspondence between the measured and simulated results confirms the understanding of the moisture transport phenomena occurring in the paper, and their relation to the measurement results. In the simulations above, the moisture depth profiles were guessed based on knowledge of the moisture transport characteristics in the coating process. A better way would be to calculate the moisture depth profiles based on mass transfer simulations of the coating process [8]. The calculated moisture depth profiles could then be put as input to the Monte Carlo coated paper model, which produces the simulated moisture measurement results. Comparing them to the actual measurements in a similar manner as was done above would give more insight into the coating process. However, this work is left for the future.

8. Discussion and conclusions

The main objective of this thesis was to show that multipoint moisture depth profiling of paper samples is possible using near-infrared spectroscopic methods. In the preceding chapters this goal has received a "three-dimensional" treatise: it has been shown that moisture depth profiling is possible technically, theoretically and in practice. The technical work involved the design and realisation of the measurement system and method; theoretically, an analysis of the measurement method and its depth-profiling properties was presented; and the practical application was the installation and use of the measurement system in the paper coating process. This chapter discusses the results of this thesis and draws conclusions from these three perspectives.

A fibre-optic multimeasurement system was designed and realised. The core of the system is the MCT spectra camera, which allows simultaneous measurement from over one hundred fibre input channels. The combination of the MCT camera with the double-chopping light source and the custom designed probes enabled multipoint multi-geometry on-line NIR spectroscopic measurements. This kind of multi-measurement system has not been presented earlier. Moreover, the laboratory and on-line measurement methods with the measurement system were also developed in this thesis. These involved, in particular, the use of reference measurements to standardise the probes and the data processing methods for the massive amount of data produced by the measurement system. The system and the measurement principle were tested extensively in the laboratory by installing it on a laboratory coater.

The multi-measurement system allows the measurement of top and bottom reflection, diffuse and collimated transmission, and specular reflection NIR spectra simultaneously in several measurement positions. In this work there were seven measurement positions. The system produces 42 different spectra about 10 times per second. Different quantities can be calculated and predicted from the spectra. This allows a very thorough analysis of industrial processes, but, on the other hand, requires some development work for data processing.

The emphasis in this thesis is on moisture depth profiling. The measurement system developed uses multiple geometries to extract information about the moisture depth profile in the coated paper. Laboratory experiments showed that

it is possible to follow the transport of water in a coated or uncoated paper in a semi-quantitative way.

Moisture depth profiling in the coating process is not the only application of the multi-measurement system. It could be used in other paper industry processes, including papermaking, calendering and printing. Other industries, such as the plastics industry, could also benefit. By developing new probes with different geometries and process interfaces, and by using different spectral cameras, the application range grows remarkably. Potential applications include, for example, blend homogeneity measurement and tablet quality inspection in the pharmaceutical industry, and fermentation process control in the biotechnical industry.

The second perspective on the subject of moisture depth profiling is theoretical. A Monte Carlo model to simulate the light behaviour in a coated paper was developed. The model was constructed so that the experimental geometries are mimicked as exactly as possible. The model needs the optical properties of the coating colour and base paper as a function of moisture as input parameters. Experimental and theoretical methods to determine these parameters were developed. Methods to make the simulation and measurement results directly comparable to each other were also developed.

A good correspondence was achieved between the simulated and the measured spectra. Based on this, the correspondence of the simulated and measured scattering and moisture results was also good. The results clearly show that it is possible to simulate the light and coated paper interaction in the different phases of the coating process. Simulations serve as a valuable tool in the explanation of the measurement results for two reasons. First, with simulations one can check different scenarios that are impossible to realise in practice. These checks help in understanding the complex phenomena occurring in the coating and in the paper, and their relationship to the measured signal. Second, with the knowledge from simulations the measurement results become more quantitative. For example, the effective probing depth for moisture measurements could be estimated in different situations.

The simulation model was used to analyse the depth-profiling properties of the multi-measurement method. The depth sensitivity was formally defined for the first time. The definition was used to get the analysis depth of the diffuse reflection measurement. Specifically, it was found that the analysis depth for

room-dry paper (moisture level 4%) is 40 µm, but is shallower in wetter papers. It was also shown that in wet papers the depth sensitivity to moisture in deep layers of the paper can even be negative. The depth sensitivities of diffuse reflection and transmission measurements were thoroughly explored. These results give new perspectives on the near-infrared measurement science. They also show that semi-quantitative moisture depth profiling is plausible with the multi-measurement system.

The third perspective on the moisture depth profiling is applications. The main application in this thesis is the paper coating process, but the results are also applicable to other paper industry processes, such as the drying section of paper mills. In the analysis of the on-line measurement data presented in Section 7.4 the emphasis was on showing the feasibility of the depth profiling measurements in on-line conditions. From the application point of view, it was shown that the water transport during the coating process does not fully obey the theories presented earlier in the literature [8, 100]. Specifically, the location of the critical points and the amount of water absorbed into the base paper did not change as expected when the coat weight and coating recipe were changed. Moreover, the determination of the first critical point was difficult at some trial points.

The determination of the first critical point is usually based on the specular reflection or gloss signal. Earlier studies and literature have proposed that after applying the coating the gloss level stays constant until some menisci start to form on the surface. At this point there should be an abrupt drop in the gloss measurement, which constitutes the first critical point [20]. However, in the measurements in this work the determination of the FCC was rather ambiguous in some cases. The specular reflection sometimes began to drop at the first measurement position, and continued to decrease all the way down to its final level. In such cases the detection of the FCC was impossible. In some other cases the specular reflection had a constant phase in the beginning, and a sharp decrease, so the FCC was detectable in principle. However, the specular reflection signal also showed some unexpected behaviour after the FCC in some cases.

The exact reasons for the peculiar behaviour of the specular reflection could not be found. However, some possible explanations are given by [25]:

- The amount of coating colour varies from place to place on the paper surface. This means different positions of the paper can reach the first critical point at different times, meaning that there is no well-defined FCC in the macroscopic scale. This easily leads to a smoothening of the specular reflection curve.
- The base paper gets pressed in the blade, and can expand after it. This can make the surface of the coated paper roughen after the blade. The wetting fibres of the paper can also swell, which gives the same effect. As the surface roughens, the specular reflection signal is scattered more angularly, leading to a decreasing specular reflection signal.

It is probable that both effects work together in reality. However, it is very difficult to judge which is the more important. Conclusions about these issues could only be drawn after performing more careful measurements. For example, measuring the angular and spatial dependence of the specular reflection signal would give a means to find the reasons for the specular reflection behaviour.

The position of the SCC was easily found in all measured trial points. The sharp increase in scattering intensity obeyed the theories of coating colour immobilisation [20]. Methods to find the FCC and SCC positions were developed. The FCC method gives only a very approximate position, whereas the detected SCC is quite accurate.

The position of the critical concentrations was studied as the drying strategy, coat weight, coating colour composition and base paper were changed. The critical concentrations did not change at all with different coat weights, and only slightly with different coating colours. This is in contrast to the mass and heat transfer simulations reported in the literature [8, 100]. On the other hand, the FCC and SCC positions changed significantly as the drying strategy or base paper was changed. Therefore, the conclusion is that the drying strategy and type of base paper determine the coating colour immobilisation characteristics, rather than coat weight or coating colour recipe.

With the multi-geometry moisture measurements it is possible to follow the behaviour of water in the coating process. The semi-quantitative moisture depth profile during the coating process can be inferred by analysing the specular reflection, scattering and moisture measurement results together. In particular,

the bottom reflection moisture measurement was important since it shows the penetration of water into the base paper. The top reflection and transmission moisture measurements indicate the drying of the paper, but not so much the water transport.

The same comparisons between different drying strategies, coat weights, coating colour compositions and base papers were also made in terms of the amount of water penetrated into the base paper. This was calculated from the bottom reflection moisture measurement. This analysis confirmed the results obtained with the critical concentrations. Water penetration into the base paper did not change with different coat weight, only slightly with different coating colours, and significantly with different drying strategies and base papers. The conclusion is that the penetration of water into the base paper is dictated more by the base paper properties and drying strategy than the water retention properties of the coating colour.

The amount of measurement data obtained during the trial runs is huge. That data is accompanied by the results from extensive laboratory measurements. During the work it became clear that it is not possible to analyse all the data in one thesis. There are many questions still waiting for answers. Thus the research should be continued, especially concentrating on the further analysis of the present results and performing more laboratory measurements. More trial runs would be appropriate after gaining more understanding of the coating process. Now that the measurement system and method has been developed and tested, and a wealth of data obtained, continuing projects can be built on a firm ground.

As a final conclusion, the goals set for this thesis have been reached, if not even exceeded. The issue of moisture depth profiling with NIR spectroscopy has received a thorough treatise from the technical, theoretical and application points of view. The results achieved in this thesis have many applications in the science of NIR analysis in laboratory and process environments. In particular, the combination of multi-measurement techniques with theoretical analysis of the measurement and application knowledge will lead to new measurement applications in the near future.

9. Summary

The main goal of this thesis was to develop a measurement system and method for moisture depth profiling of paper in the paper coating process. This also included the determination of the first and second critical points of the coating colour consolidation process.

The theory of near-infrared measurements was briefly reviewed and the near-infrared measurement techniques were summarised. A near-infrared spectroscopic method and measurement system for moisture depth profiling was developed. The measurement system is based on a fibre-optic light source and probes, and a hyperspectral imaging spectrograph. Measurement and data processing methods to produce specular reflection, diffuse reflection intensity (scattering) and moisture results with different geometries were also developed. The different geometries included diffuse reflection from both sides of the paper, and diffuse transmission and collimated transmission through the paper. All these measurements were performed at seven measurement points along the coating machine.

A theoretical model of the measurement method from the point of view of light behaviour in the sample was developed. The model was based on a Monte Carlo simulation of light scattering and absorption inside the paper, and considerations of the layer structure of the paper. The model needs the absorption and scattering coefficients as an input, as well as the anisotropy factor. These were determined for the base paper and the coating colour as a function of moisture by the inverse Monte Carlo method. The measurements needed by the inverse Monte Carlo model were performed with a double-beam spectrometer equipped with an integrating sphere.

The theoretical model of the measurement was applied to study the depth-profiling capabilities of the measurement method. A general definition for the depth sensitivity of near-infrared spectroscopic measurements was proposed. A theoretical analysis of the depth profiling capabilities of the system was presented, and confirmed qualitatively by laboratory tests. Based on these, the analysis depth of the reflection moisture measurement in uncoated paper was concluded to be about 40 µm. It was also shown that the analysis depth depends on the average moisture content of the paper, and that the inclusion of a coating

layer complicates the depth profiling. In particular, the response of reflection and transmission moisture measurements to water in the coating layer is weaker than to water in the base paper.

As the main application, the measurement system was installed on a pilot-scale paper coating machine. The feasibility of semi-quantitative moisture depth profiling during the coating process was shown, and the determination of the first and second critical points of the coating colour consolidation process was discussed. Detailed results from an extensive programme of trial runs were presented, along with discussion of the physics behind the measurements. It was found that the determination of the first critical point is ambiguous in some cases, but the second critical point was easily detected. The position of the critical points and the penetration of water into the base paper during the coating process were almost independent of coat weight and coating colour thickener. This is in contrast to simulations with the heat and mass transfer theories previously reported in the literature. Reasons for this discrepancy were discussed, and conclusions drawn.

The thesis showed that semi-quantitative moisture depth profiling is possible with near-infrared spectroscopic methods. From the technical point of view, the depth-profiling system and method was designed, developed and tested. From the theoretical point of view, the depth profiling properties of the system were analysed. And finally, it was shown that the system can be used in a demanding application in the paper coating process to get valuable information on the coating colour immobilisation and water transport.

References

[1] Li-Chan, E., Ismail, A., Sedman, J. & van de Voort, F. Vibrational Spectroscopy of Food and Food Products. In: Chalmers, J. & Griffiths, P. (Eds.) Handbook of Vibrational Spectroscopy, Vol. 5. Chichester, UK: John Wiley & Sons. 2002. Pp. 3629–3662.

[2] Alexander, C., Axelrod, S., Belotserkovsky, E., MacHattie, R. & Watson, D. New Insight into Coating Consolidation through an On-line Tool. Proceedings of the 10th Control Systems Conference. 2002. Pp. 303–307.

[3] Mäntylä, M., Paavola, A. & Tenhunen, J. Direct online coat weight measurement using multicomponent infrared spectroscopy. Appita Journal, Vol. 56. 2003. Pp. 181–183.

[4] Lang, D. Press optimization with a new, instantaneous wet end paper machine moisture profile measurement. TAPPI Paper Summit – Spring Technical and International Environmental Conference. 2004. Pp. 167–173.

[5] Hale, G. & Querry, M. Optical Constants of Water in the 200-nm to 200-µm Wavelength Region. Applied Optics, Vol. 12. 1973. Pp. 555–563.

[6] Peel, J. Paper Science and Paper Manufacture. Vancouver, Canada: Angus Wilde Publications. 1999. Pp. 88–98.

[7] Hashemi, S. & Murray Douglas, W. Moisture Nonuniformity in Drying Paper: Measurement and Relation to Process Parameters. Drying Technology, Vol. 21. 2003. Pp. 329–347.

[8] Timofeev, O., Pajari, H., Koskela, H., Paaso, J. & Kiiskinen, H. Drying of Coated Paper: Simulation and Pilot Experiments. Proceedings of the PAPTAC Annual Meeting. 2007.

[9] Williamson, M. Moisture profilers offer less streaks, higher coater speeds at blandin paper. Pulp and Paper, Vol. 75. 2001. Pp. 55–56.

[10] Peel, J. Paper Science and Paper Manufacture. Vancouver, Canada: Angus Wilde Publications. 1999. Chapter 11.

[11] Anderson, J. G. Measuring paper moisture. Measurement and Control, Vol. 25. 1992. Pp. 102–103, 105.

[12] Singh, D. A High Speed, High Temperature, On-line Moisture Sensing Technique for Paper Web Applications. Proceedings of the IEEE International Conference on Industrial Technology, Vol. 2. 2000. Pp. 24–25.

[13] Batchelor, W. Measurement of z-direction moisture transport and shrinkage in the drying of paper. Appita Journal, Vol. 57. 2004. Pp. 107–111, 127.

[14] Wu, Z., Batchelor, W. & Johnston, R. Development of an impedance method to measure the moisture content of a wet paper web. Appita Journal, Vol. 52. 1999. Pp. 425–428.

[15] Kuusela, R. Infrared moisture measurement of paper, board and pulp. PhD Thesis. Kuopio, Finland: University of Kuopio. 1990.

[16] Lang, D. Press optimization with a new, instantaneous wet end paper machine moisture profile measurement. 2004 TAPPI Paper Summit – Spring Technical and International Environmental Conference. 2004. Pp. 167–173.

[17] Putkinen, P., Nuyan, S. & Mäntylä, M. Instantaneous moisture measurement system solves wet end stability problems, optimises pressing, and improves runnability. Proceedings – PulPaper 2004 Conferences, Efficiency. 2004. Pp. 81–85.

[18] Dahlquist, J., Belotserkovsky, E., Lantz, K. & Sutcliffe, L. New on-line sensor for direct measurement of calcium carbonate and clay in paper coatings. APPITA Annual General Conference, Vol. 1. 1998. Pp. 247–252.

[19] Lehtinen, E. Introduction to pigment coating of paper. In: Papermaking Science and Technology, Vol. 11. Jyväskylä, Finland: Fapet Oy. 2000. Chapter 1.

[20] Watanabe, J. & Lepoutre, P. A mechanism for the consolidation of the structure of clay-latex coatings. Journal of Applied Polymer Science, Vol. 27. 1982. Pp. 4207–4219.

[21] Lepoutre, P. & Lord, D. Destabilized clay suspensions: Flow curves and dry film properties. Journal of Colloid and Interface Science, Vol. 134. 1990. Pp. 66–73.

[22] Huang, J. & Herbet, A. An infrared test method to measure coating immobilization. TAPPI Proceedings: 1996 Coating Conference. 1996. Pp. 149–157.

[23] Stanislawska, A. & Lepoutre, P. Consolidation of pigmented coatings: Development of porous structure. Tappi Journal, Vol. 79. 1996. Pp. 117–125.

[24] Willenbacher, N., Hanciogullari, H. & Radle, M. New laboratory test to characterize immobilization and dewatering of paper coating colors. Tappi Journal, Vol. 82. 1999. Pp. 167–174.

[25] Morin, V., Angogna, A., Sabater, J., Enri, D. & Le Nest, J. CTP develops a method of measuring gloss on-line. Paper Technology, Vol. 36. 1995. Pp. 37–45.

[26] MacHattie, R., Paavola, A. & Watson, D. Coating drying measurement and control reduces variations and costs. 59th Appita Annual Conference, Vol. 1. 2005. Pp. 53–58.

[27] Belotserkovsky, E. & MacHattie, R. Fiber optic gel point sensor for paper coating drying control and optimization. Proceedings of SPIE – The International Society for Optical Engineering, Vol. 4076. 2000. Pp. 244–251.

[28] Watson, D. & MacHattie, R. Coating consolidation measurement and control reduces variations and costs. Paper Technology, Vol. 46. 2005. Pp. 18–22.

[29] Åkerholm, J., Berg, C. & Kirstilä, V. An experimental evaluation of the governing moisture movement phenomena in the paper coating process. II. Experimental. Drying Technology, Vol. 19. 2001. Pp. 2407–2419.

[30] Heikkilä, P. & Rajala, P. Drying of paper coatings and drying equipment. In: Papermaking science and technology, Vol. 11. Helsinki, Finland: Fapet Oy. 2000. Chapter 26.

[31] Heikkilä, P. A study on the drying process of pigment coated paper webs. Ph. D. Thesis. Turku, Finland: Åbo Akademi University. 1992.

[32] Berg, C., Åkerholm, J. & Karlsson, M. An experimental evaluation of the governing moisture movement phenomena in the paper coating process. I. Theoretical aspects. Drying Technology, Vol. 19. 2001. Pp. 2389–2406.

[33] Kim, L., Pollock, M. et al. Reduction of back-trap mottle through optimization of the drying process for paper coatings, part I. Tappi Journal, Vol. 81. 1998. Pp. 153–164.

[34] Engström, G. & Rigdahl, M. Binder migration – Effect on printability and print quality. Literature review. Nordic Pulp & Paper Research Journal, Vol. 2. 1992. Pp. 55–74.

[35] Shen, Y., Bousfield, D. & van Heiningen, A. Linkage between coating absorption uniformity and print mottle. Journal of Pulp and Paper Science, Vol. 31. 2005. Pp. 105–108.

[36] Gupta, H. & Chatterjee, S. Parallel Diffusion of Moisture in Paper. Part 2: Transient conditions. Industrial and Engineering Chemistry Research, Vol. 42. 2003. Pp. 6593–6600.

[37] Leisen, J., Hojjatie, B., Coffin, D., Lavrykov, S., Ramarao, B. & Beckham H. Through-plane diffusion of moisture in paper detected by magnetic resonance imaging. Industrial and Engineering Chemistry Research, Vol. 41. 2002. Pp. 6555–6565.

[38] Fabritius, T. & Myllylä, R. Liquid sorption investigation of porous media by optical coherence tomography. Journal of Physics D: Applied Physics, Vol. 39. 2006. Pp. 4668–4672.

[39] Fabritius, T. Optical method for liquid sorption measurements in paper. PhD Thesis. Acta Universitatis Ouluensis, C 269. Oulu, Finland: University of Oulu. 2007.

[40] Berntsson, O., Burger, T., Folestad, S., Danielsson, L.-G., Kuhn, J. & Fricke, J. Effective sample size in diffuse reflectance near-IR spectrometry. Analytical Chemistry, Vol. 71. 1999. Pp. 617–623.

[41] Del Bianco, S., Martelli, F. & Zaccanti, G. Penetration depth of light re-emitted by a diffusive medium: theoretical and experimental investigation. Physics in Medicine and Biology, Vol. 47. 2002. Pp. 4131–4144.

[42] Boström, B. Measurement of dynamic moisture gradients in the z-direction. 7th International Conference on New Available Technologies, June 4–6. Stockholm, Sweden: SPCI. 2002. Pp. 60–62.

[43] Thennadil, S. & Martin, E. Empirical preprocessing methods and their impact on NIR calibrations: a simulation study. Journal of Chemometrics, Vol. 19. 2005. Pp. 77–89.

[44] Kubelka, P. & Munk, F. Ein Beitrag zur Optik der Farbanstriche. Zeitung von Technologie und Physik, Vol. 12. 1931. Pp. 593–601.

[45] Scallan, A. & Borch, J. An interpretation of paper reflectance based on morphology: General applicability. Tappi Journal, Vol. 57. 1974. Pp. 143–147.

[46] Griffiths, P. & Olinger, J. Continuum theories of diffuse reflection. In: Chalmers, J. & Griffiths, P. (Eds.) Handbook of Vibrational Spectroscopy, Vol. 2. Chichester, UK: John Wiley & Sons. 2002. Pp. 1125–1139.

[47] Dahm, D. & Dahm, K. Discontinuum theory of diffuse reflection. In: Chalmers, J. & Griffiths, P. (Eds.) Handbook of Vibrational Spectroscopy, Vol. 2. Chichester, UK: John Wiley & Sons. 2002. Pp. 1140–1153.

[48] Wang, L., Jacques, S. & Zheng, L. MCML – Monte Carlo modeling of photon transport in multi-layered tissues. Computer Methods and Programs in Biomedicine, Vol. 47. 1995. Pp. 131–146.

[49] Yaroslavsky, I., Yaroslavsky, A., Goldbach, T. & Schwarzmaier, H.-J. Inverse hybrid technique for determining the optical properties of turbid media from integrating-sphere measurements. Applied Optics, Vol. 35. 1996. Pp. 6797–6809.

[50] Green, K., Lamberg, L. & Lumme, K. Stochastic modeling of paper structure and Monte Carlo simulation of light scattering. Applied Optics, Vol. 39. 2000. Pp. 4669–4683.

[51] Wetzel, D., Eilert, A. & Sweat, J. Tunable filter and discrete filter near-infrared spectrometers. In: Chalmers, J. & Griffiths, P. (Eds.) Handbook of Vibrational Spectroscopy, Vol. 1. Chichester, UK: John Wiley & Sons. 2002. Pp. 437–452.

[52] Stark, E. Near-infrared array spectrometers. In: Chalmers, J. & Griffiths, P. (Eds.) Handbook of Vibrational Spectroscopy, Vol. 1. Chichester, UK: John Wiley & Sons. 2002. Pp. 393–422 .

[53] Lindström, H., Malinen, J. & Marbach, R. Performance Evaluation of Standard and Extended InGaAs Detector Array Spectrometers. The 11th International Conference on Near Infrared Spectroscopy, April 6–11, Cordoba, Spain. 2003. Pp. 99–104.

[54] Tate, J., Chauvel, P., Guenard, R. & Harner, R. Process monitoring by mid- and near-infrared Fourier transform spectroscopy. Handbook of Vibrational Spectroscopy, Vol. 4. Chichester, UK: John Wiley & Sons. 2002. Pp. 2737–2769.

[55] Aikio, M. Hyperspectral prism-grating-prism imaging spectrograph. PhD Thesis. VTT Publications 435. Espoo, Finland: VTT. 2001.

[56] Paaso, J., Lehtonen, P., Suopajärvi, P., Tenhunen, J., Pajari, H., Koskela, H. & Forsström, U. Measurement system for monitoring the paper coating process. 22nd PTS Coating Symposium. Baden-Baden, 20–23 Sep. 2005. Munich, Germany: PTS. 2005.

[57] Paaso, J., Lehtonen, P., Suopajärvi, P., Tenhunen, J., Pajari, H., Koskela, H. & Forsström, U. Measurement system for monitoring the paper coating process.

Wochenblatt für Papierfabrikation: Professional Papermaking, Vol. 1. 2006. Pp. 39–43.

[58] Kurki, L., Paaso, J., Teppola, P. & Marbach, R. Designing good sampling optics – Estimation of optical scattering and absorption properties of real process samples. Journal of Chemometrics. 2007. Submitted.

[59] DeThomas, F. & Brimmer, P. Monochromators for near-infrared spectroscopy. In: Chalmers, J. & Griffiths, P. (Eds.) Handbook of Vibrational Spectroscopy, Vol. 1. Chichester, UK: John Wiley & Sons. 2002. Pp. 383–392.

[60] Weyer, L. & Lo, S.-C. Spectra – structure correlations in the near-infrared. In: Chalmers, J. & Griffiths, P. (Eds.) Handbook of Vibrational Spectroscopy, Vol. 3. Chichester, UK: John Wiley & Sons. 2002. Pp. 1817–1837.

[61] Malinen, J., Känsäkoski, M., Rikola, R. & Eddison, C. LED-based NIR spectrometer module for hand-held and process analyser applications. Sensors and Actuators B Chemical, Vol. 51. 1998. Pp. 220–226.

[62] Chalmers, J. & Griffiths, P. (Eds.) Handbook of Vibrational Spectroscopy, Vol. 1. Chichester, UK: John Wiley & Sons. 2002.

[63] Känsäkoski, M., Kemppainen, A., Suhonen, J., Malinen, J., Rantanen, J., Yliruusi, J., Luostarinen, K. & Nauha, P. Integrated multichannel detector analysers at process control. Near Infrared Spectroscopy: Proceedings of the 11th International Conference, Cordoba, Spain. NIR Publications. 2004. Pp. 121–126.

[64] Mie, G. Beiträge zur Optik trüber Medien, speziell kolloidaler Metallösungen. Annales der Physik, Vol. 308. 1908. Pp. 377–445.

[65] van de Hulst, H. Light scattering by small particles. New York: Dover Publications. 1981. Chapter 9.

[66] Chandrasekhar, S. Radiative transfer. Oxford: Clarendon Press. 1960.

[67] Vargas, W. Generalized four-flux radiative transfer model. Applied Optics, Vol. 37. 1998. Pp. 2615–2623.

[68] Henyey, L. & Greenstein, J. Diffuse radiation in the galaxy. Astrophysics Journal, Vol. 93. 1941. Pp. 70–83.

[69] Caldwell, B. Kubelka–Munk coefficients from transmittance. Journal of Optical Society of America, Vol. 58. 1968. Pp. 755–758.

[70] Silberstein, L. Philosophical Magazine, Vol. 4. 1927. P. 1291.

[71] Ryde, J. Proceedings of the Royal Society (London), Vol. A90. 1931. P. 219.

[72] Ryde, J. Journal of the Society of Glass Technology, Vol. 16. 1932. P. 408.

[73] Kuhn, J., Korder, S., Arduini-Schuster, M., Caps, R. & Fricke, J. Infrared-optical transmission and reflection measurements on loose powders. Review of Scientific Instruments, Vol. 64. 1993. Pp. 2523–2530.

[74] Kienle, A., Patterson, M., Dögnitz, N., Bays, R., Wagnieres, G. & van den Bergh, H. Noninvasive determination of the optical properties of two-layered turbid media. Applied Optics, Vol. 37. 1998. Pp. 779–791.

[75] Wabnitz, H. & Rinneberg, H. Imaging in turbid media by photon density waves: spatial resolution and scaling relations. Applied Optics, Vol. 36. 1997. Pp. 64–74.

[76] Boas, D., Culver, J., Stott, J. & Dunn, A. Three dimensional Monte Carlo code for photon migration through complex heterogeneous media including the adult human head. Optics Express, Vol. 10. 2002. Pp. 159–170.

[77] Ramella-Roman, J., Prahl, S. & Jacques, S. Three Monte Carlo programs of polarized light transport into scattering media: Part I. Optics Express, Vol. 13. 2005. Pp. 4420–4438.

[78] Burger, T., Kuhn, J., Caps, R. & Fricke, J. Quantitative determination of the scattering and absorption coefficients from diffuse reflectance and transmittance measurements: Application to pharmaceutical powders. Applied Spectroscopy, Vol. 51. 1997. Pp. 309–317.

[79] Burger, T., Ploss, H., Kuhn, J., Ebel, S. & Fricke, J. Diffuse reflectance and transmittance spectroscopy for the quantitative determination of scattering and absorption coefficients in quantitative powder analysis. Applied Spectroscopy, Vol. 51. 1997. Pp. 1323–1329.

[80] Burger, T., Kuhn, J. & Fricke, J. NIR radiative transfer investigations to characterise pharmaceutical powders and their mixtures. Journal of Near Infrared Spectroscopy, Vol. 6. 1998. Pp. 33–40.

[81] Muinonen, K. & Saarinen, K. Ray optics approximation for Gaussian random cylinders. Journal of Quantitative Spectroscopy and Radiative Transfer, Vol. 64. 2000. Pp. 201–218.

[82] Leskelä, M. Simulation of particle packing for modelling the light scattering characteristics of paper. Ph.D. thesis. Espoo, Finland: Helsinki University of Technology. 1997.

[83] Lettieri, T., Marx, E., Song, J.-F. & Vorburger, T. Light scattering from glossy coatings on paper. Applied Optics, Vol. 30. 1991. Pp. 4439–4447.

[84] Carlsson, J., Hellentin, P., Malmqvist, L., Persson, A., Persson, W. & Wahlström, C.-G. Time-resolved studies of light propagation in paper. Applied Optics, Vol. 34. 1995. Pp. 1528–1535.

[85] Pettersson, M. & Stenström, S. Absorption of infrared radiation and the radiation transfer mechanism in paper. Part I: Theoretical model. Journal of Pulp and Paper Science, Vol. 24. 1998. Pp. 349–355.

[86] Bown, R. Physical and chemical aspects of the use of fillers in paper. In: Roberts, J. C. (Ed.) Paper Chemistry. Glasgow, UK: Blackie & Son. 1991. Pp. 162–197.

[87] Peel, J. Paper Science and Paper Manufacture. Vancouver, Canada: Angus Wilde Publications. 1999. Chapter 4.

[88] Eklund, D. & Lindström, T. Paper chemistry, an introduction. Grankulla, Finland: DT Paper Science Publications. 1991. 305 p.

[89] Peel, J. Paper science and paper manufacture. Vancouver, Canada: Angus Wilde Publications. 1999. Chapter 14.

[90] Linnonmaa, J. & Trefz, M. Pigment coating techniques. In: Papermaking Science and Technology, Vol. 11. Helsinki, Finland: Fapet Oy. 2000. Pp. 415–486.

[91] Nieto-Vesperinas, M. Scattering and diffraction in optical physics. New York: Wiley. 1991. Chapter 7.

[92] MacGregor, M. & Johansson, P.-Å. Submillimeter gloss variations in coated paper: part I, the gloss imaging equipment and analytical techniques. Tappi Journal, Vol. 73. 1990. Pp. 161–168.

[93] Noboa, H. & Seyed-Yagoobi, J. A critical review of drying models for coated paper. Proceedings of the 1999 ASME International Mechanical Engineering Congress. 1999. Pp. 1–14.

[94] Rajala, P. & Karlsson, M. A drying model for coated paper, for improved printing properties. Proceedings of the 1995 ASME International Mechanical Engineering Congress. 1995. Pp. 445–450.

[95] Karlsson, M. Papermaking Science and Technology, Vol. 9: Papermaking part 2, drying. Helsinki, Finland: Fapet Oy. 2000. Chapters 2, 3 and 4.

[96] Martin, H. Heat and mass transfer between impinging gas jets and solid surfaces. In: Advances in heat transfer. New York: Academic Press. 1977.

[97] Heikkilä, P. & Milosavljevic, N. Influence of impingement temperature and nozzle geometry on heat transfer – Experimental and theoretical analysis. Drying Technology, Vol. 21. 2003. Pp. 1957–1968.

[98] Karlsson, M. & Timofeev, O. Computer simulation of a multicylinder dryer with single-tier configuration. Proceedings of the 5th International Symposium on Process Systems Engineering, PSE ’94, Kyongju, Korea. 1994. Pp. 363–368.

[99] Lampinen, M. & Ojala, K. Mathematical modeling of web drying. In: Advances in Transport Processes, Vol. IX. Elsevier Science Publishers. 1993. Chapter 7.

[100] Pajari, H., Mansikka-aho, J., Ketoja, J. & Bousfield, D. Blade coating with free jet applicator: Modelling and experiments. Proceedings of TAPPI Advanced Coating Fundamentals Symposium. 2003. Pp. 65–82.

[101] TAPPI standard T 480 om-99. TAPPI Optical Properties Committee of the Process and Product Quality Division. TAPPI. 1999.

[102] Köhler, A. Zeitschrift für wissenschaftliche Mikroskopie, Vol. X. 1893. Pp. 433–440.

[103] Goldstein, R. & Penner, S. The near-infrared absorption of liquid water at temperatures between 27 and 209 C. Journal of Quantitative Spectroscopy and Radiative Transfer, Vol. 4. 1964. Pp. 441–451.

[104] Lehtonen, P. Paper moisture depth profiling by using near infrared spectroscopy and gloss measurement. Master of Science Thesis. Oulu, Finland: University of Oulu. 2005.

[105] Dam, J., Dalgaard, T., Fabricius, P. & Andersson-Engels, S. Multiple polynomial regression method for determination of biomedical optical properties from integrating sphere measurements. Applied Optics, Vol. 39. 2000. Pp. 1202–1209.

[106] Jääskeläinen, A., Peiponen, K.-E., Tapper, U., Kauppinen, E. & Lumme, K. Effective refractive index of calcium carbonate pigment slurries by a surface-plasmon-resonance sensor. Dyes and Pigments, Vol. 52. 2002. Pp. 15–21.

[107] Champion, J., Meeten, G. & Senior, M. Refraction by spherical colloid particles. Journal of Colloid and Interface Science, Vol. 72. 1979. Pp. 471–482.

[108] Meeten, G. & North, A. Refractive index measurement of turbid colloidal fluids by transmission. Measurement Science and Technology, Vol. 2. 1991. Pp. 441–447.

[109] Meeten, G. & North, A. Refractive index measurement of absorbing and turbid fluids by reflection near the critical angle. Measurement Science and Technology, Vol. 6. 1995. Pp. 214–221.

[110] Alexander, K., Killey, A., Meeten, G. & Senior, M. Refractive index of concentrated colloidal dispersions. Journal of Chemical Society, Faraday Trans. 2, Vol. 77. 1981. Pp. 361–372.

[111] Lehtinen, E. Papermaking Science and Technology, Vol. 11: Pigment Coating and Surface Sizing of Paper. Helsinki, Finland: Fapet Oy. 2000. Chapter 4.

[112] Jarzembski, M., Norman, M., Fuller, K., Srivastava, V. & Cutten, D. Complex refractive index of ammonium nitrate in the 2–20-μm spectral range. Applied Optics, Vol. 42. 2003. Pp. 922–930.

[113] Arakawa, E., Tuminello, P., Khare, B., Milham, M., Authier, S. & Pierce, J. Measurement of optical properties of small particles. Scientific Conference on Obscuration and Aerosol Research, Aberdeen Proving Ground, Maryland, June 23–26. 1997. 30 p.

[114] Kowalski, K. Methods of Hilbert spaces in the theory on nonlinear dynamical systems. World Scientific. 1994. Appendix E.

[115] Naes, T., Isaksson, T., Fearn, T. & Davies, T. Multivariate Calibration and Classification. Chichester, UK: NIR Publications. 2002. Chapter 17.

Appendix A: Mathematics of the inverse Monte Carlo model

This Appendix describes in detail how the inverse Monte Carlo model works. As described in Section 5.1, the inverse model finds the values of the functions $\mu_a = \mu_a(R,T,C)$, $\mu_s = \mu_s(R,T,C)$ and $g = g(R,T,C)$ with a particular combination of the measured values *D*, *T*, and *C*. This is done by an iterative algorithm, which will be described in the following.

The inverse algorithm is actually a fitting procedure: there is an unknown function of the fitting variables, and the best values for these fitting variables to make a best fit to the fitted variables is being sought. Because the underlying function is unknown and nonlinear, an iterative procedure is needed.

There are some assumptions in the present implementation of the inverse model:

- The sample consists of layers:
    - The layer whose optical properties are to be determined is chosen. It will be called the *active layer* hereafter.
    - The properties of the other layers are given. Typically, these other layers are the walls of a cuvette.
- The thickness and the refractive index of the active layer are fixed.
- From the absorption coefficient, scattering coefficient and anisotropy factor of the active layer, one, two, or all three are chosen as the fitting variables. The others are fixed.
- The direct MCML model calculates the diffuse reflectance, diffuse transmittance and collimated transmittance of the sample. The definition of these quantities may be different in different modelling geometries. Of these three, one, two, or all three are chosen as the fitted variables in the inverse algorithm.

Of course, the number of fitted variables cannot be smaller than the number of the fitting variables.

The fitting variables are collected into the *parameter vector* **x**, and the fitted variables into the *signal vector* **y**. In the following description of the inverse algorithm, the absorption and scattering coefficients are chosen for the fitting variables, and the diffuse reflection and transmission for the fitted variables:

$$\mathbf{x} = \begin{bmatrix} \mu_a \\ \mu_s \end{bmatrix}$$
$$\mathbf{y} = \begin{bmatrix} R \\ T \end{bmatrix} \qquad \text{(A1)}$$

Recall that this is only one possible combination. The relationship between these is expressed by the vector-valued function $\mathbf{y} = \tilde{\mathrm{F}}(\mathbf{x})$. The function is unknown, but can be approximated by the MCML code at one point in the vector space at a time.

Then the measured R and T values are packed into the signal vector $\mathbf{y_m}$, in exactly the same fashion as in Equation (A1). An initial guess for the absorption and scattering coefficients is made, and they are packed into the parameter vector $\mathbf{x_g}^1$. Now everything is ready for the iterative algorithm. The variable k tells the number of iteration in question, so the iteration starts with $k = 1$.

1. Calculate the signal vector corresponding to the guess: $\mathbf{y}_\mathbf{g}^k = \tilde{\mathrm{F}}(\mathbf{x}_\mathbf{g}^k)$.

2. Calculate the difference between the measured signal and the guess-based calculated signal: $\mathbf{dy}_\mathbf{gm}^k = \mathbf{y}_\mathbf{g}^k - \mathbf{y}_\mathbf{m}$. If it is smaller than the threshold, stop the iteration and return the guess vector as the final result.

3. If this is the first iteration step, estimate the Jacobi matrix of the function $\tilde{\mathrm{F}}$ by finite differences (items 4–7). If this is not the first iteration, go to item 8.

4. Form the perturbation matrix: $\mathbf{dx} = \begin{bmatrix} d\mu_a & 0 \\ 0 & d\mu_s \end{bmatrix}$.

5. Calculate the resulting difference in the signal caused by the small perturbation: $\mathbf{dy}^k = \tilde{\mathrm{F}}\left(\left[\mathbf{x}_\mathbf{g}^k \quad \mathbf{x}_\mathbf{g}^k\right] + \mathbf{dx}\right) - \tilde{\mathrm{F}}\left(\left[\mathbf{x}_\mathbf{g}^k \quad \mathbf{x}_\mathbf{g}^k\right]\right)$ (here, the function $\tilde{\mathrm{F}}$ operates row by row to produce a matrix output from a matrix input).

6. The response is linearised by marking $\mathbf{dy}^k = \mathbf{J}^k \cdot \mathbf{dx}$, where $\mathbf{J}^k$ is the Jacobi matrix.

7. The estimated inverse of the Jacobi matrix is calculated: $(\mathbf{J}^k)^{-1} = -\mathbf{dx}(\mathbf{dy}^k)^*$, where the * means the pseudo-inverse.

8. If not the first iteration, estimate the Jacobi matrix with Broyden's update method (described below), and calculate the inverse of the Jacobi matrix $(\mathbf{J}^k)^{-1}$ using the pseudo-inverse.

9. Calculate the Newton step: $\mathbf{dx}_\mathbf{gm}^k = -(\mathbf{J}^k)^{-1}\mathbf{dy}_\mathbf{gm}^k$, and update the guess: $\mathbf{x}_\mathbf{g}^{k+1} = \mathbf{x}_\mathbf{g}^k + \mathbf{dx}_\mathbf{gm}^k$.

10. Ensure that the Newton step fulfils some convergence criteria. If not, make some modifications to the step, as discussed below.

11. Go back to 1.

In all iteration steps except the first, the Broyden's update method [49] is used to estimate the Jacobi matrix:

$$\mathbf{J}^k = \mathbf{J}^{k-1} + \frac{(\mathbf{z}^{k-1} - \mathbf{J}^{k-1}\mathbf{s}^{k-1})(\mathbf{s}^{k-1})^T}{(\mathbf{s}^{k-1})^T\mathbf{s}^k} \tag{A2}$$

where

$$\mathbf{s}^{k-1} = \mathbf{x}^k - \mathbf{x}^{k-1}$$
$$\mathbf{z}^{k-1} = \mathbf{dy}_\mathbf{gm}^k - \mathbf{dy}_\mathbf{gm}^{k-1}.$$

This method makes the number of calls to the forward MCML code lower since only one call is required per iteration. When using finite differences, three calls are required when there are two fitting variables, and four calls when there are three fitting variables.

The difference between the measured signal and the calculated signal, $\mathbf{dy}_{\mathbf{gm}}^{k}$, was chosen as the criterion for convergence, i.e. the iteration stops after the maximum difference in $\mathbf{dy}_{\mathbf{gm}}^{k}$ does not exceed the precision limit. In iterative methods it is more common to write the convergence criterion in terms of the parameters to be determined (in this case, the difference $\mathbf{x}_{\mathbf{g}}^{k+1} - \mathbf{x}_{\mathbf{g}}^{k}$). However, the precision that can be achieved with the Monte Carlo inversion depends on the number of photons used in the simulation. The error introduced by the photon statistics to the calculated *R*, *T*, and *C* values can be estimated, but the impact of this error on the inverse procedure is difficult to estimate. Thus the difference signal $\mathbf{dy}_{\mathbf{gm}}^{k}$ was selected for use in the convergence criterion. Moreover, $\mathbf{dy}_{\mathbf{gm}}^{k}$ can be used to adapt the number of photons used in the Monte Carlo simulation:

$$N_{photons} = \frac{1}{\max_i \left[\left((dy_{gm}^{k})_i \right)^2 \right]} \tag{A3}$$

In fact, this formula is only used if the $N_{photons}$ exceeds the predefined minimum number of photons, which is typically 10,000–100,000. The adaptive photon number technique is especially important when high precision is required in the estimated parameters since the estimation of the Jacobi matrix becomes unstable when the Newton algorithm begins to take very small steps.

Since negative absorption and scattering coefficients are not physically meaningful, the algorithm has to be restricted so that these negative values cannot be reached. This is done by simply replacing negative values in the guess vector with positive values.

As described above, a versatile algorithm was developed. In the algorithm, any combination of the absorption and scattering coefficients, and the anisotropy factor, can be selected as the parameters to be determined. This means the

algorithm cannot know which parameter is which, and deals with every parameter in a similar manner. The MCML code does not accept g values below zero, or above one. That is why a transformation for the anisotropy g had to be introduced:

$$g' = \frac{g}{1-g} \tag{A4}$$

This transforms the range of g from [0, 1] to [0, ∞], i.e. to the same range as the absorption and scattering coefficients. Some transformations for the absorption and scattering coefficients were also tested, but they did not make the algorithm converge faster.

In iterative methods the length of the Newton step must be controlled to prevent the algorithm from taking too large a step. This is accomplished in the algorithm by calculating the largest normalised element of the Newton step $\mathbf{dx}_{\mathbf{gm}}^{k}$:

$$r = \max_i \left(\left| \frac{(dx_{gm}^{k})_i}{(x_g^{k})_i} \right| \right) \tag{A5}$$

The r is then compared to a predefined convergence factor c. If the r is smaller than c, the Newton step is accepted as such, but if it is not, the Newton step is scaled:

$$(\mathbf{dx}_{\mathbf{gm}}^{k})' = \frac{c}{r}\mathbf{dx}_{\mathbf{gm}}^{k} \tag{A6}$$

This procedure ensures that the Newton algorithm never takes a step in which one of the fitting variables is changed more than c times its absolute value. Typically, a value of 0.5 for c makes the iteration converge smoothly towards the solution.

From a purely mathematical point of view, it would have been more elegant to write the inverse algorithm in terms of the albedo, the optical thickness and the anisotropy factor [49]. However, the absorption and scattering coefficients were selected for use as such. The most important reason for this was that the

complete diffuse reflection or diffuse transmission signals are not the only possibilities; in some cases, directional diffuse reflection signals could be used in the inversion procedure. This, combined with the directional illumination and layered sample structure, makes the advantages of using the optical thickness and the albedo quite low. Moreover, since the MCML code is written in terms of the absorption and scattering coefficients, the use of optical thickness and albedo would have introduced more transformations in the code with minimal advantages.

How to calculate the diffuse reflectance and transmittance, or the collimated transmittance, was not exactly defined in the inverse algorithm. This was done on purpose. The MCML code also returns the reflected and transmitted signal as a function of elevation angle and radial coordinate, $R_{r\alpha}(r,\alpha)$ and $T_{r\alpha}(r,\alpha)$. One may now define, for example,

$$R \equiv \iint_{\Omega,R} d\Omega dR\, R_{r\alpha}(r,\alpha)\,, \tag{A7}$$

where the regions Ω and R can be selected to resemble some particular measurement geometry. Similar definition can also be applied to the transmission case. The important consequence of this is that the absorption and scattering coefficients can be determined from normal diffuse reflectance and transmittance measurements, where "normal" means the typical experimental configurations used in reflection or transmission spectroscopy. The inverse algorithm described above is equally well suited to this kind of inversion.

Published by

Series title, number and report code of publication

VTT Publications 664
VTT–PUBS–664

Author(s)
Paaso, Janne

Title

Moisture depth profiling in paper using near-infrared spectroscopy

Abstract

A near-infrared spectroscopic method and measurement system for moisture depth profiling is presented in this thesis. The measurement system is based on a fibre-optic light source and probes, and a hyperspectral imaging spectrograph. The probes feature six different measurement geometries, including a specular reflection measurement, and diffuse reflection and transmission measurements, all of which are measured in seven positions simultaneously. A theoretical analysis of the depth profiling capabilities of the system is presented, as well as laboratory tests of the system performance. Based on these, the analysis depth of the reflection moisture measurement in a 75 µm thick uncoated paper is estimated to be about 40 µm. It is also shown that the depth profiling properties depend on the average moisture content of the paper, and that the inclusion of a coating layer complicates the depth profiling. The use of the theoretical analysis results in the interpretation of the measurement results is also discussed.

As the main application, the measurement system was installed on a pilot-scale paper coating machine. The feasibility of semi-quantitative moisture depth profiling during the coating process is shown. The determination of the first and second critical concentrations of the coating colour consolidation process is also discussed. Detailed results from the extensive programme of trial runs are presented, along with discussion of the physics behind the measurements. It is found that the water transport characteristics measured during the coating process are not in accordance with mass and heat transfer theories in some respects. Also, the specular reflection measurement results do not behave as expected, making the determination of the first critical concentration impossible in some cases. Instead, the second critical concentration is easily detected, but does not always behave as expected. Reasons for the unexpected behaviour of the measurements are discussed, and conclusions drawn about the water transport during the coating process.

ISBN
978-951-38-7063-8 (soft back ed.)
978-951-38-7064-5 (URL: http://www.vtt.fi/publications/index.jsp)

Series title and ISSN	Project number
VTT Publications 1235-0621 (soft back ed.) 1455-0849 (URL: http://www.vtt.fi/publications/index.jsp)	540

Date	Language	Pages
November 2007	English	193 p. + app. 6 p.

Name of project	Commissioned by
COATME2	KCL, Tekes – the Finnish Funding Agency for Technology and Innovation, the Infotech Oulu Graduate School, VTT

Keywords	Sold by
moisture content, depth profiling, paper coating, optical properties, near-infrared spectroscopy, NIR, fibre-optic light sources, fibre-optic probes, multichannel spectroscopy, water transport characteristics, on-line measurement, Monte Carlo modelling	VTT Technical Research Centre of Finland P.O.Box 1000, FI-02044 VTT, Finland Phone internat. +358 20 722 4520 http://www.vtt.fi

A near-infrared spectroscopic method and measurement system for moisture depth profiling is presented in this work. The measurement system is based on a fibre-optic light source and probes, and a hyperspectral imaging spectrograph. The probes feature six different measurement geometries, including a specular reflection measurement, and diffuse reflection and transmission measurements. A theoretical analysis of the depth profiling capabilities of the system is presented, as well as laboratory tests of the system performance. Based on these, the analysis depth of the reflection moisture measurement in a 75 µm thick uncoated paper is estimated to be about 40 µm. The measurement system was installed in a paper coating machine to measure the moisture depth profile, specular reflection intensity and diffuse reflection intensity in seven positions simultaneously. The determination of the first and second critical concentrations of the coating colour consolidation process is discussed.

It is found that the water transport characteristics measured during the coating process are not in accordance with mass and heat transfer theories in some respects. Also, the specular reflection measurement results do not behave as expected, making the determination of the first critical concentration impossible in some cases. Instead, the second critical concentration is easily detected, but does not always behave as expected. Reasons for the unexpected behaviour of the measurements are discussed, and conclusions drawn about the water transport during the coating process.

Julkaisu on saatavana
VTT
PL 1000
02044 VTT
Puh. 020 722 4520
http://www.vtt.fi

Publikationen distribueras av
VTT
PB 1000
02044 VTT
Tel. 020 722 4520
http://www.vtt.fi

This publication is available from
VTT
P.O. Box 1000
FI-02044 VTT, Finland
Phone internat. + 358 20 722 4520
http://www.vtt.fi

ISBN 978-951-38-7063-8 (soft back ed.)
ISSN 1235-0621 (soft back ed.)

ISBN 978-951-38-7064-5 (URL: http://www.vtt.fi/publications/index.jsp)
ISSN 1455-0849 (URL: http://www.vtt.fi/publications/index.jsp)